

1988

Kinetics of reactions of oxygen with the Pd(100) surface: Adsorption, desorption, reconstruction, and oxidation

Sheng-Liang Chang
Iowa State University

Follow this and additional works at: <https://lib.dr.iastate.edu/rtd>

 Part of the [Physical Chemistry Commons](#)

Recommended Citation

Chang, Sheng-Liang, "Kinetics of reactions of oxygen with the Pd(100) surface: Adsorption, desorption, reconstruction, and oxidation " (1988). *Retrospective Theses and Dissertations*. 9765.
<https://lib.dr.iastate.edu/rtd/9765>

This Dissertation is brought to you for free and open access by the Iowa State University Capstones, Theses and Dissertations at Iowa State University Digital Repository. It has been accepted for inclusion in Retrospective Theses and Dissertations by an authorized administrator of Iowa State University Digital Repository. For more information, please contact digirep@iastate.edu.

INFORMATION TO USERS

The most advanced technology has been used to photograph and reproduce this manuscript from the microfilm master. UMI films the original text directly from the copy submitted. Thus, some dissertation copies are in typewriter face, while others may be from a computer printer.

In the unlikely event that the author did not send UMI a complete manuscript and there are missing pages, these will be noted. Also, if unauthorized copyrighted material had to be removed, a note will indicate the deletion.

Oversize materials (e.g., maps, drawings, charts) are reproduced by sectioning the original, beginning at the upper left-hand corner and continuing from left to right in equal sections with small overlaps. Each oversize page is available as one exposure on a standard 35 mm slide or as a 17" x 23" black and white photographic print for an additional charge.

Photographs included in the original manuscript have been reproduced xerographically in this copy. 35 mm slides or 6" x 9" black and white photographic prints are available for any photographs or illustrations appearing in this copy for an additional charge. Contact UMI directly to order.



300 North Zeeb Road, Ann Arbor, MI 48106-1346 USA



Order Number 8825907

**Kinetics of reactions of oxygen with the Pd(100) surface:
Adsorption, desorption, reconstruction, and oxidation**

Chang, Sheng-Liang, Ph.D.

Iowa State University, 1988

U·M·I

**300 N. Zeeb Rd.
Ann Arbor, MI 48106**



PLEASE NOTE:

In all cases this material has been filmed in the best possible way from the available copy. Problems encountered with this document have been identified here with a check mark .

1. Glossy photographs or pages
2. Colored illustrations, paper or print _____
3. Photographs with dark background
4. Illustrations are poor copy _____
5. Pages with black marks, not original copy
6. Print shows through as there is text on both sides of page _____
7. Indistinct, broken or small print on several pages _____
8. Print exceeds margin requirements _____
9. Tightly bound copy with print lost in spine _____
10. Computer printout pages with indistinct print _____
11. Page(s) _____ lacking when material received, and not available from school or author.
12. Page(s) _____ seem to be missing in numbering only as text follows.
13. Two pages numbered _____. Text follows.
14. Curling and wrinkled pages _____
15. Dissertation contains pages with print at a slant, filmed as received _____
16. Other _____

U·M·I



**Kinetics of reactions of oxygen with the Pd(100) surface:
Adsorption, desorption, reconstruction, and oxidation**

by

Sheng-Liang Chang

**A Dissertation Submitted to the
Graduate Faculty in Partial Fulfillment of the
Requirements for the Degree of
DOCTOR OF PHILOSOPHY**

Department: Chemistry

Major: Physical Chemistry

Approved:

Signature was redacted for privacy.

In Charge of Major Work

Signature was redacted for privacy.

For the Major Department

Signature was redacted for privacy.

For the Graduate College

**Iowa State University
Ames, Iowa
1988**

TABLE OF CONTENTS

	Page
GENERAL INTRODUCTION	1
PAPER I: FORMATION OF A METASTABLE ORDERED SURFACE PHASE DUE TO COMPETITIVE DIFFUSION AND ADSORPTION KINETICS: OXYGEN ON Pd(100)	5
PAPER II: THE INITIAL STAGES OF OXYGEN ADSORPTION ON Pd(100) AT 300 K AND BELOW: ADSORPTION KINETICS AND ADSORPTION SITE REQUIREMENTS	25
PAPER III: OXYGEN ON Pd(100): ORDER, RECONSTRUCTION, AND DESORPTION	63
PAPER IV: OXYGEN-STABILIZED RECONSTRUCTION OF Pd(100): PHASE TRANSITIONS DURING OXYGEN DESORPTION	116
PAPER V: PHASE DIAGRAM OF O/Pd(100)	172
APPENDIX: THE LEED PROGRAM	223
CONCLUSIONS	243
REFERENCES	245
ACKNOWLEDGEMENTS	246

GENERAL INTRODUCTION

When a gas molecule approaches a metal surface, the molecule can be trapped in a potential energy well on the surface. If the surface exhibits a long range two-dimensional periodicity, ordered adlayers can result from the interactions between adsorbates combined with the site-dependent interactions between a particle and substrate. The purpose of this dissertation is to study the evolution of ordered surface adlayers under ultrahigh vacuum conditions. The system oxygen/Pd(100) is chosen to investigate the formation and the variation of oxygen adlayers when oxygen coverage and substrate temperature are changed. We employ traditional surface science techniques to accomplish this goal: AES (Auger electron spectroscopy) is used to examine impurities on the surface and to provide coverage information, TDS (thermal desorption spectroscopy) is used to calibrate the oxygen coverage and to extract bond strengths, and LEED (low-energy electron diffraction) is used to monitor variations of ordered structures on the surface.

Palladium is important from the view point of oxidation reactions. Several studies have been done concerning carbon monoxide and hydrogen oxidation on various Pd surfaces. The formation of CO_2 and H_2O on Pd surfaces has been studied by many groups (1-5). These reactions follow the Langmuir-Hinshelwood mechanism which means that all species have to adsorb on Pd surfaces before the final products are formed. Conrad et al. have studied the CO oxidation on a Pd(111) surface and have shown that CO adsorbs associatively while oxygen adsorbs dissociatively on

this surface (1). Stuve et al. (2) obtain similar results on a Pd(100) surface and confirm that this reaction is structure insensitive (3). Formation of H_2O on Pd(100) surface has also been studied with EELS and LEED by Nyberg and Tengstäl (4). They have observed a hydroxyl group existing on the surface in addition to atomic oxygen and associated H_2O . A later study by Petersson et al. has shown that the formation of the hydroxyl species is the rate-determining step (5).

All these studies point out a common fact, that is, such reactions involve the formation of atomic oxygen on surfaces. All of these studies emphasize the reaction mechanism between the co-adsorbates. However, there is a very fundamental and interesting problem which has been largely overlooked, which is the interaction between atomic oxygen and the Pd surfaces. This may also strongly influence the reaction mechanism.

Ertl and Koch (6) were the first to observe the formation of a $p(2 \times 2)$ ordered oxygen structure on Pd(100), but they failed to generate any higher coverage structures at room temperature. Nyberg and Tengstäl (7) applied EELS to study this system. They proposed that oxygen dissociatively adsorbs on the (100) face at temperatures higher than 120 K, and that atomic oxygen sits in the four-fold hollow. Later, Rieder and Stocker (8) performed helium diffraction experiments and confirmed that oxygen atoms are indeed located in the four-fold hollow sites. Thermal desorption experiments were carried out by Stuve et al. (2). In their studies, three desorption peaks were observed but the assignment of these peaks to the surface structures was only vague.

Orent and Bader (9) successfully observed at least four different ordered adlayers formed under various experimental conditions, including two oxygen orderings and two oxygen-induced reconstructions. The two reconstructed structures were tentatively attributed to two of the low index bulk PdO planes based on the unit cell derived from the observed LEED patterns, but there was no firm evidence about the arrangement of oxygen atoms within the unit cell.

As can be seen from these studies, different surface ordered adlayers can be formed under different conditions. As a result, a discussion of any heterogeneous catalytic reactions cannot be completed without dealing with all the phases formed on the surfaces.

Reconstructions can be particularly important in catalytic reactions. For example, a study of CO oxidation on a polycrystalline Pt wire has shown that the reaction rate oscillates periodically as a function of CO coverage (10). Further investigation has proven that the cause of the oscillation is the reversible phase transition between the reconstructed and unreconstructed Pt(100) surface (11).

In order to have a better understanding about the variation of oxygen ordered adlayers on Pd(100) surface, we developed a sophisticated system (12) to monitor the changes of LEED patterns which reflect the long range periodicity of ordered structures on a surface. This computer-interfaced video camera together with LEED optics is known as video-LEED (13,14). Due to the speed and the memory capacity of the computer, a large amount of data can be acquired and analyzed in a relatively short time. In addition, the interruption between two

sequential experimental data points can be made as small as 1/30 seconds. Therefore, more complete experimental information can be obtained. The characteristics of the video-LEED and a brief explanation of the computer code that drives the interface are described at the end of this dissertation.

Explanation of Dissertation Format

This dissertation is arranged according to the alternate style format. Five papers are collected. Paper I, "Formation of a Metastable Ordered Surface Phase Due to Competitive Diffusion and Adsorption Kinetics: Oxygen on Pd(100)," was published in volume 59 of the Physical Review Letters on pages 296-299, 1987. Paper II, "The Initial Stages of Oxygen Adsorption on Pd(100) at 300 K and Below: Adsorption Kinetics and Adsorption Site Requirements", will be submitted to Surface Science. Paper III, "Oxygen on Pd(100): Order, Reconstruction, and Desorption", was published in volume 88 of the Journal of Chemical Physics on pages 2071-2082. Paper IV, "Oxygen-Stabilized Reconstructions of Pd(100): Phase Transitions During Oxygen Desorption", has been submitted to Surface Science. Paper V, "Phase Diagram of O/Pd(100)", will be submitted to Physical Review B.

PAPER I:

FORMATION OF A METASTABLE ORDERED SURFACE PHASE DUE TO COMPETITIVE
DIFFUSION AND ADSORPTION KINETICS: OXYGEN ON Pd(100)

FORMATION OF A METASTABLE ORDERED SURFACE PHASE DUE TO COMPETITIVE
DIFFUSION AND ADSORPTION KINETICS: OXYGEN ON Pd(100)

S.-L. Chang and P. A. Thiel

Department of Chemistry and Ames Laboratory-USDOE
Iowa State University
Ames, Iowa 50011 USA

ABSTRACT

A metastable $c(2 \times 2)$ structure is formed by atomic oxygen on Pd(100) under conditions of slow diffusion combined with rapid adsorption. We propose that formation of the $c(2 \times 2)$ under these conditions must be controlled by characteristics of the dissociative adsorption event itself.

I. INTRODUCTION

In the past twenty years, there has been a great deal of research into the characteristics of two-dimensional phase diagrams of small molecules adsorbed on surfaces (e.g., 1,2). Structures formed under non-equilibrium conditions (metastable structures) remain uncharacterized, presumably because of expectations that they will simply exhibit a high degree of disorder, and thereby prove largely uninteresting. Indeed, conditions where surface diffusion is slow (low substrate temperature) have been used deliberately to prepare metastable disordered adlayers of oxygen for studies of temperature-dependent ordering kinetics (e.g., 3,4). We report in this Letter that a metastable ordered structure can be formed by atomic oxygen on Pd(100) under extreme conditions of slow diffusion combined with rapid adsorption. Observation of such metastable structures is predicted to be a general phenomenon which is related directly to the nature of the adsorption step.

II. EXPERIMENTAL

The experiments are carried out in a standard ultrahigh vacuum chamber equipped with instrumentation for Auger electron spectroscopy (AES), low-energy electron diffraction (LEED), and quadrupole mass spectrometry. The background pressure is below 2×10^{-10} Torr prior to oxygen dosing. Oxygen gas is introduced via a leak valve by backfilling the entire chamber. A detailed description of the video-LEED system used in this experiment can be found elsewhere (5).

III. RESULTS AND DISCUSSION

It is well known that oxygen adsorbs dissociatively on Pd(100) at room temperature, forming two stable ordered structures: a p(2x2) with an ideal coverage of 0.25 monolayers, and a $(\sqrt{2} \times \sqrt{2})R45^\circ$ [also known as a c(2x2)] with an ideal coverage of 0.50 monolayers (6,7). [One monolayer, $\theta = 1$, is defined here as one adsorbed particle per surface Pd atom, 1.32×10^{15} particles cm^{-2} .] The phase diagram is very similar to that of oxygen on Ni(100) (8). The forces which give rise to the p(2x2) and c(2x2) phases are believed to be mainly pairwise: strong nearest-neighbor (n.n.) repulsions, weak second-n.n. repulsions, and weak third-n.n. attractions (7-9). For both Pd(100) and Ni(100), it has been reported that the adsorption probability drops close to zero at 0.25 monolayers, and because of this, exposures in excess of 50 Langmuirs are necessary to remove all traces of the p(2x2) and form the well-ordered c(2x2) (7,9). Our own findings corroborate these statements (10). Furthermore, we observe that atomic oxygen can form a metastable c(2x2) structure under conditions of low sample temperature and high oxygen pressure. The metastable c(2x2) is formed under conditions much different from those described for the stable c(2x2), because it is not preceded by the p(2x2) phase and it forms at a relatively low exposure.

Two physical processes whose rates can be controlled during formation of an adsorbed layer are dissociative adsorption and atomic diffusion. To a first approximation, these rates vary as simple

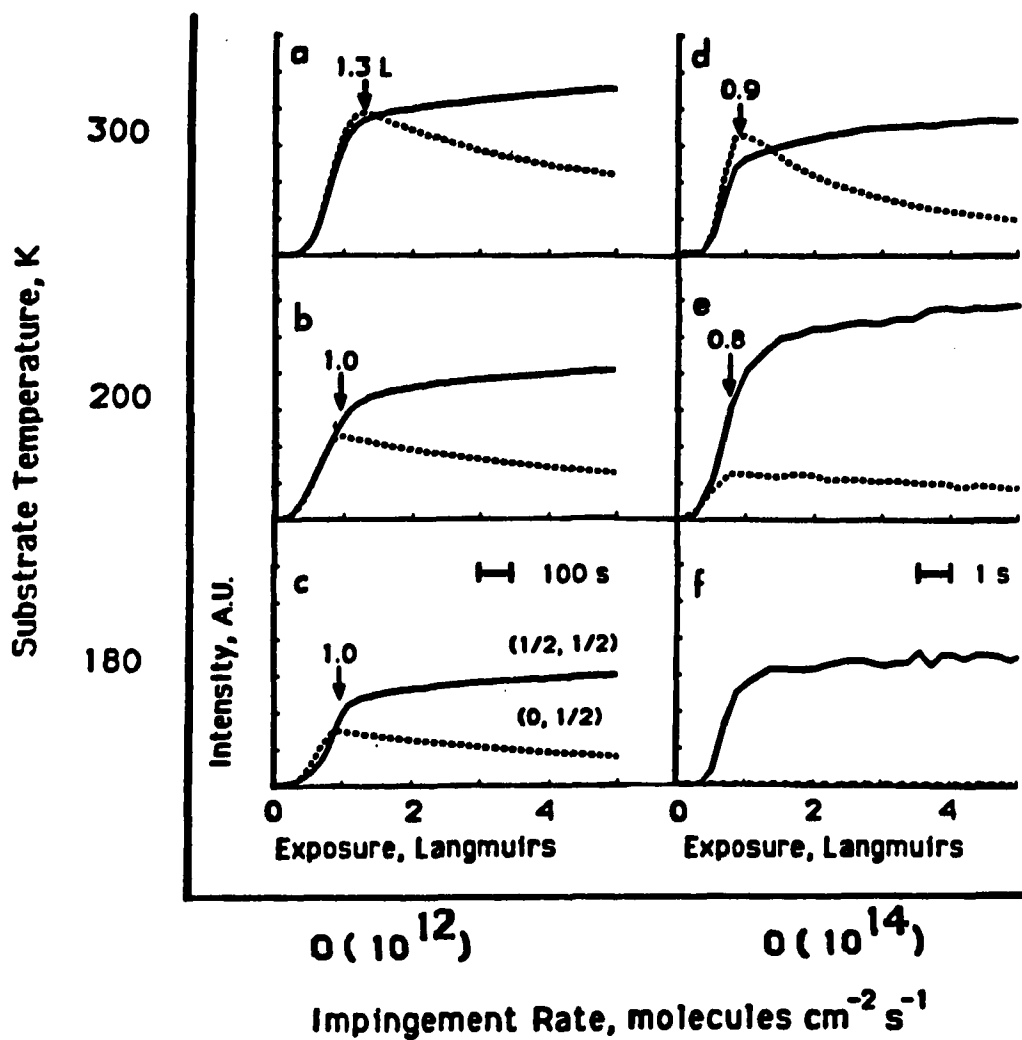


Figure 1. Changes in intensity of $(1/2, 1/2)$ and $(0, 1/2)$ LEED spots during adsorption of oxygen on Pd(100), normalized to an integral-order spot of the clean surface. Each of curves (a)-(f) shows the results of an individual experiment, at the sample temperature and oxygen impingement rate indicated. The impingement rates on the left and right sides are $1.1 \pm 0.1 \times 10^{12}$ and $6 \pm 3 \times 10^{13} \text{ cm}^{-2} \text{ s}^{-1}$, respectively. Each intensity axis represents the same (arbitrary) scale.

functions of two experimental parameters: gas impingement rate (gas pressure) and sample temperature, respectively. In Figure 1 we show the development of intensity of two LEED spots as a function of oxygen exposure for various combinations of oxygen pressure and sample temperature. The $(0,1/2)$ spot signals only the $p(2 \times 2)$ structure, whereas the $(1/2,1/2)$ spot is present both for the $p(2 \times 2)$ and $c(2 \times 2)$ lattices. Figures 1a-c indicate the development of intensity in these features at constant (low) impingement rate and at decreasing sample temperature; Figures 1d-f show the same data at an impingement rate which is two orders of magnitude higher. In all cases but one, the $p(2 \times 2)$ pattern forms first and attains its maximum intensity at 0.8 to 1.3 L exposures, then fades slowly as the $c(2 \times 2)$ pattern develops. This sequence indicates that diffusion is fast relative to adsorption, so that the stable structures can form during adsorption. Note that as sample temperature decreases the maximum intensity of the $p(2 \times 2)$ diminishes at both impingement rates. This trend is more marked at the higher impingement rate, as shown by Fig. 1 d-f. Figure 1f represents the extreme in this trend: At an oxygen impingement rate on the order of $10^{14} \text{ cm}^{-2} \text{ s}^{-1}$ and sample temperatures of 150 to 180 K, the $c(2 \times 2)$ forms immediately and there is no evidence of an intermediate $p(2 \times 2)$ structure. This result is completely reproducible.

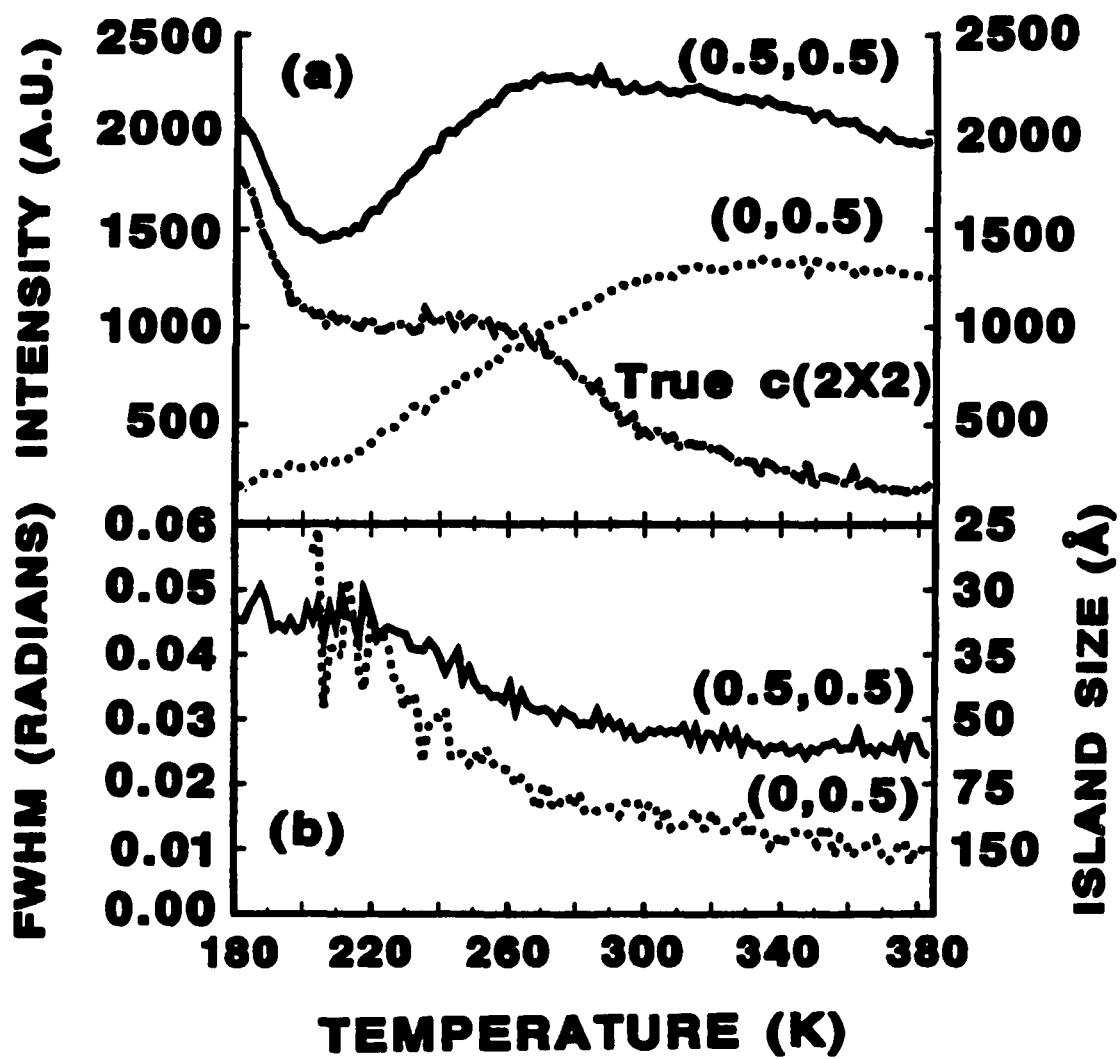
LEED I-V curves of the $(1/2,1/2)$ beam are very similar both for the $c(2 \times 2)$ which is formed under conditions of slow diffusion and rapid adsorption (Fig. 1f) and the $c(2 \times 2)$ which can be formed at 300 K using exposures of several hundred Langmuirs (10). This indicates that the

arrangement of atomic nuclei in the immediate vicinity of an oxygen nucleus within the $c(2 \times 2)$ layer is the same in both cases, i.e., the $c(2 \times 2)$ is due to atomic oxygen in the same adsorption site no matter how it is prepared.

Following an exposure of 1 L in the experiment of Fig. 1f, Auger electron spectroscopy shows that the coverage of oxygen is the same as that obtained after a 1 L exposure in the other experiments: 0.25 ± 0.03 monolayers (10). At this coverage, the $c(2 \times 2)$ prepared under the conditions of Fig. 1f can be annealed to 300 K, without measurable change in oxygen coverage. A $p(2 \times 2)$ pattern develops during the annealing. Figure 2 shows the quantitative variation in LEED spot intensity and spot width during the annealing process. The $(1/2, 1/2)$ spot represents a sum of intensity contributions from the oxygen $c(2 \times 2)$ and $p(2 \times 2)$ patterns. Therefore, the $I(T)$ function for the $c(2 \times 2)$ pattern has been obtained by subtracting $I(T)$ of the $(0, 1/2)$ beam, multiplied by an empirically-determined factor of 1.4, from $I(T)$ of the $(1/2, 1/2)$ spot. The result, shown in Fig. 2a, clearly shows that annealing causes loss of $c(2 \times 2)$ regions and simultaneous gain of $p(2 \times 2)$ domains. This is irreversible. Therefore, the $c(2 \times 2)$ formed at low temperature and at high impingement rates is a metastable (kinetically frozen) structure which reverts to the $p(2 \times 2)$ when diffusion "turns on." The $c(2 \times 2) \rightarrow p(2 \times 2)$ transformation appears to take place in two distinct stages. This will be discussed more fully elsewhere (10). The variation in spot profile widths, shown in Fig. 2b, indicates that the

Figure 2a. Variations in integrated LEED spot intensities during annealing from 180 to 380 K in vacuum, following adsorption as shown in Fig. 1f. The curve representing the "true $c(2 \times 2)$ " intensity has been obtained as described in the text. The heating rate is 1 K/s. All data are taken at the indicated temperature, with no correction for Debye-Waller attenuation of intensity.

Figure 2b. Variations in full-width half-maxima (FWHM) of LEED spots. The island sizes shown on the right abscissa are derived from the FWHM by assuming the islands have a constant, circular diameter, as described in Ref. 2. The analysis of the $(1/2, 1/2)$ spot is based on the assumption that it represents entirely $c(2 \times 2)$ islands [which is only true at $T < 200$ K], whereas the $(0, 1/2)$ spot represents only $p(2 \times 2)$ islands at all values of T . The difference in values for the island size at any given temperature derived from these two curves is due primarily to the difference in lattice constants, a , for the two structures: $a = 3.89$ Å for the $c(2 \times 2)$ structure and $a = 5.50$ Å for the $p(2 \times 2)$ structure.



c(2x2) islands are initially quite small [30 Å diameter], whereas the ultimate p(2x2) island size is ca. 150 Å (2).

Molecular, chemisorbed oxygen has been identified as a stable species on Pd(100) at temperatures below 120 K (11). In order to preclude its influence in our experiments, we use coadsorption of oxygen isotopes (O_2^{18} and O_2^{16}) to identify a thermal desorption feature at 150 K as the molecular state, based on the lack of isotopic scrambling within this feature. Assuming first-order desorption kinetics and $\nu = 10^{13} \text{ s}^{-1}$, the molecular state has a binding energy of 9 kcal/mole (12). Our adsorption experiments are performed at temperatures $> 180 \text{ K}$ and oxygen pressures $< 10^{-7} \text{ Torr}$. The values of the desorption kinetic parameters can be used to calculate that the maximum equilibrium coverage of molecular oxygen is 10^{-4} monolayers under these conditions. In short, the molecular chemisorbed state is not significantly populated during adsorption in our experiments.

We have also investigated aspects of the adsorption kinetics using AES and TDS. The initial adsorption probability, S_0 , at 150 K appears to be close to unity and is roughly twice that at 300 K, which suggests the existence of an intrinsic precursor to dissociative chemisorption. This precursor is most probably chemisorbed molecular oxygen, which is observed directly at lower temperature (11). Assuming that this is true, the lifetime of the intrinsic precursor is on the order of 10^{-2} seconds or less in the experiments of Fig. 1. This can be compared with the time between adsorption events at or near a single surface site, which is on the order of $10^3 / S_0$ seconds at an impingement rate of

$10^{12} \text{ cm}^{-2} \text{ s}^{-1}$ (Fig. 1a-c), or $10^1/S_0$ seconds at an impingement rate of $r = 10^{14} \text{ cm}^{-2} \text{ s}^{-1}$ (Fig. 1d-f). Given that S_0 is on the order of one, it is clear that the lifetime of the intrinsic precursor is far too short to be influenced by the variation of impingement rate in the regime described by the experiments of Fig. 1. Therefore, the intrinsic precursor cannot play a significant role in the suppression of $p(2 \times 2)$ and formation of $c(2 \times 2)$ at high impingement rates and low sample temperatures.

At higher coverages, $S(\theta)$ decreases. The saturation coverage decreases as temperature increases: the saturation coverage at 150 K is only ca. 0.35 monolayers. We propose the following general model: when diffusion is fast relative to adsorption (as in Figures 1a-1e), stable structures can form sequentially during adsorption; however, when diffusion is slow relative to adsorption (as in Fig. 1f), small metastable islands of $c(2 \times 2)$ form coexistent with low-density regions of disorder and domain boundaries. The time scale of diffusion which is necessary for $p(2 \times 2)$ formation can be quantified by considering that if the time between impingement events at a single site is less than 10^1 s , diffusion is too slow to allow $p(2 \times 2)$ formation (Fig. 1f), but when this time is on the order of 10^3 s , diffusion is sufficiently rapid that $p(2 \times 2)$ formation can take place (Fig. 1c). If the necessary diffusion lifetime (τ) then is on the order of 10^2 s at $T = 180 \text{ K}$, and assuming a pre-exponential factor in the diffusion rate constant (ν) of 10^{13} s^{-1} , we can calculate the activation barrier for diffusion (E_a) from

$$E_a = kT \ln(v\tau) = 12.5 \pm 1 \text{ kcal/mol.}$$

This number compares favorably with activation barriers for oxygen diffusion measured on Ir(111) (13), Rh(111) (3), and W(112) (4).

The formation of the metastable c(2x2) islands under conditions of rapid adsorption and slow diffusion must result from some characteristic of the adsorption event itself. We can envision two ways in which this might occur.

In 1984, Brundle, Behm and Barker proposed that an empty eight-site ensemble is necessary for dissociative adsorption of one oxygen molecule on Ni(100), based on Monte Carlo simulations of the coverage-dependence of the adsorption probability at 300 K (14). This ensemble, enclosed by the shaded rectangle in Fig. 3, may also be necessary for dissociative adsorption of oxygen on Pd(100). Let us first assume that the oxygen atoms are at thermal equilibrium with the metal surface immediately following dissociation. If adsorption is rapid relative to diffusion, then some molecules may adsorb randomly into adjacent, overlapping ensembles in such a way that small domains of c(2x2) are created immediately upon adsorption. Because adsorption is fast, they become locked into these c(2x2) clusters before they can respond to the weak second- and third-n.n. forces by hopping away. Meanwhile, other molecules adsorb randomly into ensembles which are not of the correct phase to continue the c(2x2) overlayer, and which trap empty space between domain boundaries. Figure 3 illustrates this effect. A recent

Monte Carlo simulation by Evans (15) indicates that rather large domains of $c(2 \times 2)$ are created under these conditions.

The second case in which a $c(2 \times 2)$ might form under non-equilibrium conditions is one in which the oxygen atoms do not equilibrate immediately following dissociation. Rupture of the oxygen-oxygen bond and formation of the Pd-O chemisorption bond is (net) exothermic by 0.8 eV per atom (10). Depending upon the efficiency of energy transfer to the surface, it may be that the oxygen atoms carry excess translational kinetic energy for some distance before finally coming to equilibrium with the cold metal. Note that such transient motion is not a "normal" type of surface diffusion. The result could be to make the translationally hot atoms unresponsive to the weak second- and third-n.n. interactions, leaving only the strong first-n.n. repulsions in effect while the atoms move and lose energy to the metal. The filling of the Pd(100) lattice would then bear some similarity to random, immobile filling of a square lattice with only nearest-neighbor exclusions operating between single particles (16). Such a process would again generate small islands of the $c(2 \times 2)$ phase in coexistence with trapped empty spaces between antiphase domains, as shown in Fig. 3.

At this point, we cannot determine which (if either) of these two models is correct. Certainly more complex models could be envisioned (15). The main point is that our data indicate that metastable ordered structures may be generally observed under conditions where the adsorption rate dominates the diffusion rate. A systematic survey of

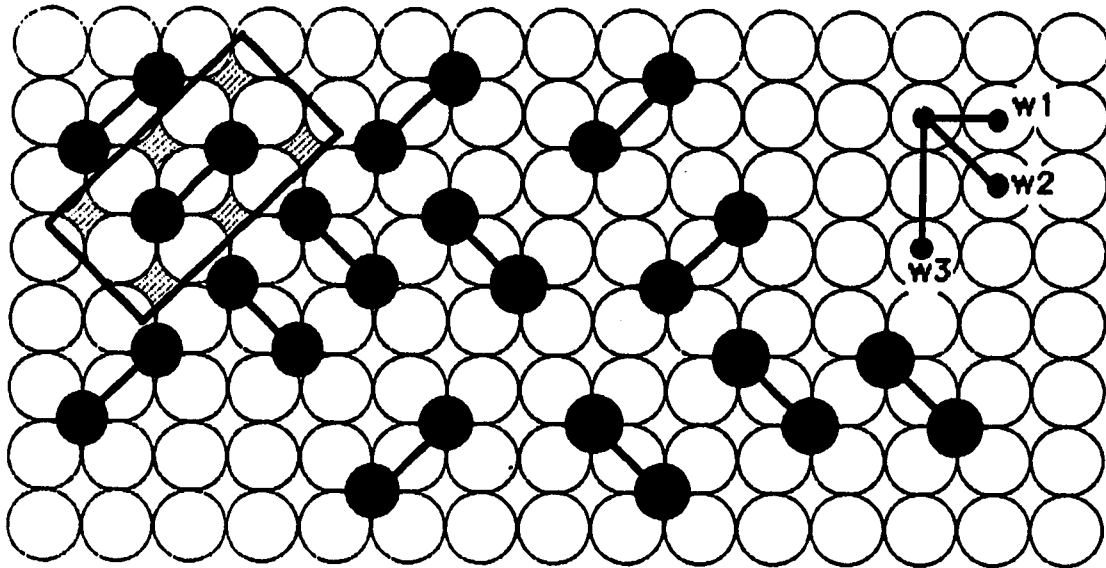


Figure 3. Illustration of random, immobile dimer adsorption into the empty eight-site ensembles described by Brundle, Behm and Barker (15). The products of each dimer's dissociation are connected by straight lines, but this only reflects the bond of the original molecule, and does not imply that a bond remains after dissociative adsorption. The open circles represent Pd atoms in the (100) plane, and the filled circles represent oxygen atoms. The pairwise forces between the oxygen atoms are shown as w_1 (strong first-n.n. repulsion), w_2 (weak second-n.n. repulsion) and w_3 (weak third-n.n. attraction) (7-9).

these structures could yield unique information about the dynamics of the adsorption process, and may prove useful as a tool in preparing kinetically frozen ordered phases of small molecules on surfaces.

In summary, we find that a metastable ordered structure can be formed by atomic oxygen on Pd(100) under conditions of rapid adsorption and slow diffusion. We propose that formation of the $c(2 \times 2)$ must be controlled by the characteristics of the dissociative adsorption event itself, and we advance two possible models to explain our results. In these models, $c(2 \times 2)$ formation is linked to the adsorption step either by the ensemble of sites necessary for dissociative adsorption of a single molecule, or else by transient motion which takes place as the atoms equilibrate with the metal after dissociation of the molecule.

IV. ACKNOWLEDGMENTS

We acknowledge important discussions with C. R. Brundle, A. E. DePristo, J. W. Evans, and R. S. Hansen. This work has been supported by the Director of Energy Research, Office of Basic Energy Sciences. Ames Laboratory is operated for the U.S. Department of Energy by Iowa State University under Contract W-7405-ENG-82.

V. REFERENCES

1. L. D. Roelofs, in Chemistry and Physics of Solid Surfaces IV, Edited by R. Vanselow and R. Howe, Springer-Verlag, Berlin (1982) pp. 219-249.
2. D. P. Woodruff, G.-C. Wang and T.-M. Lu, in The Chemical Physics of Solid Surfaces and Heterogeneous Catalysis 2, Edited by D. A. King and D. P. Woodruff, Elsevier, Amsterdam (1983) pp. 327-331.
3. P. A. Thiel, J. T. Yates, Jr. and W. H. Weinberg, *Surface Sci.* 82 (1979) 22.
4. G.-C. Wang and T.-M. Lu, *Phys. Rev. Letters* 50 (1983) 2014.
5. J. W. Anderegg and P. A. Thiel, *J. Vac. Sci. Technol. A4*, (1986) 1367.
6. G. Ertl and J. Koch, *Z. Physik. Chem.* 69 (1970) 323.
7. T. W. Orent and S. D. Bader, *Surface Sci.* 115 (1982) 323.
8. D. E. Taylor and R. L. Park, *Surface Sci.* 125 (1983) L73.
9. C. R. Brundle and J. Q. Broughton, in The Chemical Physics of Solid Surfaces and Heterogeneous Catalysis 3A, Edited by D. A. King and D. P. Woodruff, Elsevier, Amsterdam (to be published).
10. S.-L. Chang and P. A. Thiel, Chem. Dept., Iowa State Univ., in preparation.
11. C. Nyberg and C. G. Tengstäl, *Surface Sci.* 126 (1983) 163.
12. P. A. Redhead, *Vacuum* 12 (1962) 203.
13. V. P. Ivanov, G. K. Boreskov, V. I. Savchenko, W. F. Egelhoff, Jr. and W. H. Weinberg, *Surface Sci.* 61 (1976) 25.

14. C. R. Brundle, R. J. Behm and J. A. Barker, *J. Vacuum Sci. Technol.* A2 (1984) 1038.
15. J. W. Evans, *J. Chem. Phys.* 87 (1987) 3038.
16. J. W. Evans, D. R. Burgess and D. K. Hoffman, *J. Chem. Phys.* 79 (1983) 5011.

PAPER II:

THE INITIAL STAGES OF OXYGEN ADSORPTION ON Pd(100) AT 300 K
AND BELOW: ADSORPTION KINETICS AND ADSORPTION SITE REQUIREMENTS

THE INITIAL STAGES OF OXYGEN ADSORPTION ON Pd(100) AT 300 K
AND BELOW: ADSORPTION KINETICS AND ADSORPTION SITE REQUIREMENTS

S.-L. Chang and P. A. Thiel

Department of Chemistry and Ames Laboratory-USDOE
Iowa State University
Ames, Iowa 50011 USA

ABSTRACT

Adsorption of oxygen on Pd(100) is investigated by use of video-LEED and AES. The temperature ranges from 150 K to 300 K; at all these temperatures, atomic adsorption is favored. The oxygen pressure during adsorption is between 2×10^{-9} Torr and 2×10^{-7} Torr. Oxygen adsorbed on the surface under these conditions follows a molecular precursor-mediated adsorption mechanism. A metastable $c(2 \times 2)$ structure is formed under conditions of fast adsorption rate and slow diffusion rate. When this metastable $c(2 \times 2)$ is annealed from 180 K to 300 K, two steps of changes are observed: First, the metastable $c(2 \times 2)$ structure decomposes without causing any changes in the $p(2 \times 2)$ domain size. Second, as temperature increases, the $p(2 \times 2)$ domains start to grow. Our study shows that these changes are seen in this system whenever ordered adlayers are formed below 300 K. This implies that small patches of the metastable $c(2 \times 2)$ are always formed to some extent; the $c(2 \times 2)$ is strongly favored, however, by conditions where the mobility of atomic oxygen is low. In other words, kinetically limited adsorption tends to put oxygen atoms into a more condensed configuration, namely, the $c(2 \times 2)$ structure. We also discuss models to explain the formation of the metastable $c(2 \times 2)$ structure.

I. INTRODUCTION

The oxygen-palladium interaction has been a subject of extensive study in recent years. This is because adsorbed oxygen plays an important role in the oxidation reactions. While numerous investigations have been performed concerning reactions of adsorbed oxygen with CO, H₂O and small hydrocarbons (1), the chemisorption of oxygen on Pd surfaces is still not fully understood. For a Pd(100) surface, Nyberg and Tengstäl (2) have performed angular resolved high resolution electron energy loss spectroscopy (EELS) and LEED experiments between 80 K and 300 K. They found that at 80 K dissociatively adsorbed oxygen predominates at low coverages, and molecularly adsorbed oxygen forms after formation of one monolayer of atomic oxygen. The two different adsorbed states on the Pd(100) surface are characterized by two energy loss peaks in their EELS spectra. The atomic state shows a loss feature at 44 meV and the molecular state has a loss feature at 90 meV. Thermal desorption experiments show that the molecular oxygen desorbs at ~ 150 K and the atomic oxygen desorbs at 670 K ~ 800 K (1,3). The oxygen adatoms are proposed to locate in the four fold hollow sites. Rieder and Stocker (4) have confirmed this result based on their He diffraction experiments.

Two ordered adlayers formed at different coverages by atomic oxygen at 300 K are observed by means of LEED (5,6). The p(2x2) structure which has an ideal coverage of 0.25 monolayers forms first. Following formation of the p(2x2) is the c(2x2) structure which has an ideal

coverage of 0.5 monolayers. The sequence of ordered adlayer formation probably implies that the lateral interactions involved between adsorbates are strong nearest neighbor (n.n.) repulsions, weak next-nearest neighbor (n.-n.n.) and weak third-nearest neighbor (third-n.n.) attractions (7). The real and reciprocal space representations of the two ordered structures are shown in Fig. 1. The $(1/2, 1/2)$ spot appears in both of the $p(2 \times 2)$ and $c(2 \times 2)$ patterns while the $(0, 1/2)$ spot can only be observed in the $p(2 \times 2)$ structure. Therefore, it is possible to study the growth of these two ordered structures by monitoring intensity variations of the spots.

We have previously reported that oxygen adsorption on a Pd(100) surface can form a metastable $c(2 \times 2)$ structure when adsorption rate dominates the diffusion rate (3). In the present paper, we show AES and LEED results of adsorption of oxygen on the Pd(100) surface between 180 K and 300 K. The metastable $c(2 \times 2)$ is characterized and the adsorption mechanism for oxygen are discussed.

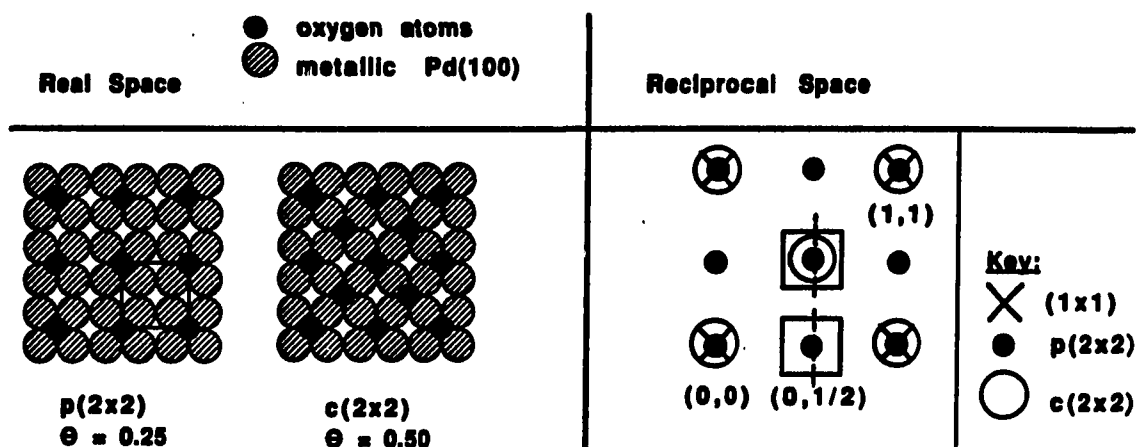


Figure 1. Real and reciprocal-space representations of the chemisorbed adlayers formed by oxygen on Pd(100). In the reciprocal space representations, the spots which are selected for measurement of integrated intensities are enclosed by rectangles. The spot profile measurements are shown by dashed lines.

II. EXPERIMENTAL

The experiments are performed in a Varian stainless steel ultrahigh vacuum chamber. The ultrahigh vacuum (UHV) is achieved by a 220 ℓ /sec ion pump, a 170 ℓ /s turbo molecular pump and a titanium sublimation pump. The apparatus is shown in Fig. 2. The chamber is equipped with a single-pass cylindrical mirror analyzer (CMA) Auger spectrometer and LEED optics for surface characterization, a mass spectrometer for thermal desorption experiments, and an ion bombardment electron gun for surface cleaning. Oxygen gas (99.6% purity, extra dry, Matheson Gas Products Co.) is introduced through a leak valve by back filling the entire chamber.

The 10 mm x 8 mm x 1 mm Pd disc is grown by the Ames Laboratory and is cut from a rod of Pd single crystal within 0.5° of the (100) face. It is aligned by a Laue back reflection camera and both sides are mechanically polished to a mirror finish. The final stage of polishing is achieved by using 0.05 μ diameter alumina slurry. No electrochemical or etching treatment is used. The sides of the sample are spot-welded to two 0.02 inch diameter Ta wires. These two wires are spot-welded to two 0.08 inch diameter Ta rods which are connected to the cold finger via two cylindrical Cu clamps. The rotatable sample manipulator, which can be cooled by liquid nitrogen (LN_2), is described elsewhere (8). The sample is heated resistively by passing current through it. Temperatures are measured by 0.03 inch diameter W(5% Re)/W(26% Re) thermocouple wires spot-welded on the center, top of the sample.

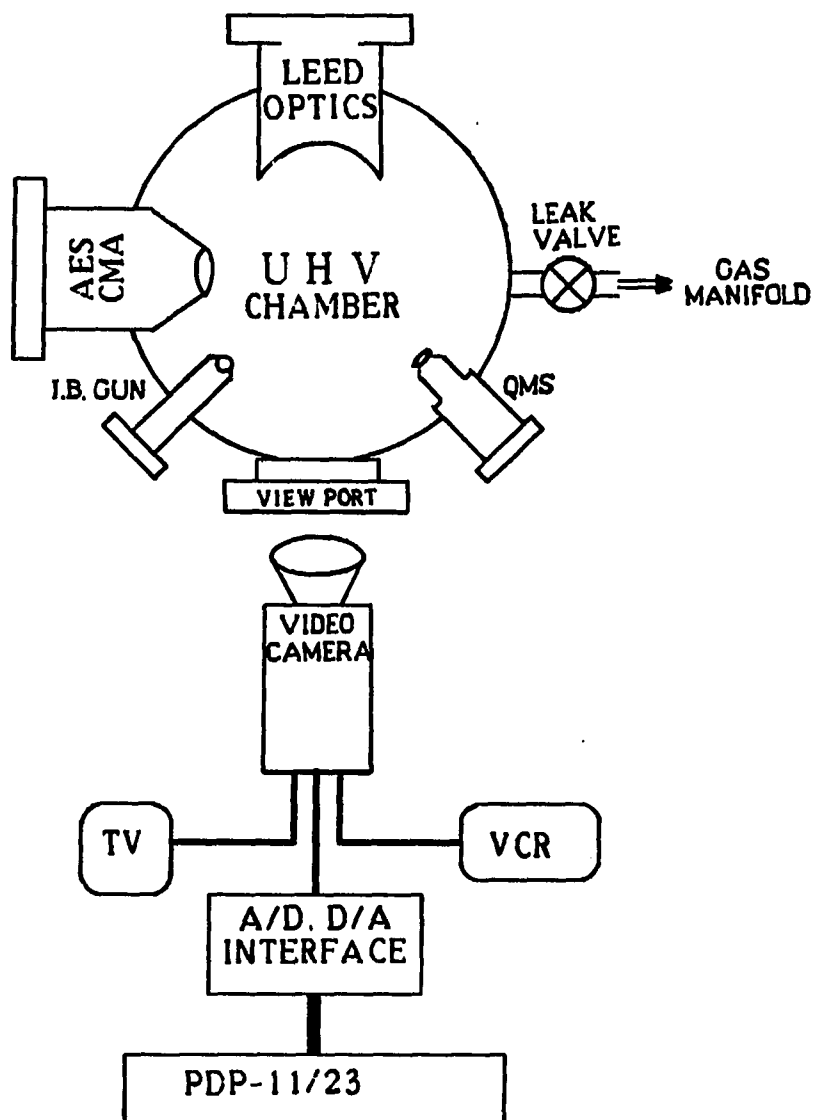


Figure 2. Schematic of ultrahigh vacuum system and computer-interfaced video-LEED.

The procedures used to clean the sample in vacuum are described elsewhere (9). The final clean sample shows no detectable impurities, i.e., C, S, P, or O from the AES spectra. The full width at half maximum (FWHM) of the integral-order LEED spot, which is a measure of the degree of perfection of the substrate, is about 4 to 6% of the surface Brillouin zone for the clean Pd sample. A detailed description of the video-LEED apparatus shown in Fig. 2 can be found in Ref. 10.

III. EXPERIMENTAL RESULTS

A. AES Study of Oxygen Adsorption on Pd(100)

Auger spectroscopy is used to measure the relative coverage of oxygen. This is done by monitoring the ratio of peak-to-peak amplitudes between oxygen 511 eV and Pd 330 eV transitions as a function of oxygen exposure. This result is shown in Fig. 3. The left coordinate, coverage (θ), is found by assuming $\theta = 0.25$ at 1 L of exposure at room temperature. This coverage calibration is based on the fact that the intensity of the (0, 1/2) spot, which represents the perfection of the p(2x2) structure, reaches a maximum at ~ 1 L of oxygen exposures. The experimental results that show the growth of ordered adlayers monitored by LEED are discussed in the next section.

In Fig. 4, we show the sticking coefficient of oxygen on this surface as a function of exposure. This is obtained by differentiating the data of Fig. 3. The result indicates that the initial sticking coefficient is temperature dependent. Assuming that this quantity is 1.0 at 180 K, it decreases to 0.6 at 300 K. Fig. 4 also shows that the sticking probability approaches zero after 1/4 monolayers at all temperatures. However, AES is highly uncertain as θ approaches 1/4 monolayer based on our TDS results (8). This is probably due to electron stimulated desorption. The TDS results show that saturation exceeds 0.25 monolayers in all the experiments of Fig. 3. In a previous study, Orent and Bader (6) report that the initial sticking probability is 0.1 at 300 K and drops two orders of magnitude from 0.1 to 0.001 as

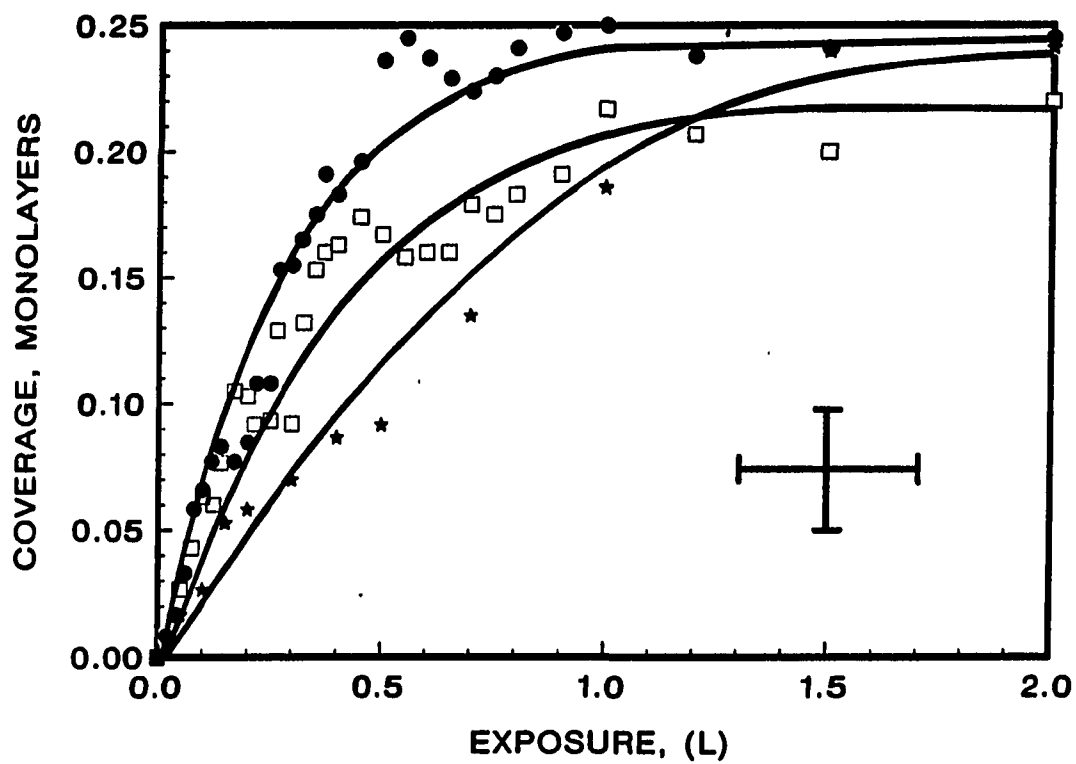


Figure 3. Coverage calibration based on AES results. The filled circles represent 180 K adsorption, squares are 200 K, and stars are 300 K.

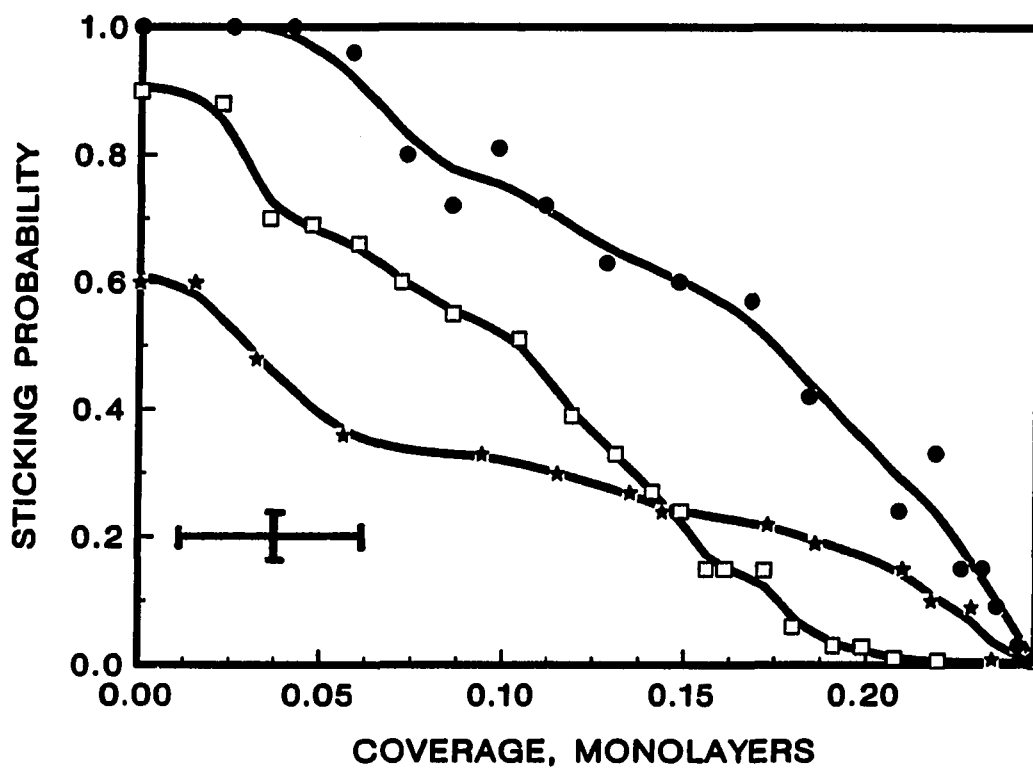


Figure 4. Sticking coefficients of dissociative adsorption of oxygen on Pd(100) at various temperatures.

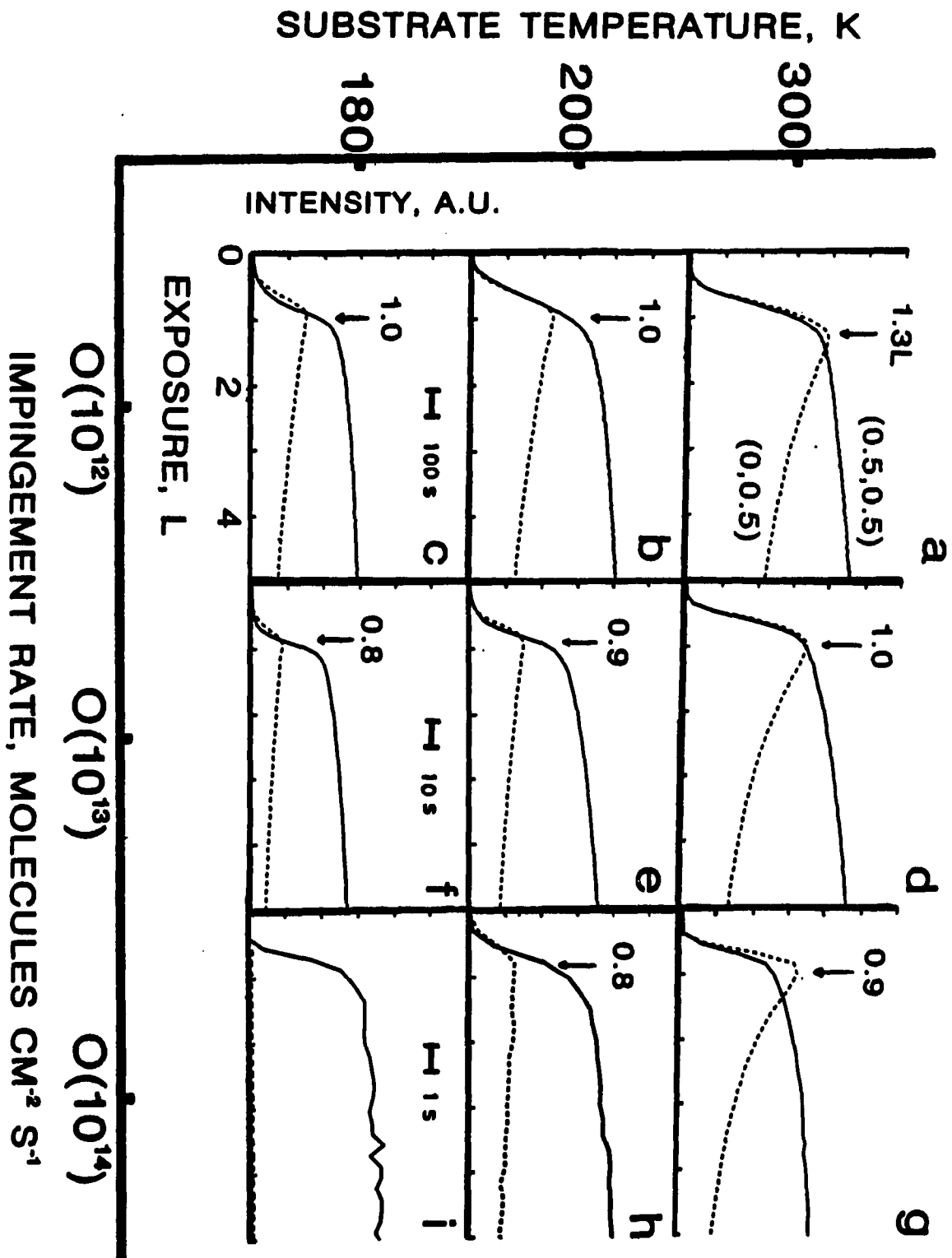
coverage increases above $1/4$ monolayers. We think that this may stem from the same phenomenon which gives rise to a metastable ordered $c(2 \times 2)$ (3), discussed in the following sections. That is, a particular ensemble of sites may be required for dissociative adsorption, and this ensemble is blocked out by the $p(2 \times 2)$ at $\theta = 1/4$ monolayers.

B. LEED Studies of Adsorption at 300 K and Below

Figure 5 describes the changes of half order spot intensities when oxygen dissociatively adsorbs on the surface at 300 K and below. We report nine results obtained under different conditions. Each panel in Fig. 3 represents a complete experiment where the spot intensity vs. exposure is plotted. The experimental conditions are indicated by two coordinates which represent the substrate temperature and the oxygen impingement rate, respectively. All the intensities are normalized to the $(1, 0)$ substrate beam of the clean surface at 300 K. No corrections are made for Debye-Waller attenuation at various temperatures. The conclusions which will be drawn in this paper are not affected by whether such a correction is made or not.

All experiments shown in Fig. 5 (except Fig. 5i) display two different steps of ordered adlayer growth. Below ~ 1 L, both $(0, 1/2)$ and $(1/2, 1/2)$ spots grow with almost the same rate; in this stage, the $p(2 \times 2)$ forms. Above ~ 1 L, the $(0, 1/2)$ spot begins to decrease while the $(1/2, 1/2)$ spot grows slowly which indicates the formation of the $c(2 \times 2)$. The panels in the first column of Fig. 5 (5a, 5b, and 5c) describe a relatively slow adsorption process at 300 K, 200 K, and

Figure 5. Changes of integrated spot intensities as a function of oxygen exposure during adsorption. Two LEED spots, (0, 0.5) and (0.5, 0.5), are shown. The experimental conditions for each feature are indicated by substrate temperature (right axis) and impingement rate (bottom axis). Arrows indicate the oxygen exposures where the maximum intensity of the p(2x2) structure is reached.



180 K, respectively. As indicated by arrows, the maximum intensity of the $(0, 1/2)$ spot, which stands for completion of the $p(2 \times 2)$ with its ideal coverage of 0.25 monolayers, is reached at about 0.8 to 1.3 L. This value holds true for all the experiments shown in Fig. 5 except one. This pressure- and temperature-independent growth of the $p(2 \times 2)$ structure is attributed to the rapid diffusion of atomic oxygen during adsorption (3). We have estimated the diffusion barrier to be 12.5 ± 1 kcal/mol (3).

It is interesting to compare the relative intensities of the $(1/2, 1/2)$ and $(0, 1/2)$ spots at ~ 1 L of exposure in Figs. 5a-5c, where the maximum intensity of the $(0, 1/2)$ spot decreases as temperature decreases. This trend is seen also in Figs. 5d-5f and Figs. 5g-5h and eventually no sign of $p(2 \times 2)$ appears in Fig. 5i. One might explain this phenomenon (Figs. 5a-5h) by the effect of Debye-Waller attenuation. However, if the same comparison is made along the row where the sample temperature is fixed as the gas impingement rate increases from left to right, (e.g., Figs. 5b, 5e, and 5h) the decrease in the maximum $(0, 1/2)$ spot intensity is still observed and is much more significant at higher adsorption rates. Based on this observation, we interpret our data by proposing that a new structure which weakens the $(0, 1/2)$ spot intensity is formed when experimental conditions are changed. Thus, the decrease in the $(0, 1/2)$ spot intensity is due to the decrease in the number of scatterers in the $p(2 \times 2)$ domains, not due to the Debye-Waller effects. As will be pointed out later, thermal vibrations of surface

atoms at 300 K and below probably do not cause a significant reduction in the intensity of a superstructure beam in these experiments.

The $p(2 \times 2)$ structure completely disappears in Fig. 5i. Note that two extreme conditions are employed in this experiment, which apparently serve to completely eliminate the $p(2 \times 2)$ structure: rapid adsorption rate (high oxygen pressure) and slow diffusion rate (low substrate temperature). The structure formed in Fig. 5i shows a $c(2 \times 2)$ diffraction pattern but the coverage at 1 L is 0.25 monolayers which is 0.25 monolayers less than the ideal coverage of a $c(2 \times 2)$ structure. We call this structure a "metastable $c(2 \times 2)$ ", since it is formed at low coverage by freezing the adatoms in the frame of a $c(2 \times 2)$ structure, most likely in two next nearest neighbor (n.-n.n.) sites, on the surface. The experimental conditions used in Fig. 5i manifest the mechanism involved in forming this metastable $c(2 \times 2)$ structure. The combined factors of adsorption rate (impingement rate) and diffusion rate (sample temperature) imply that the formation of the metastable $c(2 \times 2)$ is controlled by characteristics of the dissociative adsorption event itself.

C. Characteristics of the Metastable $c(2 \times 2)$ Structure

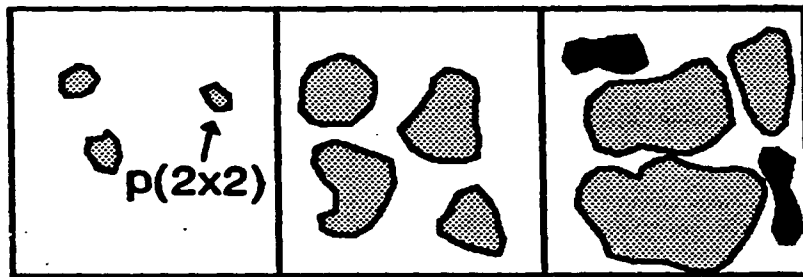
In this section we show experimental results which help us in characterizing the metastable $c(2 \times 2)$ structure. First we monitor the development of half order spot profiles under the conditions shown in Fig. 5a and Fig. 5i. These data reflect the average domain chord length as coverage changes. Some experimental results and a proposed model to

explain the metastable $c(2 \times 2)$ formation are shown in Fig. 6. In Fig. 6a-b, we show the growth of the (2×2) ordered layer under normal conditions, i.e., slow adsorption and fast diffusion (cf. Fig. 5a, 5d). In this case, the $p(2 \times 2)$ domains form first for the adatoms can respond to the interactions (3,10) between them properly. As coverage increases, small $p(2 \times 2)$ domains grow to larger ones (Fig. 6a). This idea is supported by examining the $(1/2, 1/2)$ spot profiles which are displayed in Fig. 6b. The continuous narrowing of the FWHM as a function of coverage implies that the $p(2 \times 2)$ domains grow to larger sizes. In Figs. 6c-d, the conditions for metastable $c(2 \times 2)$ formation are introduced, i.e., fast adsorption and slow diffusion (cf. Fig. 5i). Small clusters of $c(2 \times 2)$ domains are formed due to the kinetic restrictions mentioned above. As coverage increases, more and more local small $c(2 \times 2)$ domains are created but do not coalesce (Fig. 6c). This is probably because they are confined by kinetic limitations and boundaries between out of phase domains. In Fig. 6d, we show the changes of the $(1/2, 1,2)$ spot profiles which are measured under conditions in Fig. 5i. The profile of the $(1/2, 1/2)$ spot shows a broad peak with a high background intensity, and these characteristics persist up to 0.25 monolayers. The behavior of the $(1/2, 1/2)$ spot profile describes exactly what is proposed in the model. (Note that we are interested in the coverage range between 0.00 to 0.25 monolayers only.) The "near percolation" behavior of the $c(2 \times 2)$ domains which occurs as coverage approaches saturation (0.34 ± 0.02 monolayers) and causes a dramatic increase in domain sizes, is not discussed here (11,12).

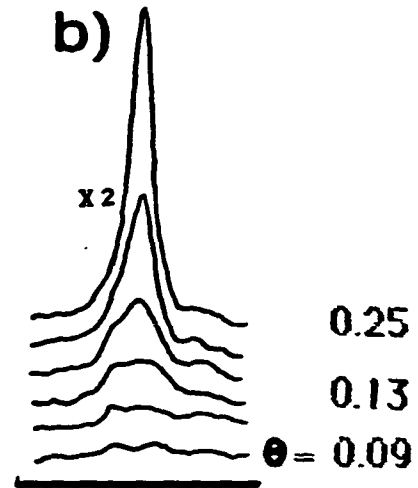
Figure 6. Proposed microscopic picture for growth of ordered structure on Pd(100) under various conditions.

- (a) Under conditions where diffusion is fast and adsorption is slow, small $p(2 \times 2)$ domains form first at low coverages. As coverage increases toward $1/4$ monolayers, small $p(2 \times 2)$ domains coalesce to form larger $p(2 \times 2)$ domains.
- (b) The $(1/2, 1/2)$ spot profile at various coverages supports what is proposed in (a). The profile becomes sharper as $p(2 \times 2)$ domains grow.
- (c) When adsorption is fast and diffusion is slow, small clusters of $c(2 \times 2)$ form at low coverages. As coverage increases, the number of metastable $c(2 \times 2)$ domains increases, but their average size is still small.
- (d) The $(1/2, 1/2)$ spot profile remains broad as coverage increases, implying a constant average domain size. The profile is broader than in (b) indicating the domain size is smaller in this case.

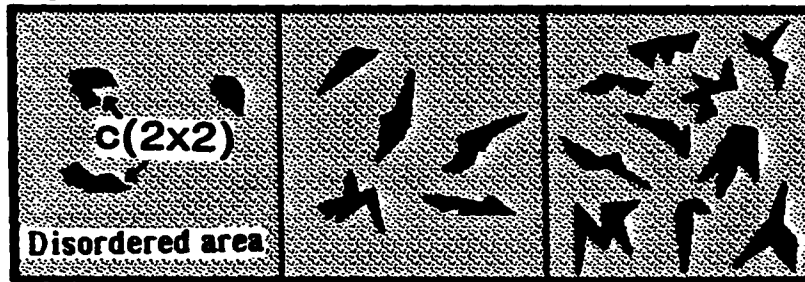
a)



b)



c)



$\theta \longrightarrow$

d)

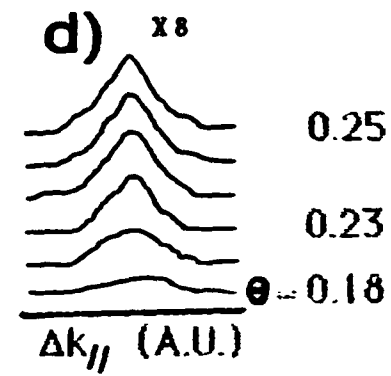


Figure 6 implies that the formation of the metastable $c(2 \times 2)$ is caused by different arrangements of adsorbates in their adsorption sites than a normal $p(2 \times 2)$ adsorption at low coverages. Since adsorbate induced reconstructions are commonly observed among transition metals, especially for group VIII B elements (13,14,15), we must consider this as one possible explanation for our metastable $c(2 \times 2)$. As pointed out in a recent study by Wenzel et al. (16), both C and O display a $c(2 \times 2)$ LEED pattern when adsorbed on a Ni(100) surface. The C adatoms induce a rotational movement of the underlying Ni atoms, whereas the O atoms do not. This is explained in terms of the difference in electronic configuration between C and O atoms. We believe that our metastable $c(2 \times 2)$ is not due to adsorbate-induced reconstruction like that induced by carbon on Ni(100). We prove our belief by showing the I-V curves of the $(1/2, 1/2)$ spot for both the metastable $c(2 \times 2)$, Fig. 7b, which is formed in Fig. 5i after 1 L of exposure and the $c(2 \times 2)$ structure, Fig. 7a, which is formed under normal conditions, i.e., after 30 to 50 L of oxygen exposure at room temperature. The close resemblance of these two figures implies that the arrangements of atoms within the unit cells of the two structures are identical. This rules out the possibility of reconstruction in the surface atoms of the metastable $c(2 \times 2)$.

Since the metastable $c(2 \times 2)$ is formed by kinetic "freezing" of adsorbates on the surface, this confinement in mobility of atomic oxygen should be removed by annealing the sample to higher temperatures (17). We show this result in Fig. 8a, in which a metastable $c(2 \times 2)$ ($\theta = 0.25$ monolayers) is annealed from 180 K to 380 K. The top panel in Fig. 8a

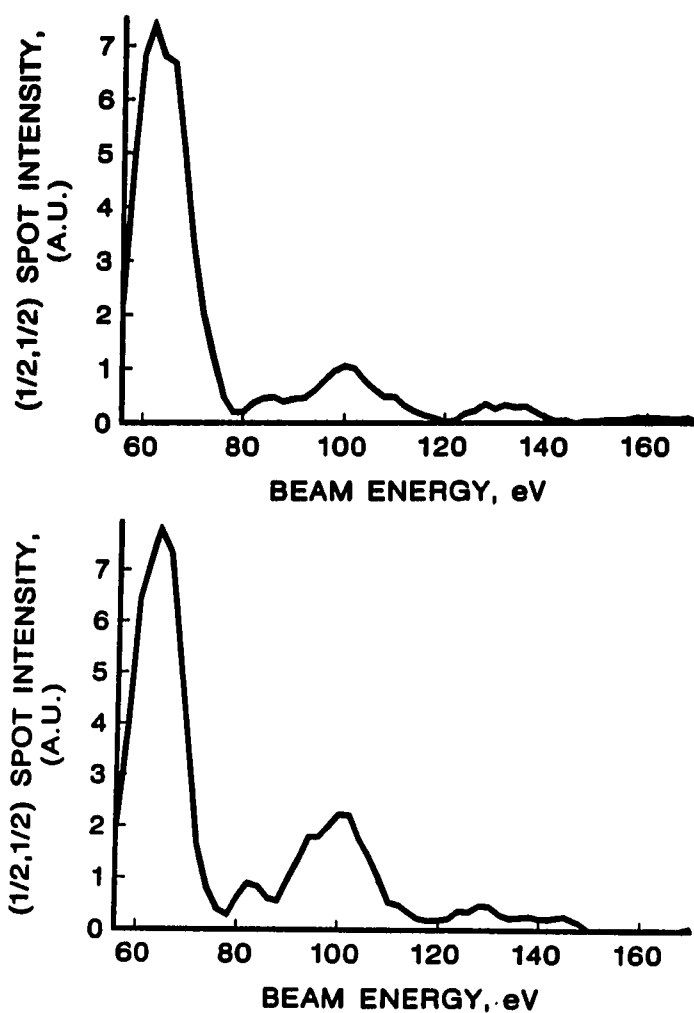


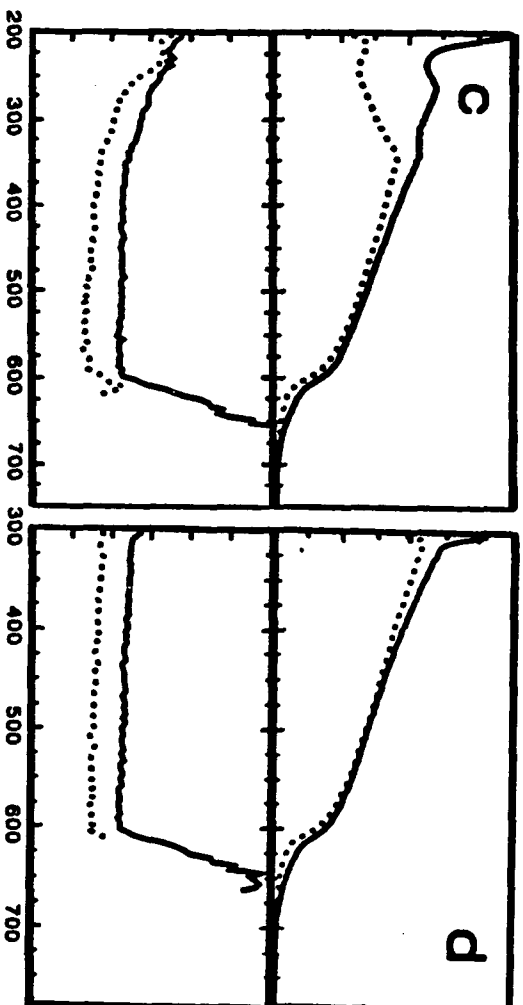
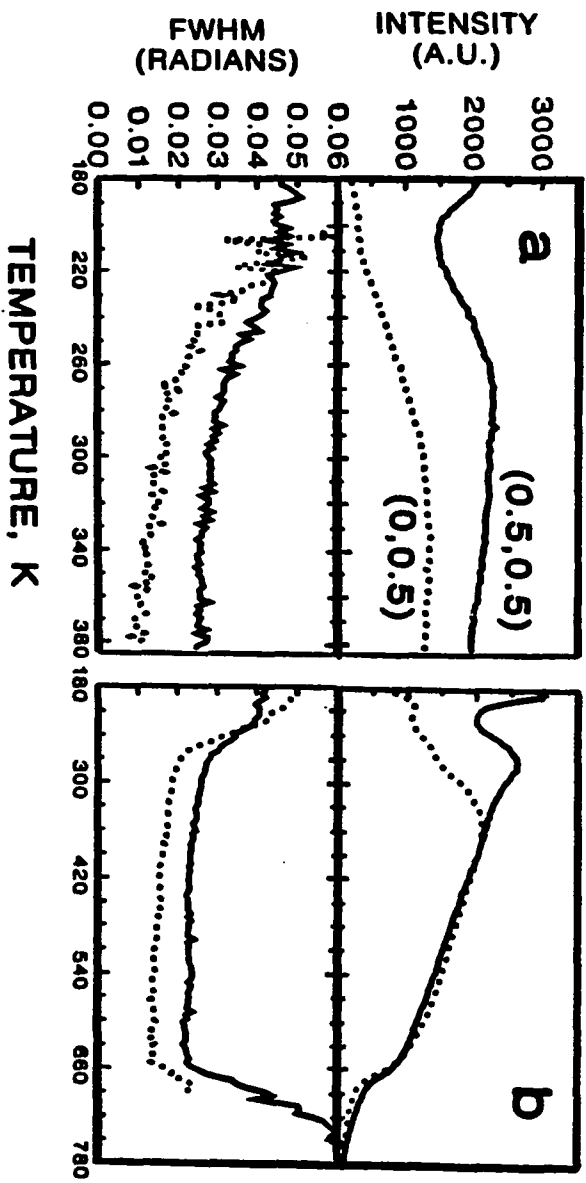
Figure 7. (1/2, 1/2) LEED spot intensity vs. beam energy plot.

- (a) $c(2 \times 2)$ pattern formed at room temperature after a 50 L of oxygen exposure.
- (b) Metastable $c(2 \times 2)$ structure formed under conditions of fast adsorption and slow diffusion after 1 L of oxygen exposure.

Figure 8. Changes of second order spots as a function of temperature during annealing. The top panels show the change of spot intensities and the bottom panels are spot profiles. The FWHM of the spot profile is expressed in units of radians which is calculated by using the island size broadening model (18). All the features in (a), (b), (c) and (d) represent ordered adlayers after adsorption of 1 L oxygen under different conditions. The heating rate used is 1 K/s.

(a) shows annealing of the metastable structure formed by using conditions described in Fig. 5i.

(b) (c) and (d) show annealing of p(2x2) structure formed by dosing 1 L oxygen (2×10^{-8} Torr x 50 sec.) at 180 K, 200 K and 300 K, respectively.



shows the changes in half-order spot intensities and the bottom panel shows the corresponding changes in FWHM of spot profiles. In addition to the data shown in Fig. 8a, we show three other experiments in Fig. 8b, 8c, and 8d which correspond to adsorption of 1 L of oxygen ($P_{O_2} = 2 \times 10^{-8}$ Torr) at 180 K, 200 K and 300 K, respectively. We can see from Fig. 8a, that the (0, 1/2) spot intensity increases as temperature rises and the p(2x2) domains grow correspondingly. These results clearly indicate that once the kinetic limits are removed, transformation from the metastable c(2x2) to the p(2x2) structure is feasible. This process is absolutely irreversible. In Fig. 8b and 8c, where there is less metastable c(2x2), however, the half-order spots act very similarly to those in Fig. 8a. By closely examining the half-order spots shown in Figs. 8a-c, we can summarize their behavior in the following four stages: 1) Below 220 K, the (1/2, 1/2) spot intensity drops very fast, while the (0, 1/2) spot intensity remains almost constant. The FWHM of both spots do not change very much as temperature increases. 2) Between 220 K and 300 K, the intensities of both spots increase rapidly. The corresponding spot profiles broaden rapidly as well. 3) Between 300 K and 600 K, both spot intensities decrease while their profile widths remain constant. This is typical for Debye-Waller attenuation. 4) Above 600 K, the adlayer starts disordering as shown by an abrupt decrease in spot intensities. Fig. 8d shows adsorption taking place at 300 K. As temperature increases both half-order spots decrease linearly in intensity till 600 K where disordering starts. The FWHM of both spots remain constant up to 600 K. The changes in stages (1) and

(2) shown in Figs. 8a-c are not observed here. The similarities in the half-order spots between Fig. 8a and Figs. 8b-c indicate that the metastable $c(2 \times 2)$ structure is always generated, more or less, when adsorption occurs below 300 K.

We interpret Figs. 8a-c as follows: When we anneal the low-temperature, oxygen-covered surface to 220 K (cf. stage 1), the metastable $c(2 \times 2)$ is destroyed. However, this process does not result in an increase of the $p(2 \times 2)$ domain size on the surface. This is perhaps, because the $p(2 \times 2)$ domains are too small to affect the $(0, 1/2)$ spot profile. As temperature reaches 220 K and above, the $p(2 \times 2)$ domains grow rapidly due to link of small domains (cf. stage 2). When temperatures are above 300 K, Debye-Waller effects become prominent, which causes the diffraction spot intensity to decrease but not the FWHM of the spot profiles (19). When adsorption occurs at 300 K or above, the formation of the metastable $c(2 \times 2)$ structure is not possible, and as a result, in Fig. 8d we do not observe the changes in stage 1 and 2 described previously when we anneal the sample. The fact that we can observe such clear variations of the half order spot intensity at temperatures below 300 K is probably because the Debye-Waller effects do not have a dramatic influence on the superstructure beam in this temperature range.

It is interesting to note that EELS studies performed by Nyberg and Tengstäl (2) show a 55 meV loss peak after adsorbing 1 L of oxygen at 80 K on Pd(100) which they attribute to atomic oxygen that resides in a

relatively dense configuration. We believe that what they observe is perhaps related to the metastable $c(2 \times 2)$.

In the annealing process shown in Fig. 8a, the transformation from the metastable $c(2 \times 2)$ to the $p(2 \times 2)$ is caused by removing the diffusion barrier, therefore, the coverage should not change in the range where this transformation occurs, i.e., between 180 K and 300 K. We perform two experiments to assure that the coverage indeed remains constant. First, our mass spectrometer shows no detectable changes in oxygen partial pressure which would signal desorption. Second, the AES signal of oxygen 510 eV and Pd 330 eV transitions are monitored and the result is shown in Fig. 9. Both results indicate that the coverage is conserved within the temperature range of interest.

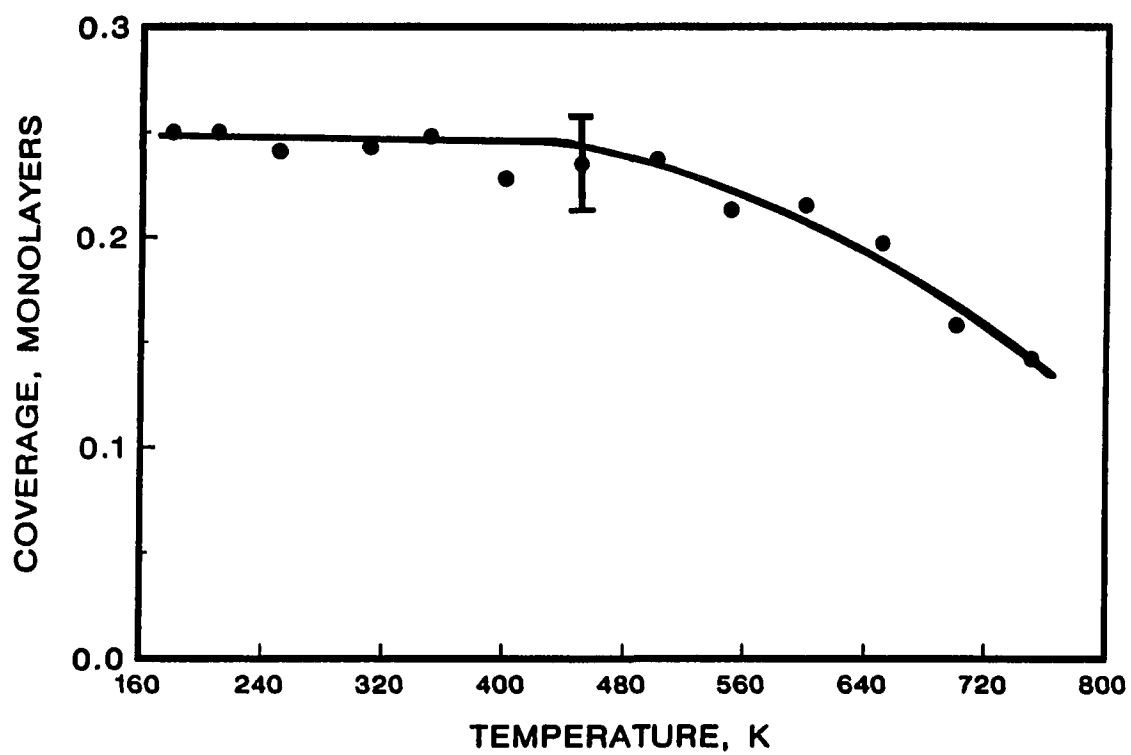


Figure 9. Changes of peak-to-peak heights ratio between oxygen 511 eV and Pd 330 eV transitions of the metastable $c(2 \times 2)$ structure during annealing.

IV. DISCUSSION

Dissociative chemisorption of gas molecules on metal surfaces can be described by two different mechanisms: direct and precursor-mediated. They can be illustrated and discussed by means of the potential energy diagram shown in Fig. 10. There are two energy minima in Fig. 10, corresponding to the dissociative chemisorption state (A_{ad} , atomic adsorbed state) and to the weakly adsorbed molecular state ($A_{2,ad}$, the mobile molecular precursor state), which are separated by an energy barrier with magnitude E_3 . In the direct adsorption process, the incident molecule dissociates upon initial impact with the surface. In other words, when the molecule crosses the potential curve (1) in Fig. 10 it is not trapped in the $A_{2,ad}$ state, instead, it dissociates and adsorbs into the A_{ad} state. In this case, the sticking probability is usually weakly dependent on the surface temperature, if at all. For the precursor mechanism, the molecule is first trapped in a weakly bound molecular state, $A_{2,ad}$, from which dissociation occurs by a thermally activated process. In this case, the sticking probability decreases rapidly with increasing surface temperature for a non-activated process. Since the precursor molecule is only a weakly bound species, it is often capable of diffusion over both the filled sites and empty sites on the surface. A mobile precursor molecule which moves over the bare sites is called an "intrinsic precursor" whereas one on top of filled sites is called an "extrinsic precursor" (20). Infinite mobility in the molecular precursor implies a coverage-independent sticking probability

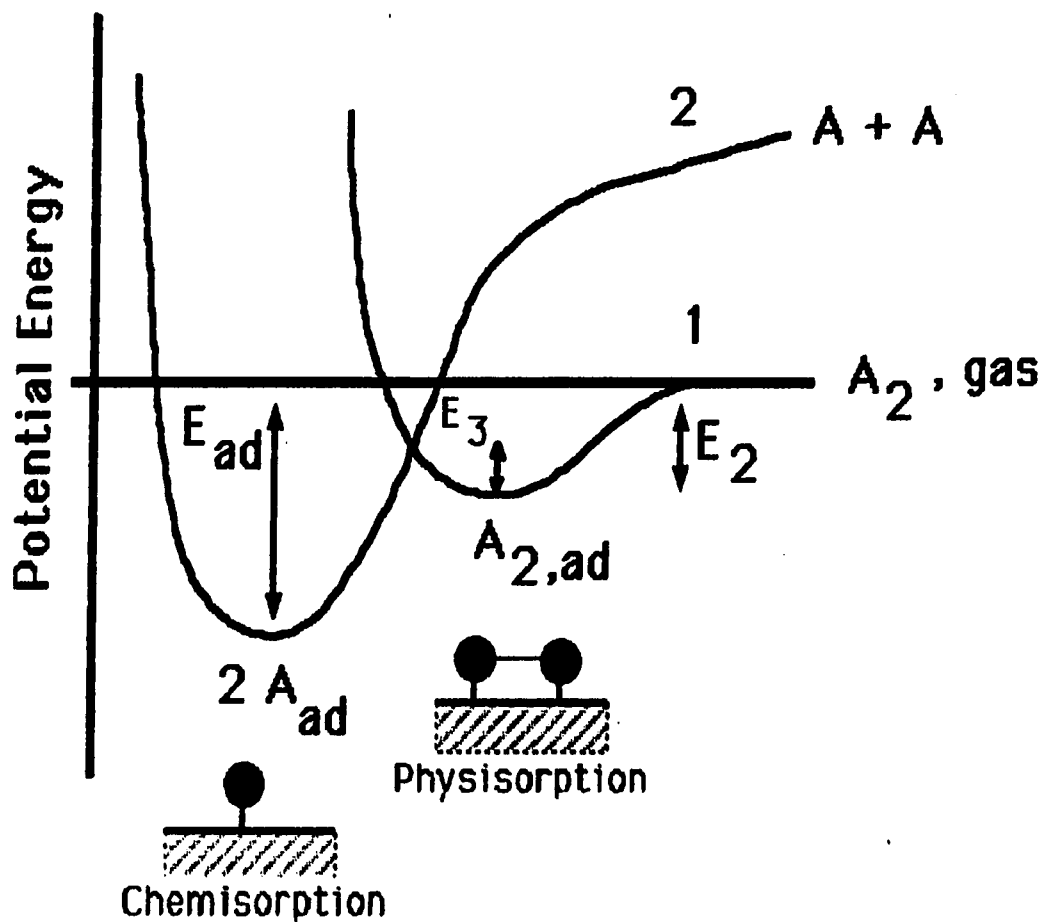


Figure 10. One dimensional potential energy diagram for a gas molecule A_2 which interacts with a metal surface. E_2 and E_3 represent the activation energies for desorption and dissociation of molecular adsorbed A_2 , respectively. Curve (1) is the molecular state and curve (2) is the dissociated state. The relative magnitude between E_2 and E_3 can be varied. If $E_3 > E_2$, adsorption is activated. Here we show the case $E_2 > E_3$ which stands for non-activated adsorption.

up to saturation coverage, i.e., any empty site can be found by an incident molecule, until the surface is filled. However, a mobile molecular precursor with a short life time may return to the gas phase before dissociation occurs. On the other hand, if all the available sites are occupied then further adsorption is impossible even for a precursor which has a very long lifetime.

In the present study, we can see that the initial sticking probability shown in Fig. 4 is temperature-dependent. This suggests that a molecular precursor state is involved in the adsorption process. Molecular precursors to dissociation are quite commonly observed (21-24). These molecular precursors are also often found to act as mobile precursors. Furthermore, it is seen from Fig. 4 that the sticking coefficient decreases as coverage increases at all temperatures. The shapes of the curves in Fig. 4 are qualitatively consistent with a mobile precursor of limited lifetime.

An alternative explanation for similar $s(\theta)$ data is offered by Campbell et al. (25) for the system $O_2/Pt(111)$. They propose a model in which the atomic adsorption potential well (cf. E_{ad} in Fig. 10) decreases as coverage increases. This change in the potential well thus explains the variation of the sticking probability as coverage increases. This model is equivalent to suggesting that adsorption at low coverages is preferentially into special sites with high sticking probability which decreases as these sites are filled. This model may be applicable to the system $O/Pd(100)$, because the formation of the metastable $c(2 \times 2)$ shown in Fig. 5i can be explained by it. When oxygen

molecules dissociatively adsorb on the surface under conditions described by Fig. 5f, the immobile oxygen atoms are trapped in their preferred adsorption sites on the surface, and in the meantime, the fast adsorption rate causes the surface to be covered rapidly by oxygen. The combined factors result in formation of the metastable $c(2 \times 2)$ structure. If this is the case then the $c(2 \times 2)$ structure contains the information of the sites necessary for O_2 dissociative adsorption. It is likely that O_2 requires two sequential diagonal sites with their n.n. sites empty (10). This is the eight-site ensemble model, shown in Fig. 11a, first proposed by Brundle et al. (10) to explain the dissociative adsorption of oxygen on the Ni(100) surface. It seems that this eight-site model gives a reasonable explanation to our experimental results.

In addition to the eight-site model, let us consider another model, the five-site ensemble model (shown in Fig. 11b), which also could result in the $c(2 \times 2)$ structure. Imagine that oxygen can dissociate, and adsorb as monomers. Assume that the translational energy carried by these "monomers" after they dissociate is so high that they can only respond to very strong n.n. repulsive interactions. As a result, a $c(2 \times 2)$ structure is formed. This kind of adsorption is very similar to random adsorption of monomers which exclude five sites each (11). Nevertheless, the five-site model is not considered as a proper model in explaining the adsorption process that takes place on the Pd(100) surface. Our argument is based on the experimental result which shows that the sticking probability approaches zero as the $p(2 \times 2)$ is

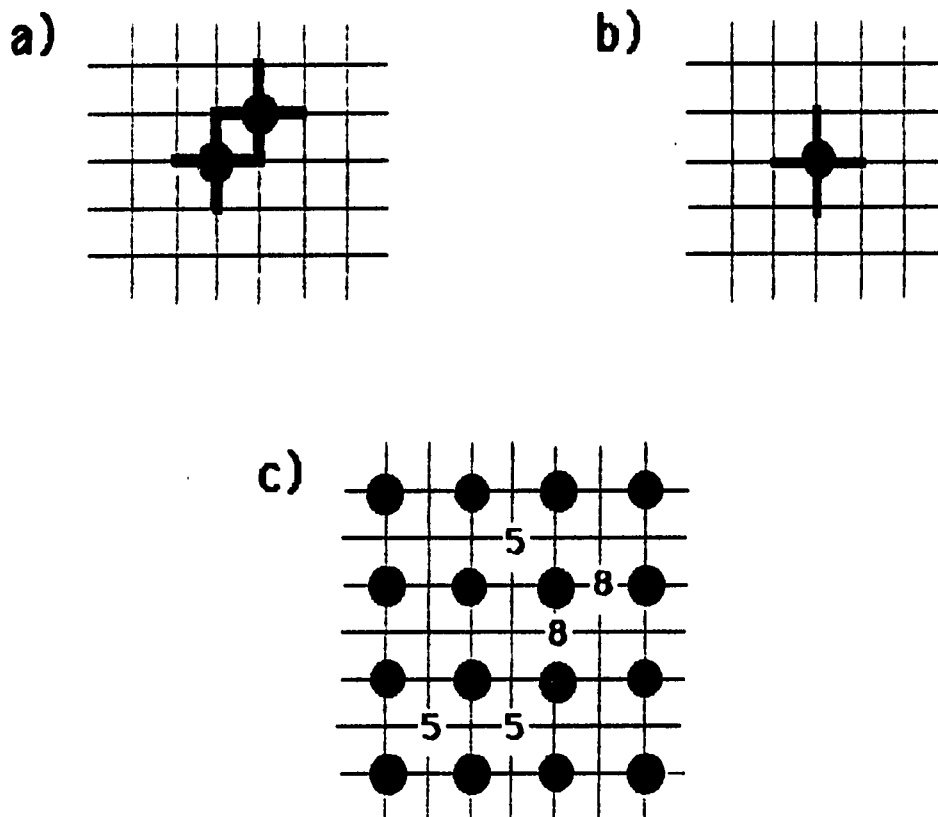


Figure 11a. The eight-site model. Oxygen atoms located on two diagonal sites with their n.n. sites empty.

Figure 11b. The five-site model. All the n.n. sites around the adsorbed oxygen atom are empty. Both a) and b) are part of the $c(2 \times 2)$ structure.

Figure 11c. A perfect $p(2 \times 2)$ leaves plenty of five-site ensembles (represented by "5") on the surface while no eight-site ensembles (represented by "8") can be found.

completed. This indicates that after the $p(2 \times 2)$ formation under equilibrium conditions, there are no more (or very few) appropriate sites, eight sites or five sites, left for oxygen to adsorb. This can be understood by assuming that a perfect $p(2 \times 2)$ structure can be created on an infinite square lattice. On such a $p(2 \times 2)$ covered surface, we can still find many five-site ensembles whereas all eight-site ensembles are destroyed. This is illustrated in Fig. 11c. It is certainly not possible to obtain a perfect $p(2 \times 2)$ due to defects on the surface. However, this ideal model tells us at least one thing which is that the eight-site model mimics the experimental results better than the five-site model. A computer simulation performed by Evans (11) for both eight-site and five-site models indicates that the probability of finding a five-site ensemble is four times higher than that of finding an eight-site ensemble at $\theta = 0.25$. There may be other models also applicable to the adsorption of oxygen on Pd(100); nevertheless, the eight-site model is the most plausible one at the present moment.

V. CONCLUSION

The major conclusions in this study are summarized as follows:

1) Oxygen adsorbs dissociatively on the Pd(100) surface at temperatures above 150 K via a molecular precursor intermediate, which is reflected in the temperature-dependence of the initial sticking coefficient. Additionally, an eight-site ensemble on the surface may be responsible for dissociative adsorption of oxygen.

2) A metastable $c(2 \times 2)$ structure can be formed at low coverage under conditions of slow diffusion and fast adsorption. The formation of such a $c(2 \times 2)$ structure suppresses the $p(2 \times 2)$ structure which is formed, under normal conditions, prior to the $c(2 \times 2)$ structure.

3) The metastable $c(2 \times 2)$ is always observed when adsorption occurs below 300 K. There are two sequential steps involved in converting a metastable $c(2 \times 2)$ to a $p(2 \times 2)$ during annealing: a) the metastable $c(2 \times 2)$ structure is destroyed; and b) small domains of $p(2 \times 2)$ link together to form larger domains.

VI. ACKNOWLEDGEMENTS

We acknowledge valuable discussions with Dr. J. W. Evans. Ames Laboratory is operated for the U. S. Department of Energy by Iowa State University under Contract No. W-7405-ENG-82. This work is supported by the Director for Energy Research, Office of Basic Energy Sciences.

VII. REFERENCES

1. E. M. Stuve, R. J. Madix and C. R. Brundle, Surf. Sci. 146 (1984) 155; 146 (1984) 179.
2. C. Nyberg and C. G. Tengstäl, Surf. Sci. 126 (1983) 163.
3. S.-L. Chang and P. A. Thiel, Phys. Rev. Lett. 59 (1987) 296.
4. K. H. Rieder and W. Stocker, Surf. Sci. 150 (1985) L66.
5. G. Ertl and J. Koch, Z. Physik. Chem. 69 (1970) 323.
6. T. W. Orent and S. D. Bader, Surf. Sci. 115 (1982) 323.
7. C. R. Brundle, R. J. Behm and J. A. Barker, J. Vac. Sci. Technol. A2 (1984) 1038.
8. J. W. Anderegge and P. A. Thiel, Rev. Sci. Instrum. 55 (1984) 1669.
9. S.-L. Chang and P. A. Thiel, J. Chem. Phys. 88 (1988) 2071.
10. J. W. Anderegge and P. A. Thiel, J. Vac. Sci. Technol. A4 (1986) 1367.
11. J. W. Evans, J. Chem. Phys. 87 (1987) 3038.
12. S.-L. Chang, D. E. Sanders, J. W. Evans and P. A. Thiel, "Surface Structures Determined by Kinetics Processes: Adsorption and Diffusion on Pd(100)," The Structure of Surfaces: Proceedings of The Second International Conference on the Structure of Surfaces (ICSOS-II) J. F. Van Der Veen and M. A. Van Hove, Eds., Springer Verlag, Berlin (1988) 231-237.
13. M. G. Cattania, V. Penka, R. J. Behm, K. Christmann and G. Ertl, Surf. Sci. 126 (1983) 382.

14. J. Goschnick, M. Wolf, M. Grunze, W. N. Unertl, J. H. Block, and J. Loboda-Cackovic, *Surf. Sci.* 178 (1986) 831.
15. K. Christmann, V. Penka, R. J. Behm, F. Chehab and G. Ertl, *Solid State Commun.* 51 (1984) 487.
16. L. Wenzel, D. Arvanitio, W. Daum, H. H. Rotermund, J. Stohr, K. Baberschke and H. Ibach, *Phys. Rev. B* 36 (1987) 7689.
17. G.-C. Wang and T.-M. Lu, *Phys. Rev. Lett.* 50 (1983) 2014.
18. G.-C. Wang, Ph.D Dissertation, University of Wisconsin-Madison, 1978.
19. G. A. Somorjai, *Chemistry in Two Dimensions: Surfaces* (Cornell University, Ithaca and London, 1981), p 169.
20. E. S. Hood, B. H. Toby and W. H. Weinberg, *Phys. Rev. Letters* 53 (1985) 2437.
21. D. A. King and M. G. Wells, *Surf. Sci.* 29 (1972) 454.
22. M. J. Grunze, J. Euhler, M. Neumann, C. R. Brundle, D. J. Auerbach and R. J. Behm, *Surf. Sci.* 139 (1984) 109.
23. C. T. Rettner and H. Stein, *Phys. Rev. Lett.* 14 (1987) 2768.
24. M. D. Williams, D. S. Bethune and A. C. Luntz, *J. Chem. Phys.* 88 (1988) 2842.
25. C. T. Campbell, G. Ertl, H. Kuipers and J. Segner, *Surf. Sci.* 107 (1981) 220.

PAPER III:

OXYGEN ON Pd(100): ORDER, RECONSTRUCTION, AND DESORPTION

OXYGEN ON Pd(100): ORDER, RECONSTRUCTION, AND DESORPTION

S.-L. Chang and P. A. Thiel

Department of Chemistry and Ames Laboratory-USDOE
Iowa State University
Ames, Iowa 50011 USA

ABSTRACT

We have investigated the temperature and coverage-dependent transformations of the ordered structures of oxygen on Pd(100). The four ordered structures are the chemisorbed $c(2 \times 2)$ and $p(2 \times 2)$ lattices, and the reconstructed $p(5 \times 5)$ and $(\sqrt{5} \times \sqrt{5})R27^\circ$ lattices. We present evidence that the $p(5 \times 5)$ reconstruction forms in an activated step from $c(2 \times 2)$ regions. The onset of $p(5 \times 5)$ formation is associated with an increase in oxygen sticking coefficient. In thermal desorption, there are three states which can be correlated directly with the structure of the adsorbed phase during desorption: At lowest coverage, the α state shows the traits of second-order kinetics and is due to desorption from a disordered adlayer. At higher coverage, the β state appears and is due to desorption from a layer with $c(2 \times 2)$ order. There is a lower barrier to desorption in the β state than in the α state because of the repulsive second-nearest-neighbor interactions in the $c(2 \times 2)$. At highest coverage, the sharp and narrow γ state emerges. This is accompanied by decomposition of the $(\sqrt{5} \times \sqrt{5})R27^\circ$ reconstruction, in which cooperative stabilization of the reconstruction by oxygen atoms effectively creates strong quasi-attractive oxygen-oxygen interactions. There are interesting similarities between the oxygen-stabilized reconstructions of Pd(100) and the initial stages of oxidation of Ni(100), as well as the oxygen-stabilized reconstructions of Pt(100). The data are obtained from low-energy electron diffraction coupled with

a computer-interfaced video camera, Auger electron spectroscopy, and thermal desorption spectroscopy.

I. INTRODUCTION

Palladium falls between Ni and Pt in the tenth column of the Periodic Table. Thus, it is appropriate that Pd(100) is similar to (and often intermediate between) Ni(100) (1) and Pt(100) (2-5) in the ways it interacts with oxygen. For both Ni(100) and Pd(100), chemisorbed oxygen can form two ordered structures on the unreconstructed metal lattice: p(2x2) and $(\sqrt{2} \times \sqrt{2})R45^\circ$ [the latter is commonly denoted c(2x2)], with ideal coverages (θ) of 0.25 and 0.50 monolayers, respectively. [We define one monolayer, $\theta = 1$, as the coverage at which there is one adsorbed particle per unreconstructed metal surface atom. At $\theta = 1$, there are 1.32×10^{15} particles cm^{-2} on Pd(100).] The p(2x2) on Pd was originally reported by Ertl and Koch (6), whereas Orent and Bader first described the c(2x2) on that metal (7). Both structures have been confirmed by Stuve et al. (8). The phase diagram of O/Ni(100) has been partially mapped out by Taylor and Park (9), and discussed also by Brundle et al. (10).

At still higher coverage, Ni forms NiO, a bulk-like oxide, in which the oxygen penetrates 2 or 3 layers deep from the beginning (1). Pd also appears to reconstruct in such a way that the surface mimics the structure of bulk PdO. The two reconstructions of Pd, first described by Orent and Bader (7), are p(5x5) and $(\sqrt{5} \times \sqrt{5})R27^\circ$. Because the oxygen in these phases is easily cleaned off by reaction with CO, Orent and Bader suggest that oxygen does not penetrate the Pd lattice in the fifth-order structures, but rather remains on top of the surface (7).

Assuming that the oxygen is only one layer deep, the $p(5 \times 5)$ and $(\sqrt{5} \times \sqrt{5})R27^\circ$ lattices probably have ideal coverages of 0.64 and 0.80 monolayers, respectively (7). Oxygen also stabilizes two reconstructions on Pt(100), with measured coverages of 0.44 and 0.63 monolayers (3).

The real-space representations of the four ordered structures associated with oxygen on Pd(100) are shown in Fig. 1. Note that there is no structural determination available for the two fifth-order lattices, and so the real-space structures shown for them are only reasonable possibilities.

In at least one respect, Ni, Pd and Pt react much differently with oxygen. Nickel forms a very stable bulk oxide, so that oxygen dissolution into bulk Ni is the only reaction which takes place when an oxygen-covered Ni(100) sample is heated in vacuum (1). No oxygen desorbs into the gas phase. However, the heat of formation of PdO is more positive than that of NiO by 163 kJ/mol (11). This is reflected in the fact that only about 0.1 monolayers of oxygen leave the Pd(100) surface via dissolution into the bulk (8; present work). At coverages above this limit, most surface oxygen desorbs into the gas phase when the sample is heated. On Pt(100), no oxygen penetrates into the bulk (2,3).

Thermal desorption spectra were first measured for O/Pd(100) by Stuve et al. (8), who found three distinct spectral features. The spectra bear a strong qualitative similarity to those of O/Pt(100) (2,4). Norton and coworkers have shown that one of the desorption

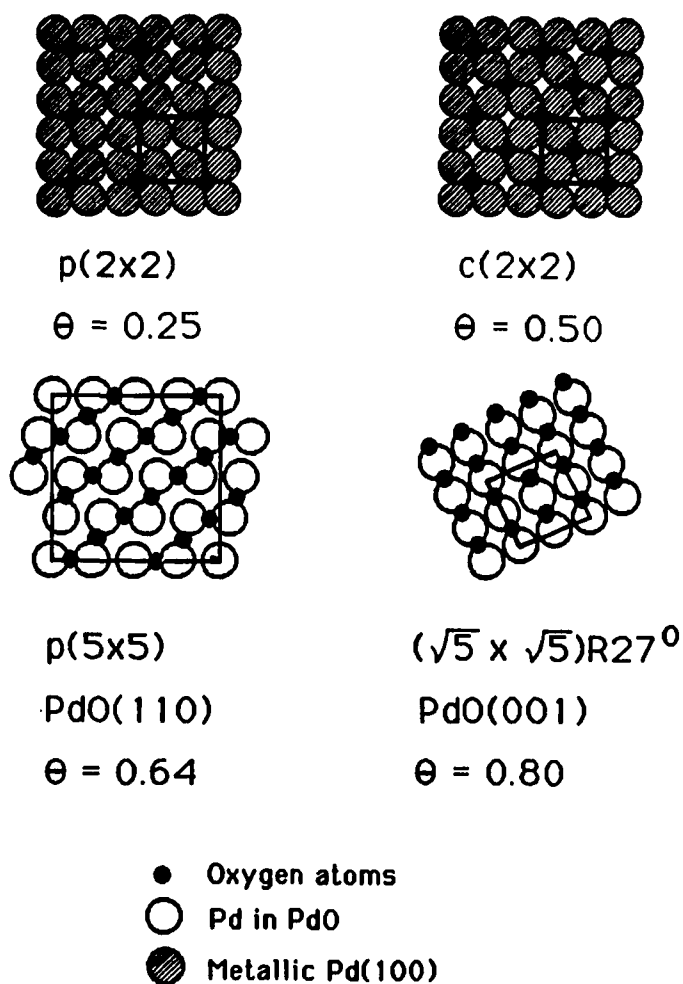


Figure 1. Real space representations of the ordered oxygen phases observed on Pd(100). For clarity, the underlying Pd(100) lattice is omitted in the p(5x5) and $(\sqrt{5} \times \sqrt{5})R27^\circ$ structures, but the respective unit cells are drawn. The Pd lattice must contract by 0.8 and 1.3%, respectively, to achieve coincidence with PdO as shown.

features on Pt is due to interconversion between the two oxygen-stabilized reconstructions (2,3). In this work, we report evidence that a desorption state of O/Pd(100) is similarly due to decomposition of a reconstructed phase, leaving oxygen on an unreconstructed substrate. The desorption process (while the metal is changing phase) occurs in a very narrow temperature range. Similar narrow, sharp desorption peaks are reported also for H/Ni(110) (12,13), H/Pd(110) (14), and H/W(100) (15) where they are related to decomposition of reconstructed phases.

The phase diagram of O/Pd(100) is relatively complex because of the presence of the reconstructed phases. Principles which apply to adsorbate-induced reconstructive transitions (as opposed to displacive transitions) in other systems (2,3,12,16-19) shall be useful in the current discussion, and so we review them here. There is evidence that the energetic driving force for these adsorbate-induced metal phase transitions is provided by the difference between the adsorbate's heat of adsorption, ΔH_a , on the reconstructed surface and the unreconstructed surface. For the sake of argument, let us consider the case where the magnitude of ΔH_a is larger for the reconstructed phase. Then if the surface is structurally inhomogeneous (i.e., partly reconstructed and partly unreconstructed), adsorbed atoms or molecules are selectively trapped in reconstructed areas. This is because the energetic inhomogeneity of the surface sets up a barrier against adsorbate diffusion out of the patch where its heat of adsorption is higher (14,15). Furthermore, a minimum local coverage is necessary to maintain

the reconstruction within a given area. If coverage in the area falls below this critical value, the metal locally reverts to the unreconstructed phase. The formation of the reconstructed phase proceeds via a nucleation and growth mechanism, and consequently exhibits a strong hysteresis in temperature. These principles were first proven true for CO/Pt(100) (16,17), and various aspects of them are reported applicable to H/Ni(110) (12,18), O/Ni(110) (19), and O/Pt(100) (2,3) as well. In this paper, we use these ideas to understand the reconstructions of O/Pd(100).

It is clear that there are many processes which must be considered in this system: diffusion and ordering, reconstruction, bulk dissolution, and desorption. In this paper we discuss those structural changes within the surface layer(s) which take place at high temperatures, $T \gtrsim 400$ K. These include two-dimensional phase transitions, as well as the irreversible processes of desorption and dissolution. We do not discuss kinetics of transitions which take place irreversibly at lower temperature, including adsorption and diffusion-limited adsorbate ordering. These are described elsewhere (20,21).

II. EXPERIMENTAL PROCEDURES

The experimental apparatus consists of a stainless steel ultrahigh vacuum chamber with commercial single-pass cylindrical mirror analyzer (CMA) and coaxial electron gun, optics for low-energy electron diffraction (LEED), ion bombardment gun, and mass spectrometer. The pressure in the chamber is 2×10^{-10} Torr or less prior to each experiment. The mass spectrometer, an EAI 250 quadrupole, is multiplexed by a PDP 11/23 computer, which allows (effectively) simultaneous measurement of up to eight mass intensities. The sample is mounted on a manipulator described elsewhere (22). Temperature is controlled through a feedback circuit designed by Herz et al. (23). The LEED data are acquired with a computer-interfaced Video system which has been also described elsewhere (24). The parameters used in Auger electron spectroscopy (AES) are these: 2 kV incident beam energy, 5 V peak-to-peak modulation amplitude, and 0.75 μ A sample current.

During initial cleaning, the main impurities in the Pd(100) sample are sulfur, carbon and phosphorous. These are removed by elevating the crystal temperature stepwise by 50 K in vacuum. During each mild annealing, contaminants (except carbon) can be seen in the Auger spectrum as they segregate to the surface. Argon ion sputtering is then applied for three to five minutes (current density of ca. 10^{14} ions $\text{cm}^{-2} \text{s}^{-1}$) to remove these impurities from the surface. This cycle is repeated from room temperature to about 1200 K until no more contamination can be detected by AES. After other impurities are gone,

carbon is removed by adsorbing oxygen at room temperature and flashing the sample in vacuo to 1200 K. This is repeated until no more CO is formed as a reaction product during the flash. The small excess of oxygen remaining at the end can be removed by annealing the surface in vacuo at 1200 K for about 2 minutes. Oxygen is used to titrate carbon in this way at the beginning of each day's experiments, and AES is used to check that no other contaminants are present after the titration. Furthermore, sample cleanliness during the LEED or AES experiments is checked periodically by heating the sample in vacuum after the LEED or AES experiment is finished, and monitoring the desorption spectra of O₂ and CO simultaneously. We find that this is rather sensitive to contamination generated by the electron guns and hot filaments used in LEED and AES. If surface contamination is present, we observe desorption of CO and abnormalities in the oxygen desorption spectrum. In the data reported here, such contamination has been carefully excluded.

The sample is heated resistively, so the magnetic field induced by the electrical current distorts the LEED pattern during heating. To avoid this distortion during data acquisition, the computer shuts off the heating current momentarily while data are acquired. The heating rate in the LEED experiments is about 1 K/s. The LEED beam voltage is 64 eV and the beam current is 0.5 to 0.7 μ A.

III. EXPERIMENTAL RESULTS

A. Coverage Calibration

The calibration of coverages in this system is not straightforward. In LEED, the $p(2 \times 2)$ reaches a maximum in intensity at exposures of 1.0 ± 0.3 L (1 L $\equiv 10^{-6}$ Torr-sec), for temperatures between 200 and 400 K. At this exposure, we assume that $\theta = 0.25$ (6,7), although non-zero temperature and crystal imperfections may cause an unknown, but probably small, deviation from this value. This is our firmest calibration of coverage. In principle, the time-integrated thermal desorption peak area can provide a measure of the number of adsorbed atoms, but in this system some oxygen leaves the surface via bulk dissolution in addition to desorption. For exposures of 0.2 L or less, only bulk dissolution takes place; no desorption occurs. The Auger spectra (see below) indicate that this corresponds to dissolution of 0.10 ± 0.03 monolayers, in agreement with previous work (8,25). If we assume that the absolute amount of oxygen which dissolves into the bulk is constant for oxygen exposures above 0.2 L, then the TDS peak areas do provide a measure of oxygen coverage as a function of exposure, which is shown in Fig. 2A. We believe that this presents the most reliable measure of absolute coverage, at $\theta > 0.25$. The coverages calculated in this way are qualitatively consistent with all of our LEED observations, and are also consistent with Orent and Bader's report that the saturation coverage exceeds 0.50 monolayers (7). We expect that these coverage values are accurate to within about ± 0.05 monolayers;

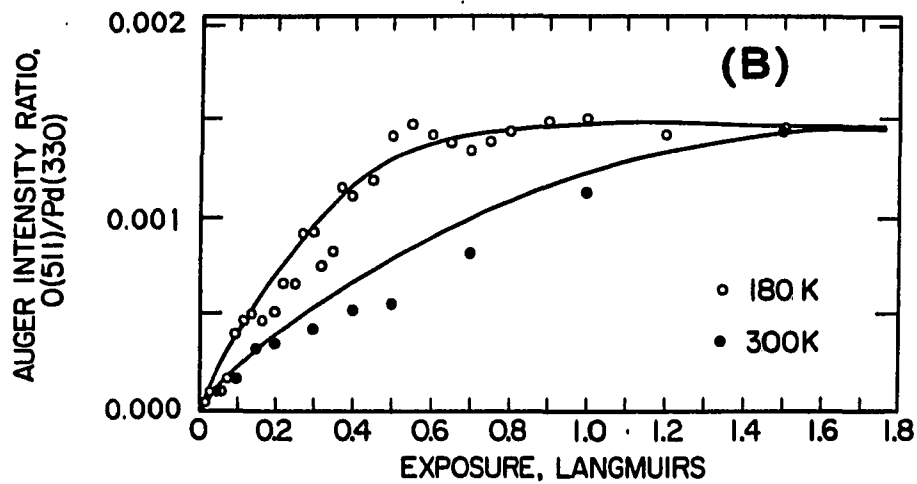
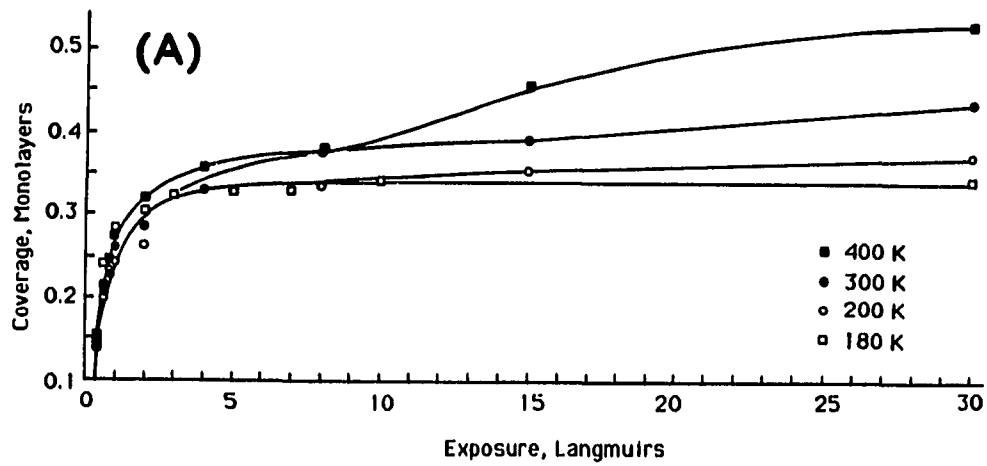


Figure 2a. Thermal desorption peak areas as a function of oxygen exposure at four adsorption temperatures.

Figure 2b. Ratio of Auger intensities for oxygen (511 eV) and Pd(330 eV) as a function of oxygen exposure at two adsorption temperatures.

however, the uncertainty is larger if our assumption that the amount of dissolution is coverage-independent should prove grossly incorrect.

Auger electron spectroscopy is commonly used to measure coverages as well. We find that if we use the ratio of peak-to-peak heights for the oxygen 511 eV and Pd 330 eV transitions in the $dN(E)/dE$ spectrum, and fix $\theta = 0.25$ at 1 L, the oxygen uptake measured with AES drops off abruptly and reproducibly at $\theta > 0.25$, even though TDS and LEED clearly show that the oxygen coverage increases above 0.25. We therefore judge that the AES data are not useful, for reasons unknown, at high oxygen coverages. Perhaps the cross-section for electron-stimulated desorption increases strongly at $\theta \gtrsim 0.25$, although Orent and Bader report successful AES measurements of higher oxygen coverages on Pd(100) (7). The AES data at lower coverages (where bulk dissolution renders TDS largely useless) are shown in Fig. 2B. Two facts should be noted. First, an exposure of 0.2 L corresponds to a coverage of about 0.10 ± 0.03 monolayers, assuming that $\theta = 0.25$ at 1 L exposure and assuming that AES signal varies linearly with coverage at $\theta < 0.25$. As noted above, this amount is lost completely to bulk dissolution during TDS. Second, the initial sticking coefficient increases as temperature decreases, implying the existence of an intrinsic mobile precursor. This is discussed more fully elsewhere (20,21).

B. LEED Patterns

Figure 1 shows the four ordered structures observed for oxygen on Pd(100) (6-8), and Fig. 3 shows the corresponding LEED patterns. In

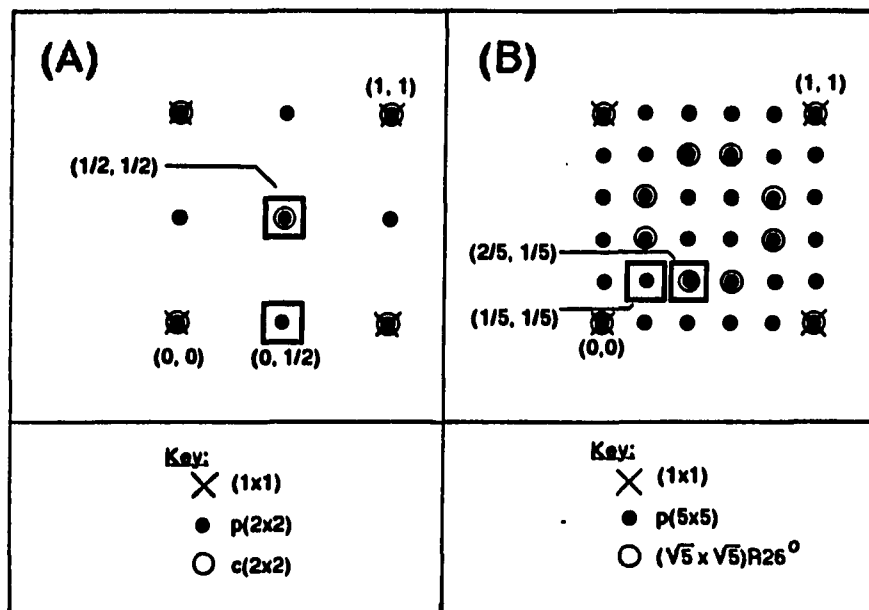


Figure 3. Schematic representation of the LEED patterns observed for oxygen/Pd(100). The spots which are chosen for measurement are enclosed by rectangles. Note that two domains of the $(\sqrt{5} \times \sqrt{5})R27^\circ$ structure must be present to produce all the spots shown for it in Fig. 3B.

order to monitor the coverage- and temperature-dependence of these structures, we measure integrated peak intensities and profiles of the diffraction spots enclosed by rectangles, as shown in Fig. 3. In Fig. 3A, the p(2x2) and c(2x2) patterns are overlaid. The ideal coverages of these structures are 0.25 and 0.50 monolayers, respectively (6,7). It can be seen that the (0, 1/2) spot provides a measure of only the p(2x2) characteristics, but the (1/2, 1/2) spot is common to both the p(2x2) and c(2x2) patterns. In Fig. 3B the reciprocal-space lattices of the two fifth-order structures are illustrated. These high-coverage structures have been ascribed to the oxygen-induced reconstructions of the Pd surface shown in Fig. 1 (7). The ideal coverages of these structures, denoted p(5x5) and $(\sqrt{5} \times \sqrt{5})R27^\circ$, are 0.64 and 0.80 monolayers, respectively (7). For these patterns, we measure characteristics of the (1/5, 1/5) spot [unique to the p(5x5)] and the (2/5, 1/5) spot [common to both fifth-order patterns].

The fact that two of the structures, c(2x2) and $(\sqrt{5} \times \sqrt{5})R27^\circ$, have no unique diffraction feature presents a problem for interpretation of the intensity data. In order to distinguish pure p(5x5) from coexistent p(5x5) + $(\sqrt{5} \times \sqrt{5})R27^\circ$ structures, for instance, our approach is to compare the (1/5, 1/5) and (2/5, 1/5) spot intensities under conditions where only p(5x5) is believed present. In our data, the ratio of (1/5, 1/5) to (2/5, 1/5) intensities has a constant value of 1.0 ± 0.5 under these conditions. Thus, we expect that the intensity of the (1/5, 1/5) spot will be 1.0 ± 0.5 times that of the (2/5, 1/5) spot if only p(5x5) is present, and less than 0.5 times as intense if $(\sqrt{5} \times \sqrt{5})R27^\circ$ is

present as well. Similarly, the ratio of $(0, 1/2)$ to $(1/2, 1/2)$ spot intensities varies from 0.9 to 1.5 under conditions where only $p(2 \times 2)$ is believed to be present ($0.13 < \theta < 0.26$ and $200 \text{ K} < T < 400 \text{ K}$).

C. LEED Patterns During Adsorption

Figure 4 shows the changes in LEED spot intensities which occur during adsorption at 400 K. The $(0, 1/2)$ spot and $(1/2, 1/2)$ spot both brighten quickly at low exposures. The $(0, 1/2)$ spot reaches maximum intensity at an exposure of 1 L, presumably because the coverage passes through the ideal value for the $p(2 \times 2)$ structure. As adsorption continues, the $(0, 1/2)$ spot dims rapidly and the $(1/2, 1/2)$ spot intensifies gradually. The data are quite similar when adsorption occurs at 300 K (20,21). However, at 10 L exposure ($\theta \sim 0.40$) and at 400 K, several changes occur simultaneously. First, the $(1/5, 1/5)$ spot and $(2/5, 1/5)$ spot intensities emerge simultaneously from zero. Their relative intensities indicate that only $p(5 \times 5)$ is present as these spots brighten. Second, at this same exposure, the $(0, 1/2)$ spot abruptly stops its rapid decline in intensity; as the $p(5 \times 5)$ grows at $\theta \gtrsim 0.4$, the $(0, 1/2)$ spot decays only gradually. Remember that this spot is unique to the $p(2 \times 2)$ structure, and so the data show clearly that appearance and growth of $p(5 \times 5)$ somehow alleviates the rapid destruction of $p(2 \times 2)$ which takes place at lower coverages. Third, at $\theta \sim 0.40$, the $(1/2, 1/2)$ spot begins an abrupt decline in intensity. These data indicate that the $p(5 \times 5)$ structure grows primarily at the expense of the $c(2 \times 2)$ as coverage increases. In repeated experiments, these changes

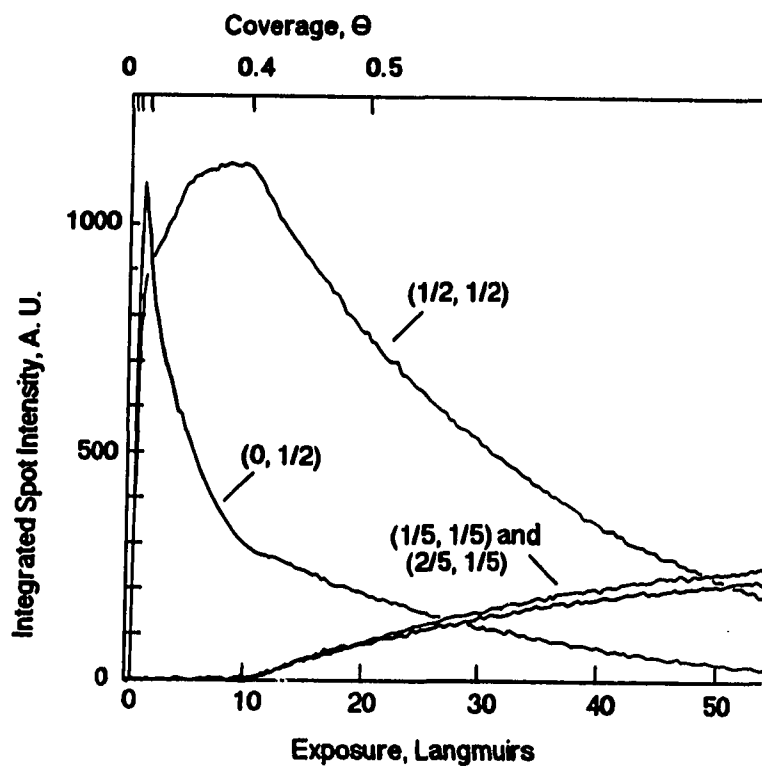


Figure 4. Variation of LEED spot intensities as a function of exposure and coverage during adsorption at 400 K. The oxygen pressure is 3×10^{-8} Torr.

always occur simultaneously and reproducibly at $\theta = 0.40 \pm 0.02$ ($\epsilon = 10 \pm 1$ L), at 400 K. The data are very similar when adsorption is carried out at 500 K, except that the p(5x5) emerges first at a higher exposure, $\epsilon = 14 \pm 1$ L. Upon adsorption at 600 K and $P = 6 \times 10^{-8}$ Torr, no fifth-order structures develop at all. Instead, at exposures above ~ 10 L, the LEED pattern shows a diffuse ring which is characteristic of Pd0 (7,26).

We do not observe the $(\sqrt{5} \times \sqrt{5})R27^\circ$ pattern during adsorption at 400, 500, or 600 K, in spite of Orent and Bader's report (7) that it forms at $T \sim 570$ K. It may be that our exposures or pressures are too low for its formation ($\epsilon \lesssim 100$ L, $P \lesssim 10^{-6}$ Torr). Alternatively, it may be that the $(\sqrt{5} \times \sqrt{5})R27^\circ$ structure can form only in a very narrow temperature range, somewhere between 500 and 600 K. Our thermal desorption results, described in a following section, favor the latter hypothesis.

Figure 2A shows that there is an increase in the rate of oxygen uptake (sticking coefficient) at $\theta \sim 0.40$ during adsorption at 400 K; this increase is absent during adsorption at 300 K. The increase coincides exactly with appearance of the p(5x5) during adsorption at 400 K, as shown in Fig. 4. It is absent at 300 K because no p(5x5) forms during adsorption at 300 K. The combined evidence strongly indicates that formation of the p(5x5) is an activated process, requiring temperatures of ca. 400 K to occur. In turn, this indicates that the p(5x5) is a metal reconstruction rather than a simple chemisorbed phase.

In the latter case, the barrier to ordering would be (typically) overcome at much lower temperature, 200-300 K (20,21). Furthermore, the oxygen sticking coefficient is enhanced by appearance of the p(5x5) phase (vide infra).

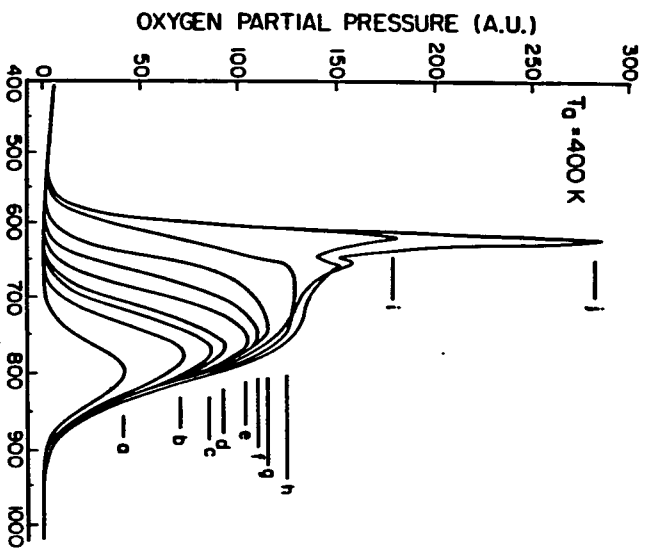
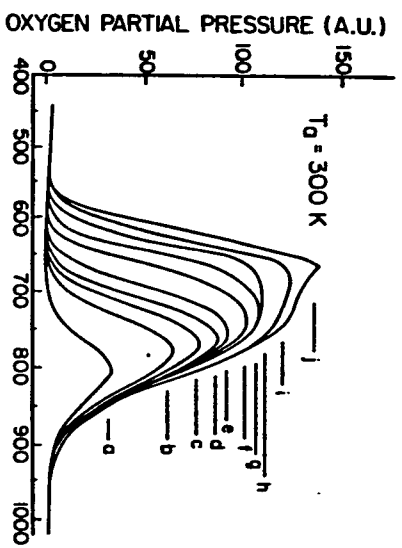
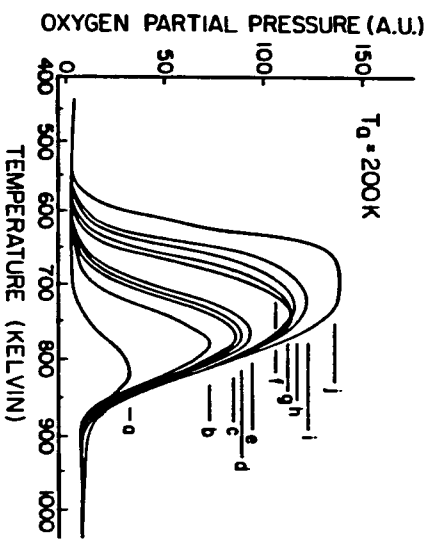
D. Desorption States

In Fig. 5 we present three families of desorption spectra, corresponding to three different adsorption temperatures, T_a . In all cases, at exposures of 2 L or less ($\theta < 0.30$), there is a single symmetric desorption peak, α , with a maximum which shifts to lower temperature as coverage increases. These are the characteristics of second-order (recombinative) desorption kinetics. At exposures between 2 and 15 L ($0.30 < \theta < 0.45$), a shoulder develops at lower temperatures. When this feature, β , is saturated by adsorption at 300 to 400 K, it forms a sharp cusp positioned at 650 to 665 K. This feature is reported also by Stuve et al. (8), who attribute it to repulsive interactions between oxygen atoms. In our experiments, it first appears at those coverages where the c(2x2) structure is replacing the p(2x2) during adsorption, and so it is reasonable that next-nearest-neighbor (n.n.n.) repulsions present in the c(2x2) structure are related to the β feature in TDS.

Figure 6 compares the experimental TDS data at $\theta < 0.45$ with numerical analysis of the second-order thermal desorption rate equation. The increase in peak width as a function of θ is not characteristic for "normal" second-order desorption and requires a coverage-dependence

Figure 5. Thermal desorption spectra of oxygen on Pd(100) following oxygen adsorption on Pd(100) at three adsorption temperatures. The heating rate is 1 K s^{-1} . The exposure for each set of curves is:

- | | |
|-----------|-----------|
| (a) 0.4 L | (f) 4.0 L |
| (b) 0.6 L | (g) 8.0 L |
| (c) 0.8 L | (h) 15 L |
| (d) 1.0 L | (i) 30 L |
| (e) 2.0 L | (j) 60 L |



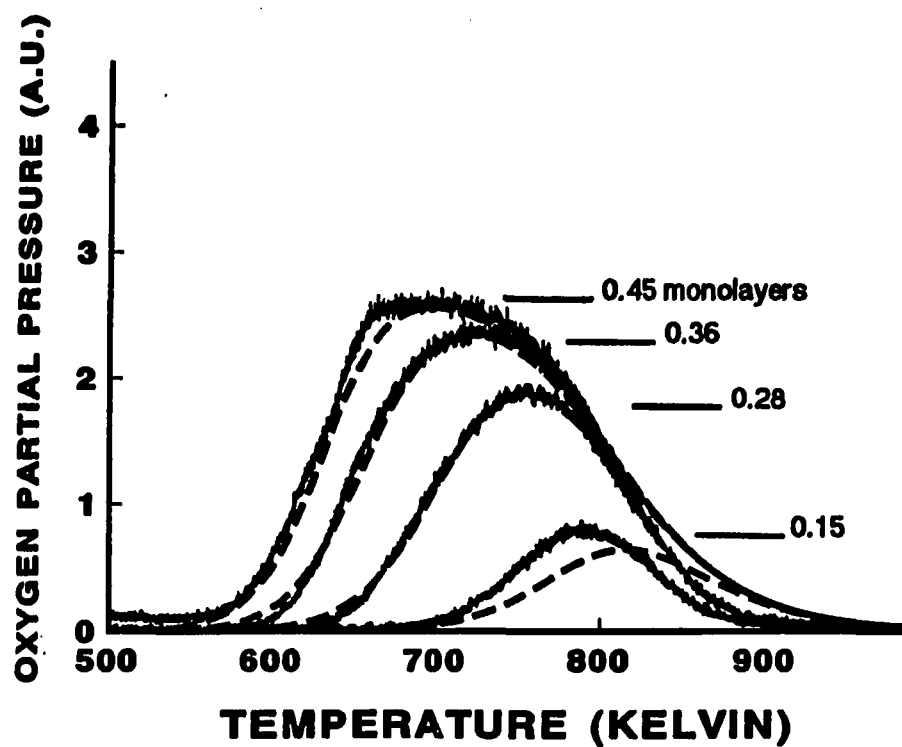


Figure 6. Kinetic analysis of the α , and β desorption states. Solid lines: experimental data. Dashed lines: results of numerical analysis of the second-order desorption rate equation, using parameters described in text.

either in the desorption barrier, or ν , or both. Therefore, repulsive interactions are incorporated in the simulations via a coverage-dependent desorption barrier, after Wang (27). The positions, widths, and shapes of the experimental spectra are fit well by a model which includes n.n.n. repulsive interactions of 3.3 kJ/mol. The nearest-neighbor (n.n.) repulsions are considered infinitely strong, which is approximated by setting the maximum coverage at $6.6 \times 10^{14} \text{ cm}^{-2}$. Interactions farther away than n.n.n. sites are ignored. The value of 3.3 kJ/mol is of the expected order of magnitude (28): interaction energies of 8.8 to 2.9 kJ/mol are estimated from the phase diagram of O/W(110), for instance (29). The model further assumes an activation barrier to desorption of 160 kJ/mol in the limit of zero coverage, and a coverage-independent preexponential rate factor, ν , of $5 \times 10^{-6} \text{ cm}^2 \text{ s}^{-1}$. While three adjustable parameters do not allow a unique fit to the data, the point here is that physically reasonable parameters can provide a good fit to the data.

At values of θ below about 0.30 monolayers, agreement between the experimental desorption data and the model curves is not as good as at higher θ (cf. Fig. 6). The model curves overestimate the peak width and temperature at low θ . This may reflect a coverage dependence in the desorption rate parameters other than the repulsive interactions included in our model.

Finally, at $\theta \gtrsim 0.50$, a third feature, γ , appears, with a peak maximum first distinguishable at 620 K. Note that this state is very sharp and narrow. The γ state is extremely sensitive to the adsorption

temperature. As Fig. 5 shows, it is completely absent after exposures up to 60 L at 200 K; it is barely discernible in the discontinuity of slope on the leading edge of the spectrum which follows 60 L exposure at 300 K; and it is very pronounced following high exposures at 400 K. The strong dependence on adsorption temperature suggests that adsorption into this state is activated.

We find no evidence for an analog to the β_3 desorption state of O/Pt(100) (2). In O/Pt(100), β_3 is not a distinct state; rather, it is a slowly decreasing background at high temperatures (2). We do not observe this in the O/Pd(100) system in spite of careful examination of the TDS curves at temperatures up to 1100 K. On Pt(100), this state accounts for 0.1 monolayers of oxygen and is ascribed to oxygen adsorbed at defects in the reconstructed surface (2).

E. Bulk Dissolution

Figure 7 shows the ratio of Auger intensities of oxygen and Pd as a function of temperature, following adsorption of 0.25 monolayers or less at 200 K. At low coverage ($\theta \lesssim 0.10$), Auger indicates loss of oxygen already between 300 and 400 K. Because TDS shows no evidence for any desorption at these coverages, the rather abrupt drop in Auger ratio between 300 and 400 K probably signals the transition between chemisorbed oxygen and oxygen dissolved in the bulk. At higher coverages, the loss of oxygen measured by Auger occurs less abruptly; instead, there is a gradual decrease up to the desorption onset at 600 to 700 K (cf. Fig. 5).

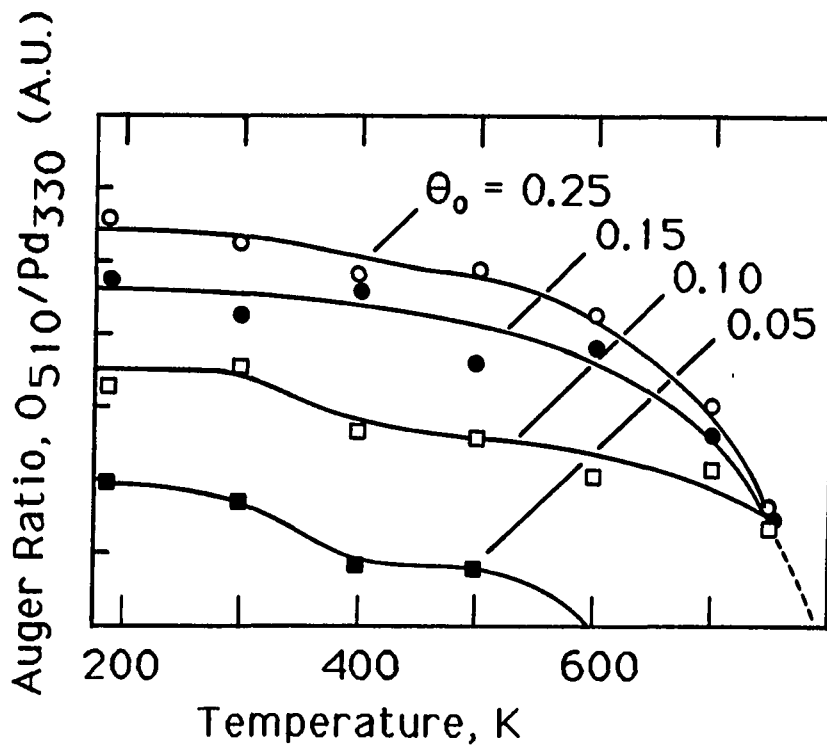


Figure 7. Ratio of oxygen to palladium peak heights in the $dN(E)/dE$ Auger spectrum as a function of temperature. Each curve is labelled with the initial coverage of oxygen, θ_0 .

F. Temperature-Dependent LEED Data

Figure 8 shows representative results from LEED experiments when an oxygen-covered sample is heated in vacuum. The corresponding thermal desorption data from Fig. 5 are shown also for comparison. The LEED and TDS experiments are done separately, but the heating rate and other experimental parameters are held constant so the results from the two experiments can be compared directly. The top panel(s) of each frame shows the changes in intensity of LEED spots which occur when the sample is heated, while the bottom panel shows the thermal desorption spectrum, for the appropriate initial coverage of oxygen.

The oxygen adlayers used in the experiments of Fig. 8 are prepared at adsorption temperatures between 200 and 400 K. However, Fig. 8 shows only those changes in the LEED patterns which occur at 400 K and above, since that is the regime of primary interest in this paper.

At the very lowest coverages of oxygen ($\theta < 0.1$) no ordered structures form, either upon adsorption or after heating. Also, no oxygen desorbs. Figure 8A shows that when the coverage is slightly higher, $\theta \sim 0.20$, only the α desorption state is populated. At this coverage, the $p(2 \times 2)$ structure forms upon adsorption and disorders well before the onset of desorption. This is shown by the variation of $(0, 1/2)$ spot intensity as a function of temperature in Fig. 8A. Orent and Bader also report that disordering precedes desorption on Pd(100) at $\theta \sim 0.25$ (7).

Figure 8B shows the result when the coverage is increased to $\theta = 0.28$. At this coverage, which is slightly above the ideal coverage of

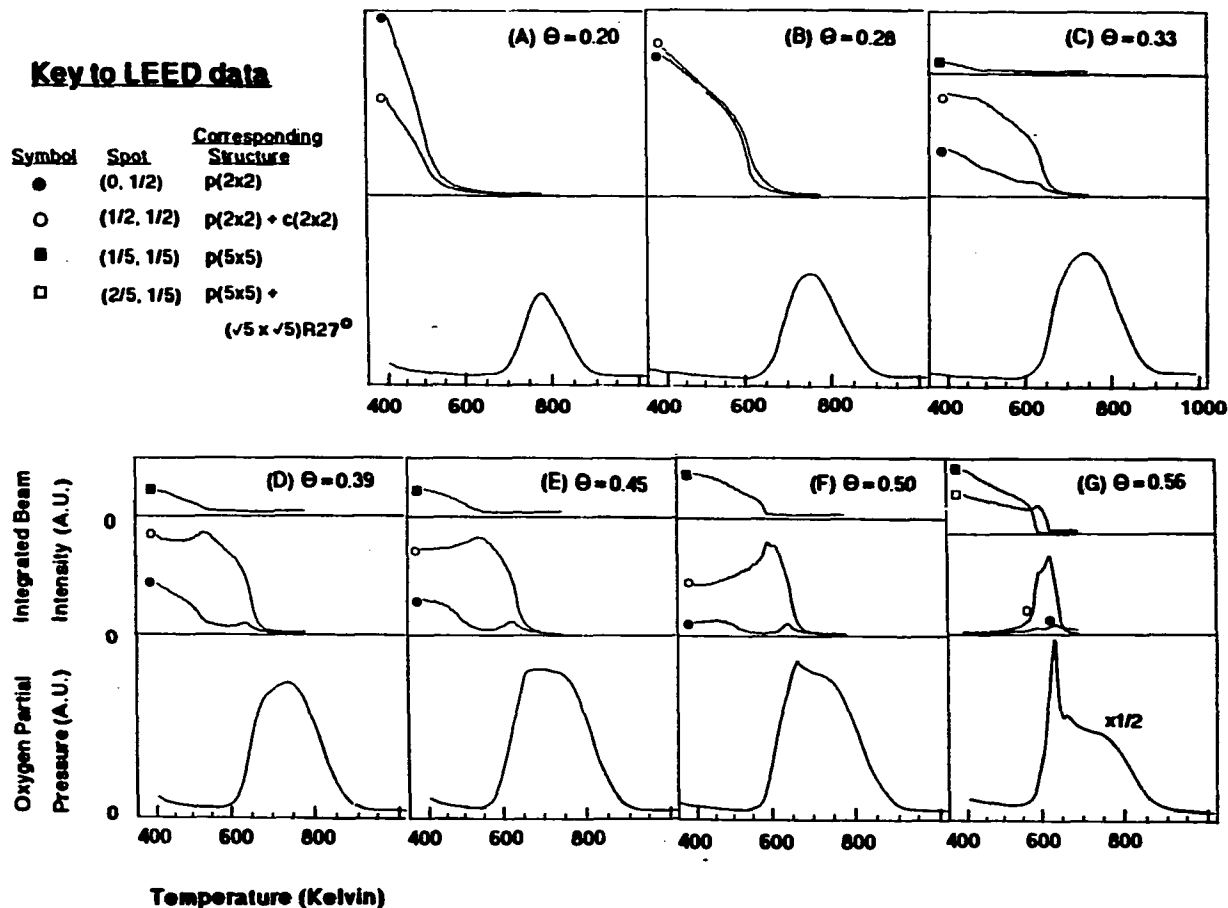


Figure 8. Variation of LEED spot intensities as a function of temperature starting from the oxygen coverages indicated. The heating rate is 1 K s^{-1} . For comparison, thermal desorption spectra taken at the same heating rate are shown also.

the $p(2 \times 2)$ at $T = 0$ K, the thermal desorption spectra still show only the symmetric α state. Now the adsorbed layer loses all long-range order just as desorption begins; both events coincide at about 620 K.

To summarize the data represented in Figs. 8A-B, the coverage range between about 0.10 and 0.30 monolayers is characterized by apparent second-order desorption from a disordered layer. The only ordered structures at these coverages, the $p(2 \times 2)$ and $c(2 \times 2)$, disorder below the desorption threshold.

At higher coverages ($0.30 \lesssim \theta < 0.50$), the thermal desorption spectra are distinguished by the emerging β shoulder. At the same time, the LEED data become more complex, as shown by Figures 8C, D and E. At these coverages there are three important diffraction features: the $(1/2, 1/2)$ spot, the $(0, 1/2)$ spot, and the $(1/5, 1/5)$ spot.

Figures 8D and E show that the the first of these three, the $(1/2, 1/2)$ spot, abruptly brightens between 470 and 540 K, and at the same time the other two LEED spots disappear. Therefore, the amount of oxygen in the $c(2 \times 2)$ structure increases while that in $p(2 \times 2)$ and $p(5 \times 5)$ lattices decreases at these temperatures and coverages. When desorption begins, at higher temperatures, Figures 8C-E show that there is considerable intensity still in the $(1/2, 1/2)$ spot. The $p(2 \times 2)$ contributes little, if any, to the intensity of the $(1/2, 1/2)$ spot as desorption begins. This shows that the $c(2 \times 2)$ is stable up to and somewhat past the onset of desorption in the β feature.

The second main feature is the $(0, 1/2)$ spot. Its intensity falls gradually with increasing temperature, presumably due to the

Debye-Waller effect; it drops suddenly toward zero at the same temperatures where the $(1/5, 1/5)$ spot disappears (e.g., at 540 K in Fig. 8D). However, shortly after desorption begins, it reappears and passes through a small maximum in intensity at 630-635 K. This is true for all coverages above about 0.30 monolayers (see Figs. 8C-G). At its maximum, the $(0, 1/2)$ spot is rather sharp.

We propose the following explanation for the brief appearance of the $p(2 \times 2)$ during desorption. Coverage decreases during desorption from the β shoulder. As a result of this alone, the $p(2 \times 2)$ brightens, but then it is quickly overcome by loss of intensity due to disordering. For instance, Fig. 8B shows that the $(0, 1/2)$ spot at $\theta = 0.28$ still has some intensity at 630 K, even though it has passed the point of inflection and is tailing off to zero. Regardless of its origin, the transient $p(2 \times 2)$ which forms during desorption is obviously a fingerprint for decomposition of the $c(2 \times 2)$ adlayer.

The ratio of intensities of the $(1/2, 1/2)$ and $(0, 1/2)$ spots at the beginning of the experiments of Figs. 8C-F is too large to represent a pure $p(2 \times 2)$ lattice; rather, a mixture of $p(2 \times 2)$ and $c(2 \times 2)$ must be represented by the half-order spots.

Third, a faint $p(5 \times 5)$ pattern is present by 400 K and is shown by the $(1/5, 1/5)$ spot in Figs. 8C-E. This phase disappears completely by 490 K at $\theta = 0.33$ (Fig. 8C) and by 540 K at $\theta = 0.39$ (Fig. 8D). The disappearance of the $(1/5, 1/5)$ spot during heating consistently coincides with an increase in the $(1/2, 1/2)$ spot intensity. In Figs. 8D and E, note also that the $(0, 1/2)$ spot intensity mimics that of the

(1/5, 1/5) spot between 400 and 550 K. These data imply that a mixed p(5x5) + p(2x2) adlayer exists below some critical temperature (which depends on coverage); as temperature increases above this point it converts to a homogeneous c(2x2) adlayer. In every case, the p(5x5) is destroyed well before the onset of desorption, and so at these coverages the p(5x5) plays no direct role in the desorption process. Note that the minimum coverage required to form p(5x5) is lower during annealing in vacuum, where $\theta_{\min} \sim 0.30$ (cf. Fig. 8C), than during adsorption at elevated temperature, where $\theta_{\min} \sim 0.40$ (cf. Fig. 4).

To summarize the data at $0.30 \lesssim \theta < 0.50$ (Figs. 8C-E), there is a mixture of p(2x2) and p(5x5) at $T = 400$ K. Some c(2x2) is present as well. The p(5x5) + p(2x2) mixture converts to c(2x2) well before desorption begins and plays no direct role in the desorption process. During the initial stages of desorption, the c(2x2) is still largely intact; it disintegrates during desorption from the β shoulder. As the c(2x2) is destroyed by loss of oxygen, a transient p(2x2) forms and then disorders. Desorption from the disordered layer then continues to completion in the α state.

At $\theta \gtrsim 0.50$, the γ state appears in thermal desorption spectra. The LEED data for this coverage range are illustrated in Figs. 8F and G. At $\theta = 0.50$, Fig. 8F shows that there is still some intensity in both of the half-order spots at 400 K, but at $\theta = 0.56$ (Fig. 8G), both of these spots are entirely gone. In other words, as coverage increases from 0.50 to 0.56 monolayers, both the p(2x2) and c(2x2) disappear at 400 K. At $\theta = 0.50$, the (0, 1/2) spot disappears at significantly lower

temperature than does the $(1/5, 1/5)$ spot, i.e., these two features do not disappear in parallel as at lower coverages. As the $(0, 1/2)$ spot vanishes, the $(1/2, 1/2)$ beam brightens, indicating again a conversion from $p(2 \times 2)$ to $c(2 \times 2)$. But here the $p(5 \times 5)$ remains throughout: both at $\theta = 0.50$ and $\theta = 0.56$, the $(1/5, 1/5)$ spot persists a little past the temperature where desorption begins, meaning that the $p(5 \times 5)$ is much more stable than at lower coverage. As the $p(5 \times 5)$ disappears, the $c(2 \times 2)$ appears or intensifies further. At slightly higher temperature the $c(2 \times 2)$ begins to decompose, as desorption from the β state begins. The data now resemble those at lower coverages, particularly in that a transient $p(2 \times 2)$ appears just as desorption from the β state ends. Desorption from the disordered layer then continues to completion in the α state.

Most remarkable, however, are the data of Fig. 8G ($\theta = 0.56$), where the $(2/5, 1/5)$ spot remains very briefly after the $(1/5, 1/5)$ spot drops to zero intensity. This signals the appearance of the $(\sqrt{5} \times \sqrt{5})R27^\circ$ structure, and coincides exactly with desorption from the γ state. The $p(5 \times 5)$ structure disappears shortly after desorption starts. Based upon these data, we conclude that the γ state is due mainly to decomposition of the $(\sqrt{5} \times \sqrt{5})R27^\circ$ structure, although there may be some contribution from the $p(5 \times 5)$ as well.

G. Reversibility

We have investigated the reversibility of the changes which take place below the desorption onset in Figs. 8D-E, i.e., the $p(5 \times 5) +$

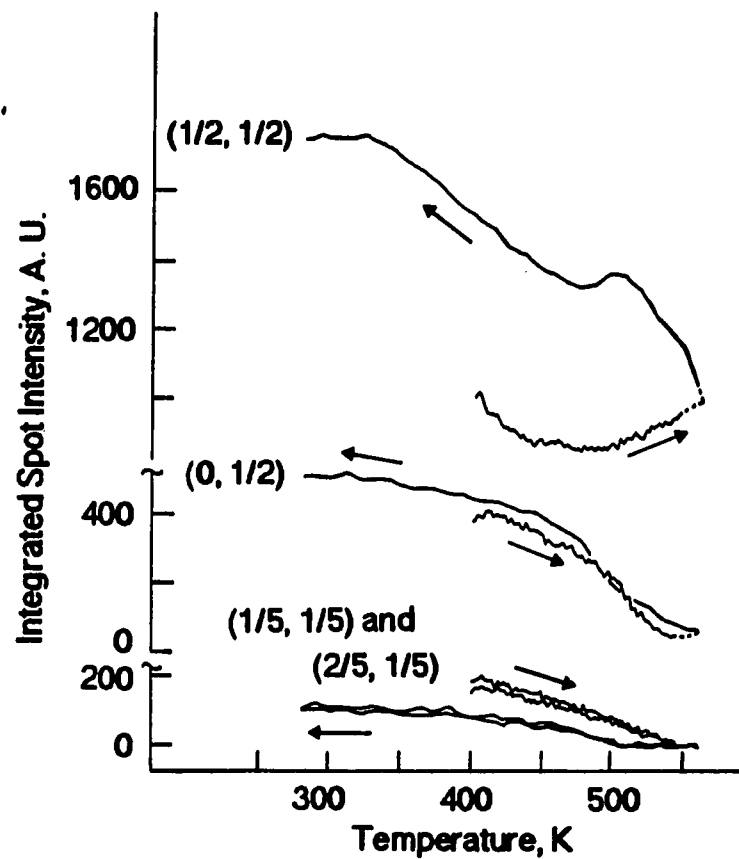


Figure 9. Successive heating and cooling cycles between 400 and 550 K. The initial coverage is 0.45 monolayers. The heating rate is 1 K s^{-1} . The cooling rate is 3 K s^{-1} .

$p(2 \times 2) \rightarrow c(2 \times 2)$ transition. The data are shown in Fig. 9. Note that the transition is reversible. The transition occurs at lower temperature during cooling than during heating. This may indicate a true hysteresis in the system, although we have not investigated the width of this loop as a function of cooling and heating rates. A detailed discussion of the reversibility between different phases can be found in reference 21.

IV. DISCUSSION

A. Interaction Between Ordered Structures

The interaction between the $p(2 \times 2)$, $c(2 \times 2)$, and $p(5 \times 5)$ structures is fascinating and complex. The $p(2 \times 2)$ and $c(2 \times 2)$ are chemisorbed structures, apparently similar to the (2×2) structures of oxygen on Ni(100) (1,10). On the other hand, our data show that formation of the $p(5 \times 5)$ can occur only at $T \gtrsim 400$ K, consistent with the hypothesis that it is an activated reconstruction rather than simply a chemisorbed phase. Orent and Bader (7) report that a minimum temperature of 470 K is necessary to overcome the barrier to its formation, slightly higher than the minimum temperature of 400 K shown in our data. During adsorption at 400 K, the $p(2 \times 2)$ structures, with an ideal coverage of 0.25 monolayers, forms at total coverages of $0.10 < \theta < 0.25$. At $0.25 < \theta < 0.40$, the $c(2 \times 2)$ grows at the expense of the $p(2 \times 2)$. Its ideal coverage is 0.5 monolayers. At $\theta > 0.40$, the $p(5 \times 5)$ appears and grows, — before the $p(2 \times 2)$ has completely disappeared. Its initiation coincides with an increase in oxygen sticking coefficient (cf. Fig. 2A and 4). Furthermore, the $p(5 \times 5)$, for which $\theta_{ideal} = 0.64$, forms during adsorption mainly at the expense of the $c(2 \times 2)$. Any model for the interaction between the three phases must be consistent with all of these observations.

We propose a model based on the energy diagram of Fig. 10, which shows the differential heat of adsorption, E , as a qualitative function of metal surface structure (reaction coordinate). The energy per atom

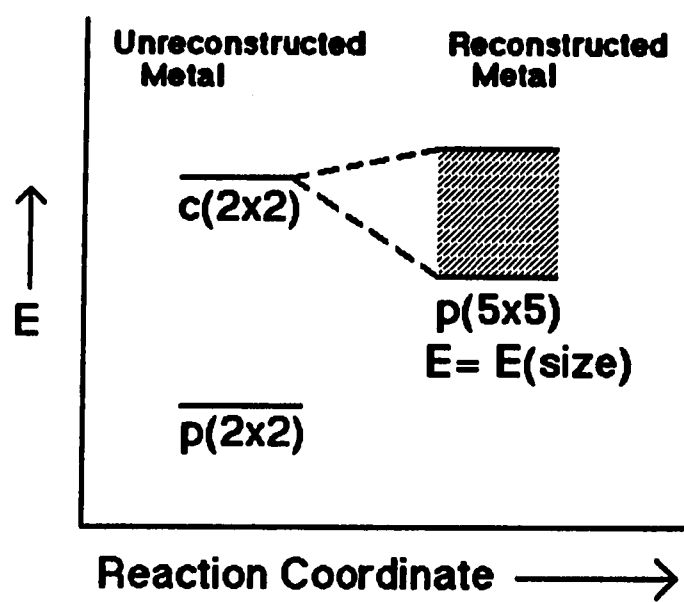


Figure 10. Progression of energy levels postulated for O/Pd(100).

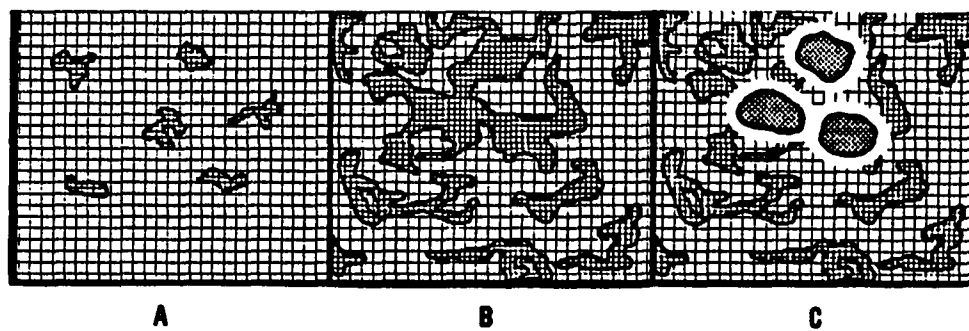
is most negative in the $p(2 \times 2)$ structure, and this is the preferred ordered phase up to $\theta = 0.25$. The energy per atom is more positive in the $c(2 \times 2)$, but this structure is nonetheless adopted at $\theta > 0.25$ because the total energy of the adsorbed layer, θE , is still lower than that of the saturated $p(2 \times 2)$, i.e., adsorption is still thermodynamically favored at $\theta > 0.25$. Both (2×2) structures are present on the unreconstructed metal.

As total coverage increases past about 0.4 monolayers, some areas of $c(2 \times 2)$ reach a critically large size and convert to $p(5 \times 5)$ domains. As shown in Fig. 10, we postulate that the binding energy per oxygen atom in a $p(5 \times 5)$ island or domain is a strong function of the size of that domain. This idea is taken from nucleation theory (30). Small islands or domains of $p(5 \times 5)$ are less stable than large islands because the increase in free energy due to interfacial tension at the island perimeter outweighs the decrease in free energy achieved by the change of phase within the body of the $p(5 \times 5)$ island. Thus, nuclei or islands smaller than a critical size are not viable (30). We expect that the interfacial tension is largely due to the discontinuity in metal surface structure at the island's edge, so the interfacial tension for a $p(5 \times 5)$ island is much larger than for a $c(2 \times 2)$ domain of comparable size. In other words, small areas of high oxygen density adopt the $c(2 \times 2)$ structure rather than the $p(5 \times 5)$. Large areas of high oxygen density adopt the $p(5 \times 5)$ structure rather than the $c(2 \times 2)$ structure. The $c(2 \times 2)$ is a necessary intermediate between the $p(2 \times 2)$ and $p(5 \times 5)$ structures. This model requires that the differential heat of adsorption of oxygen

in a large p(5x5) island is more negative than in the c(2x2) structure, in spite of the (assumed) higher packing density of oxygen in the p(5x5). The metal reconstruction must provide a stronger metal-oxygen bond, which outweighs oxygen-oxygen repulsions. A similar model is proposed for oxidation of Ni(100) (1).

Figure 11 illustrates the sequence of events which we postulate during adsorption at 400 K. As θ increases past 0.25 monolayers, regions of c(2x2) must form (Fig. 11A). These regions increase in area as coverage increases (Fig. 11B). At some point, the local areas encompassed by c(2x2) grow so large that conversion to p(5x5) occurs (Fig. 11C). The oxygen density within the new p(5x5) area is 28% higher than in the c(2x2). Therefore, this conversion leaves excess metal surface area available. Perhaps the excess area, shown in white in Fig. 11C, remains clean long enough to allow adsorption from the gas phase at the perimeter of the p(5x5) area. The sticking coefficient of oxygen into such regions would be high. This could account for the increase in oxygen sticking coefficient which accompanies appearance of the p(5x5) (cf. Fig. 2A and 4). This is qualitatively similar to the increase in oxygen sticking coefficient which accompanies the onset of oxidation on Ni(100) (1,31), and which may also accompany the onset of (1x3) reconstruction on Pt(100) (2).

The model of Figs. 10 and 11 also explains aspects of the data obtained by heating the sample at constant oxygen coverage in vacuum. Starting with the initial coverages of Figs. 8D-E, for instance, there is a mixture of p(2x2), c(2x2) and p(5x5) structures at 400 K. The



Key:

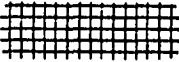
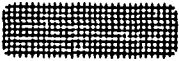

	p(2x2)
	c(2x2)
	p(5x5)

Figure 11. Schematic representation of the proposed adsorption sequence at $T = 400$ K.

reconstruction sets up a high energetic barrier against oxygen diffusion out of the $p(5 \times 5)$ regions, due to the difference in the heats of adsorption on the reconstructed and unreconstructed metal. As temperature is raised, however, the barrier can be surmounted and oxygen diffusion begins. As it does so, the local coverage within $p(5 \times 5)$ islands drops below that necessary to maintain the reconstructed phase, and the substrate reverts to (1×1) . In effect, diffusion forces the oxygen atoms to be more evenly distributed over the surface, but the best way it can accommodate that distribution is to form $c(2 \times 2)$. This explains why the $p(2 \times 2)$ and $p(5 \times 5)$ patterns disappear reversibly and in parallel, for instance, at 540 K in Fig. 8D, while the $c(2 \times 2)$ pattern intensifies simultaneously. Figure 8F ($\theta = 0.50$) suggests that there is also a region where $p(5 \times 5)$ and $c(2 \times 2)$ coexist, after the $p(2 \times 2)$ vanishes at about 500 K.

The interaction between these three structures and the $(\sqrt{5} \times \sqrt{5})R27^\circ$ reconstruction is less clear, particularly since we do not observe the latter phase during adsorption. Further discussion of this phase is deferred until the following section.

Because we postulate that nucleation is important in $p(5 \times 5)$ formation, it is reasonable that there may be some variation in results from system to system or experiment to experiment. The rate and mechanism of $p(5 \times 5)$ nucleation should naturally depend upon parameters such as oxygen pressure, sample temperature, density of surface defects, and method of preparation of the oxygen overlayer (e.g., annealing in vacuum from low temperature vs. adsorption at high temperature). This

may explain for instance, why the γ state is observed by Stuve et al. (8) following adsorption at unknown pressure and at 300 to 350 K (8,25), slightly lower in temperature than our minimum for activated p(5x5) formation, 400 K. Such variability may also account for the fact that the minimum coverage required to form p(5x5) in our experiments is lower during annealing in vacuum, where $\theta_{\min} \sim 0.30$ (cf. Fig. 8C), than during adsorption at elevated temperature, where $\theta_{\min} \sim 0.40$ (cf. Fig. 4). Some variation is similarly observed in the conditions necessary to oxidize Ni(100), which proceeds also by a nucleation and growth process (1,31).

It is puzzling that the LEED data show the surface to be completely covered by p(5x5) already at $\theta = 0.56$ and $T = 400$ K, as in Fig. 8G, since this is lower than the p(5x5)'s ideal coverage (0.64) and one would expect that a small fraction of the surface remains covered with c(2x2). One possible explanation is that the p(5x5) reconstruction, taking place in a nucleation and growth mechanism, leaves a great deal of disrupted metal surface at boundaries between p(5x5) domains. Oxygen adsorbed at these disrupted areas may not be observable with LEED. Another possibility is that our coverage calibration is in error, and the true coverage is close to 0.64. As stated earlier, the main potential source of error here is our assumption that a constant amount of oxygen dissolves into the Pd bulk, regardless of initial oxygen coverage.

In summary, the α state represents desorption from an adlayer with little or no long-range order. The β feature is associated with

desorption from $c(2 \times 2)$ order, in which n.n.n. repulsions cause a reduction in the binding energy. The γ state accompanies decomposition of the $(\sqrt{5} \times \sqrt{5})R27^\circ$ structure.

B. Desorption States

The three desorption states observed are directly correlated to the type of long-range order or disorder present in the adsorbed layer during desorption. Below 0.10 monolayers there is no desorption; only bulk dissolution occurs, between 300 and 400 K (Fig. 7). In the coverage regime $0.10 < \theta < 0.30$ there is a single desorption state, α (Figs. 8A-B). In this regime also, the $p(2 \times 2)$ or $p(2 \times 2) + c(2 \times 2)$ mixture disorders before desorption begins. Therefore, desorption throughout the α state takes place from an adlayer with little or no long-range order.

Between 0.30 and 0.50 monolayers, the β shoulder appears in TDS (Figs. 8C-F). In this coverage regime also, an ordered $c(2 \times 2)$ or $p(2 \times 2) + c(2 \times 2)$ mixture is present while desorption from the β state takes place. Repulsive interactions present in the $c(2 \times 2)$ apparently cause a lowering of the adsorption energy, so that atoms recombine and desorb from the $c(2 \times 2)$ lattice with a lower activation energy (at lower temperatures) than from the disordered layer. The difference in desorption energies in these two cases is large enough that two features appear in TDS, α and β . Our LEED observations, coupled with TDS data, are direct proof of this picture, which is in agreement with the earlier interpretation of Stuve et al. (8).

Finally, at coverages of 0.50 monolayers and above, the γ state emerges in TDS (Fig. 8G). Our LEED data indicate that this state is mainly due to recombination and desorption of oxygen from the $(\sqrt{5} \times \sqrt{5})R27^\circ$ structure while the metal substrate reverts to (1×1) . The phenomenon of desorption from a reconstructed metal surface which rearranges as coverage falls has been observed in other systems as well, notably O/Pt(100) (2), H/Ni(110) (12,13), H/Pd(110) (14), and H/W(100) (15). The low-temperature desorption feature in each of these cases is also very sharp and narrow, like the γ state on Pd(100). The mechanism and kinetics of desorption in this state are subject to continuing investigation in our laboratory.

The γ feature has been observed previously by Stuve et al. (8), who ascribe it to strong attractive interactions in the oxygen adlayer, although they cannot specify the nature of these interactions. Our combined use of LEED and TDS data allows us to firmly identify those interactions as the cooperative stabilization of the oxygen-induced metal reconstruction.

There are two related pathways by which reconstructions can form. The first is $p(5 \times 5)$ formation, which occurs at $T \gtrsim 400$ K and $\theta \gtrsim 0.40$. This is associated with an increase in oxygen sticking coefficient (Fig. 2A). The second process is reconstruction to the $(\sqrt{5} \times \sqrt{5})R27^\circ$ phase. This requires higher temperatures ($T \gtrsim 500$ K) and higher coverages ($\theta_0 \gtrsim 0.50$), and produces the γ state in thermal desorption. Furthermore, the $p(5 \times 5)$ phase may be a necessary prerequisite to the $(\sqrt{5} \times \sqrt{5})R27^\circ$ phase, under the conditions of our experiments, simply because the $(\sqrt{5} \times$

$\sqrt{5}R27^\circ$ is a high-coverage structure, and the $p(5 \times 5)$ is necessary during adsorption to build up enough oxygen on the surface.

C. Comparison with Other Metals

A pattern emerges upon comparison of oxygen reactions with Ni(100), Pd(100), and Pt(100) at high coverages. On Ni(100), at $\theta \gtrsim 0.35$, oxidation of Ni begins, and Ni atoms are displaced from their bulk-like positions (1,29). Oxygen is believed to penetrate the Ni lattice to a depth of 2-3 layers from the start (1). Palladium is less prone to oxidation than Ni, but nonetheless forms the $p(5 \times 5)$ phase at $\theta \gtrsim 0.4$ in which Pd atoms are (probably) displaced from the bulk-like positions. This is one of two oxygen-stabilized reconstructions which mimic the structure of bulk PdO, but in which the oxygen probably does not penetrate the metal lattice as deeply as in Ni. Even platinum, which does not form a stable oxide, exhibits two oxygen-stabilized reconstructions on the (100) surface (3). The oxygen-stabilized reconstructions on Pd(100) and Pt(100) (2) are directly linked to very narrow and sharp thermal desorption states. There is evidence that oxidation of Ni(100) (1,29), and oxygen-induced reconstruction of Pd(100) and Pt(100) (2,3), all occur via a nucleation and growth process. Thus, the reconstructions of Pt(100) and Pd(100), and the oxidation of Ni(100), appear to be analogous in many respects.

D. θ -T Diagram

We summarize our results in the θ -T diagram of Fig. 12, where the boundaries between regions are based on the inflection points of intensity-temperature data such as those in Fig. 8. We have not investigated the reversibility of transitions across all the boundaries shown; we have only confirmed (to date) that the vertical transition between regions 4 and 5 is truly reversible. Because of this, the portion of Fig. 12 which lies below the desorption onset should be regarded (at this point) as an empirical diagram which may incorporate some kinetic limitations, rather than a rigorous thermodynamic phase diagram. Nonetheless, we find that it is a useful representation of the conditions under which the various structures may form during adsorption of oxygen at fixed temperature or during annealing at fixed coverage.

Although we have not investigated the reversibility of oxygen disordering at $\theta \lesssim 0.30$, Auger indicates that some oxygen is lost by dissolution at about the same temperatures where oxygen disorders (cf. Fig. 7). Therefore, we expect that dissolution accompanies disordering and the order-disorder transition in this coverage regime is only partly reversible, similar to that investigated by Taylor and Park for O/Ni(100) (9).

It is interesting to speculate that region 4 may represent a portion of a thermodynamically allowed phase diagram. However, region 4 then violates the phase rule, according to which a three-phase region can only have one degree of freedom, i.e., the three-phase region of

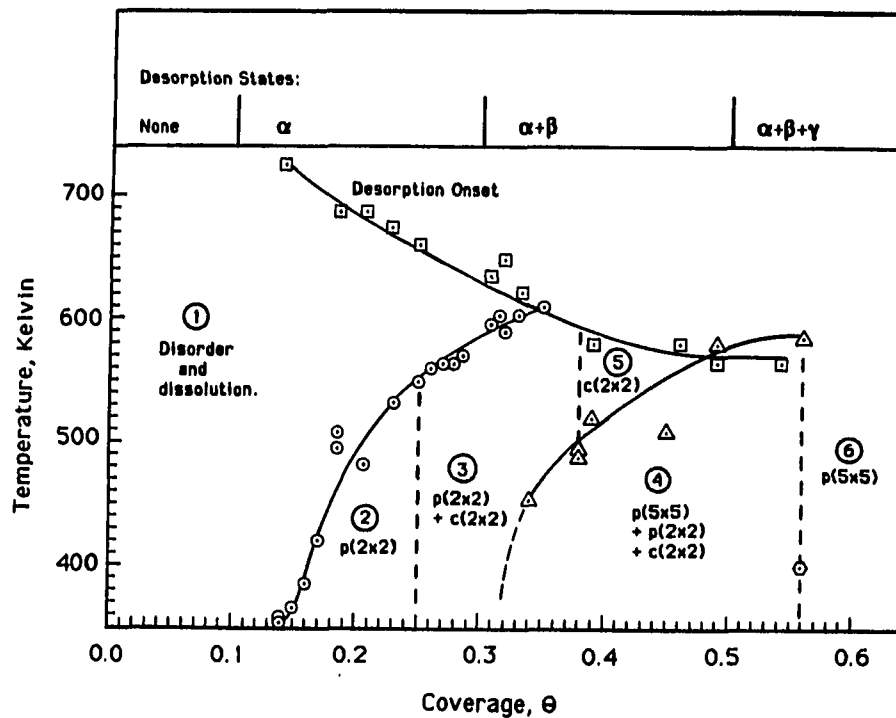


Figure 12. θ -T diagram for the system oxygen/Pd(100). The boundaries between regions are based upon data such as that shown in Fig. 8. Solid lines are used to connect data points; dashed lines are assumed or possible boundaries.

Fig. 12 should be only a line in θ -T space. One reasonable explanation may be that the p(2x2) and c(2x2) in areas 2, 3, and 4 of Fig. 12 are not distinct phases (32). Instead, there may be only a single (2x2) phase whose density varies continuously as coverage increases through these areas. This model is physically correct if the density increases at $\theta \gtrsim 0.25$ by random addition of atoms to n.n.n. sites, rather than by segregation into separate regions with long-range p(2x2) and c(2x2) order. Note that this model leads to a thermodynamically-allowed phase diagram, with no phase boundary separating regions 2 and 3. Note also that this implies that there are no third-n.n. attractions in the c(2x2), since third-n.n. attractions would favor c(2x2) island growth within the p(2x2) matrix, i.e., a true coexistence region. The "single (2x2) phase" model would contradict previous hypotheses about the nature of interactions in the c(2x2) (8,10).

V. SUMMARY

There is a complex relationship between order, reconstruction, and desorption in this system, which is summarized by the diagram of Fig. 12. The p(5x5) reconstruction forms from the unreconstructed c(2x2) in an activated step which begins at ca. 400 K. A mixture of low-density p(2x2) and high-density p(5x5), such as that in region 4, can reversibly transform to the intermediate-density c(2x2) phase (region 5) as temperature increases. This is because, at high temperature, diffusion out of the p(5x5) regions begins and the minimum coverage necessary to maintain the p(5x5) locally is lost. The p(5x5) areas dissolve, and c(2x2) must form to take up the extra coverage on the unreconstructed metal.

In thermal desorption, the α state shows the traits of second-order kinetics and is due to desorption from a disordered layer. The β state is due to desorption from a c(2x2) adlayer. There is a lower barrier to desorption in the β state than in the α state because of repulsive n.n.n. interactions in the c(2x2).

At $T > 500$ K and $\theta > 0.50$ the $(\sqrt{5} \times \sqrt{5})R27^\circ$ reconstruction forms. At slightly higher temperature, ca. 600-630 K, this phase reverts to the unreconstructed metal as oxygen desorbs in the γ state. We ascribe the sharp, narrow shape of the γ state to the cooperative stabilization of the reconstruction by adsorbed oxygen.

The reconstructions of Pd(100) appear analogous, in many respects, to the oxygen-stabilized reconstructions of Pt(100) (2,3) and the initial stages of oxidation of Ni(100) (1,29).

VI. ACKNOWLEDGMENTS

We gratefully acknowledge valuable communications with S. D. Bader, N. C. Bartelt, R. J. Behm, T. L. Einstein, J. W. Evans, R. B. Griffiths, E. M. Stuve, and E. D. Williams. J. W. Anderegg provided assistance with the apparatus. This work is supported by the Director for Energy Research, Office of Basic Energy Sciences. Ames Laboratory is operated for the U.S. Department of Energy by Iowa State University under Contract No. W-7405-ENG-82.

VII. REFERENCES

1. C. R. Brundle and J. Q. Broughton, "The Initial Interaction of Oxygen with Well-Defined Transition Metal Surfaces," in The Chemical Physics of Solid Surface and Heterogeneous Catalysis, Vol. 3, Ed. D. A. King and D. P. Woodruff, Elsevier, Amsterdam, in press.
2. P. R. Norton, K. Griffiths and P. E. Bindner, Surface Sci. 138 (1984) 125.
3. K. Griffiths, T. E. Jackman, J. A. Davies and P. R. Norton, Surface Sci. 138 (1984) 113.
4. G. N. Derry and P. N. Ross, Surface Sci. 140 (1984) 165; and references therein.
5. M. A. Barteau, E. I. Ko and R. J. Madix, Surface Sci. 102 (1981) 99.
6. G. Ertl and J. Koch, Z. Phys. Chem. 69 (1970) 323.
7. T. W. Orent and S. D. Bader, Surface Sci. 115 (1982) 323.
8. E. M. Stuve, R. J. Madix and C. R. Brundle, Surface Sci. 46 (1984) 155.
9. D. E. Taylor and R. L. Park, Surface Sci. 125 (1983) L73.
10. C. R. Brundle, R. J. Behm and J. A. Barker, J. Vac. Sci. Technol. A2 (1984) 1038.
11. D. D. Wagman, W. H. Evans, V. B. Parker, R. H. Schumm, I. Halow, S. M. Bailey, K. L. Churney and R. L. Nuttall, J. Phys. and Chem. Ref. Data 11 (1982) Suppl. 2.

12. K. Christmann, V. Penka, R. J. Behm, F. Chehab and G. Ertl, *Solid State Comm.* 51 (1984) 487; also
K. Christmann, F. Chehab, V. Penka and G. Ertl, *Surface Sci.* 152/153 (1985) 356.
13. P. R. Norton and P. E. Bindner, *Surface Sci.* 169 (1986) L259.
14. R. J. Behm, V. Penka, M.-G. Cattania, K. Christmann and G. Ertl, *J. Chem. Phys.* 78 (1983) 7486.
15. A. Horlacher Smith, R. A. Barker and P. J. Estrup, *Surface Sci.* 136 (1984) 327.
16. R. J. Behm, P. A. Thiel, P. R. Norton and G. Ertl, *J. Chem. Phys.* 78 (1983) 7437.
17. P. A. Thiel, R. J. Behm, P. R. Norton and G. Ertl, *J. Chem. Phys.* 78 (1983) 7448.
18. R. J. Behm, K. Christmann, G. Ertl, V. Penka and R. Schwankner, Ch. 40 of *The Structure of Surfaces*, Ed. by M. A. Van Hove and S. Y. Tong, Springer Verlag, Berlin (1985) pp. 257-263.
19. R. J. Behm, G. Ertl, and J. Winterlin, *Ber. Bunsenges. Phys. Chem.* 90 (1986) 294; also R. J. Behm, G. Ertl, V. Penka, and R. Schwankner, *J. Vac. Sci. Technol.* A3 (1985) 1595.
20. S.-L. Chang and P. A. Thiel, *Phys. Rev. Letters* 59 (1987) 296.
21. S.-L. Chang and P. A. Thiel, Chem. Dept., Iowa State Univ., in preparation.
22. P. A. Thiel and J. W. Andereg, *Rev. Sci. Instrum.* 55 (1984) 1669.
23. H. Herz, H. Conrad and J. Küppers, *J. Phys. E* 12 (1979) 369.

24. J. W. Anderegg and P. A. Thiel, *J. Vac. Sci. Technol.* A4 (1986) 1367.
25. E. M. Stuve, Chem. Engn., Univ. of Washington, private communication.
26. S. D. Bader, J. M. Blakeley, M. B. Brodsky, R. J. Friddle and R. L. Panosh, *Surface Sci.* 74 (1978) 405.
27. J.-S. Wang, *Proc. Royal Soc. London* A161 (1937) 127.
28. T. L. Einstein and J. R. Schrieffer, *Phys. Rev.* B7 (1973) 3629.
29. E. D. Williams, S. L. Cunningham and W. H. Weinberg, *J. Chem. Phys.* 68 (1978) 4688.
30. J. W. Christian, *The Theory of Transformations in Metals and Alloys*, Pergamon, Oxford (1975).
31. For example, see P. H. Holloway and J. B. Hudson, *Surface Sci.* 43 (1974) 123; also R. G. Smeenk, R. M. Tromp, J. W. M. Frenken and F. W. Saris, *Surface Sci.* 112 (1981) 261.
32. N. C. Bartelt, Dept. of Phys. and Astron., Univ. of Maryland, private communication; also R. B. Griffiths, Dept. of Phys., Carnegie-Mellon Univ., private communication.

PAPER IV:

OXYGEN-STABILIZED RECONSTRUCTIONS OF Pd(100):
PHASE TRANSITIONS DURING OXYGEN DESORPTION

**OXYGEN-STABILIZED RECONSTRUCTIONS OF Pd(100):
PHASE TRANSITIONS DURING OXYGEN DESORPTION**

S.-L. Chang, J. W. Evans and P. A. Thiel

**Department of Chemistry and Ames Laboratory-USDOE
Iowa State University
Ames, Iowa 50011 USA**

ABSTRACT

We present a detailed experimental study of desorption kinetics and accompanying structural phase transitions in a quasi-zero-order desorption state of atomic oxygen on Pd(100). The experimental data are of two types: measurements of desorption rates using thermal desorption spectroscopy, and measurements of changes in adlayer structure using Video-LEED. The data show directly that quasi-zero-order desorption occurs when the system passes through a two-phase region where one reconstructed phase of the adsorbate exists in equilibrium with an unreconstructed phase of the adsorbate. The experimental data are used to develop two microscopic models for the desorption phenomenon, which allow detailed analysis of the interplay between the reconstructed and unreconstructed phases during desorption. We argue that such coexistence regimes may be common in other systems where quasi-zero-order desorption kinetics are associated with phase transitions of the substrate, and may be generally responsible for these desorption states.

I. INTRODUCTION

Over the past several years, the scientific community has developed an increasingly strong interest in adsorbate-induced reconstructions of metal surfaces (1). In thermal desorption spectroscopy, a frequent characteristic of these reconstructions now appears to be desorption of the adsorbate in a state (or states) which is extremely sharp and narrow, which we shall describe as "quasi-zero-order". Desorption in such a state is invariably accompanied by drastic structural changes at the surface, e.g., loss of the reconstruction. This description holds true for the following systems, to date: H/Ni(110) (2-4), H/Pd(110) (5, 6), H/W(100) (7), H/Mo(100) (8), and O/Pt(100) (9-12). The kinetics of desorption in the sharp states have been identified in various cases as zero-order in adsorbate coverage (3), fractional-order in coverage (5), and "explosive" or "autocatalytic", i.e., effectively less than zero-order in coverage (12). In each case, the identification of a certain type of kinetics has led to the proposal of a mechanistic or thermodynamic model, independent of models proposed for the other systems. However, we suggest that the generality of these phenomena points to a common underlying mechanism.

In this paper, we report a detailed experimental study of desorption kinetics and accompanying structural phase transitions in a similar desorption state of atomic oxygen on Pd(100). The experimental data are mainly of two types: measurements of desorption rates using thermal desorption spectroscopy, and measurements of changes in adlayer

structure using Video-LEED. The data show that the desorption kinetics are primarily associated with a region of the phase diagram where a reconstructed phase coexists with an unreconstructed phase. We argue that coexistence regimes may be common in similar systems, such as those cited above, and that the interplay between the reconstructed and unreconstructed phases may provide a general explanation for quasi-zero-order desorption states in these systems. The data are also used to develop two detailed, microscopic models for the desorption phenomenon.

Oxygen induces four ordered surface structures on Pd(100) (13-15). Two are believed to represent chemisorbed oxygen on an unreconstructed substrate. These are the $p(2 \times 2)$ and $(\sqrt{2} \times \sqrt{2})R45^\circ$ lattices [the latter is commonly called $c(2 \times 2)$], with ideal coverages (θ) of 0.25 and 0.50 monolayers, respectively (13,14). The two oxygen-induced reconstructions exhibit $p(5 \times 5)$ and $(\sqrt{5} \times \sqrt{5})R27^\circ$ periodicity, with probable ideal coverages of 0.64 and 0.80 monolayers, respectively (14). The $(\sqrt{5} \times \sqrt{5})R27^\circ$ structure is denoted simply $\sqrt{5}$ in this paper, for brevity's sake. The real and reciprocal-space lattices representations associated with the four ordered phases can be found in reference 16.

Note that there is no structural determination available for either reconstruction, but the structures shown in Ref. 16 Fig. 1 are reasonable possibilities (14). Orent and Bader (14) report that oxygen in the reconstructions is very efficiently titrated with gaseous CO, a result which we have reproduced in our own laboratory. The Auger

coverage determinations of Orent and Bader (14), combined with the known density of oxygen atoms in the low-index planes of PdO, imply that there is only one layer of oxygen in the reconstructions. This suggests that oxygen is at the surface and thus readily available for reaction, rather than buried below the Pd atoms. A rapid equilibrium between surface and subsurface oxygen populations would have the same effect, but then the oxygen should be more than one layer deep. One must conclude that there is no firm evidence presently available concerning the position of the oxygen atoms with respect to the surface Pd layer, although there are indirect indications that the oxygen is only one layer deep and is located at the surface.

Thermal desorption spectra were first measured for O/Pd(100) by Stuve et al. (15). The spectra exhibit three features, each of which can be related to the surface structure which is present during desorption (16). Most important to this work is the so-called γ state, which we have previously associated with the processes of $p(5 \times 5) \rightarrow \sqrt{5}$ conversion, and subsequent decomposition of the $\sqrt{5}$ structure (16). The present contribution is an exhaustive study of the γ state desorption kinetics and their relationship to the underlying structural changes in the adlayer.

II. EXPERIMENTAL METHODS

The experiments are all performed in a stainless-steel, ultrahigh vacuum system which is equipped for Auger electron spectroscopy (AES), ion bombardment, mass spectrometry, Video low-energy electron diffraction (LEED) (17), sample heating and cooling (18,19), and gas handling.

In many of the experiments, the LEED pattern characteristics are measured at constant temperature during oxygen desorption from the surface (isothermal desorption). Figure 1 shows the typical variation of temperature with time during such an experiment. At the start of the experiment, the sample is heated with a linear heating rate, β , of 0.9 K/s (unless specified otherwise) to some predetermined temperature, such as 574 K in Fig. 1. At that point the ramp is stopped and temperature remains constant for some period of time, until finally the ramp is started again to complete desorption. In the LEED experiments, the sample is rapidly and alternately heated and cooled throughout this process; LEED data are acquired during each brief cooling cycle. For this reason, temperature drops during each measurement period, typically by 12 K (2%) or less. The resultant oscillations in temperature can be seen in the data of Fig. 1. (These oscillations are not present during measurements of desorption rates.) Each temperature quoted here for an isothermal-LEED experiment is the average temperature maintained throughout the isothermal period.

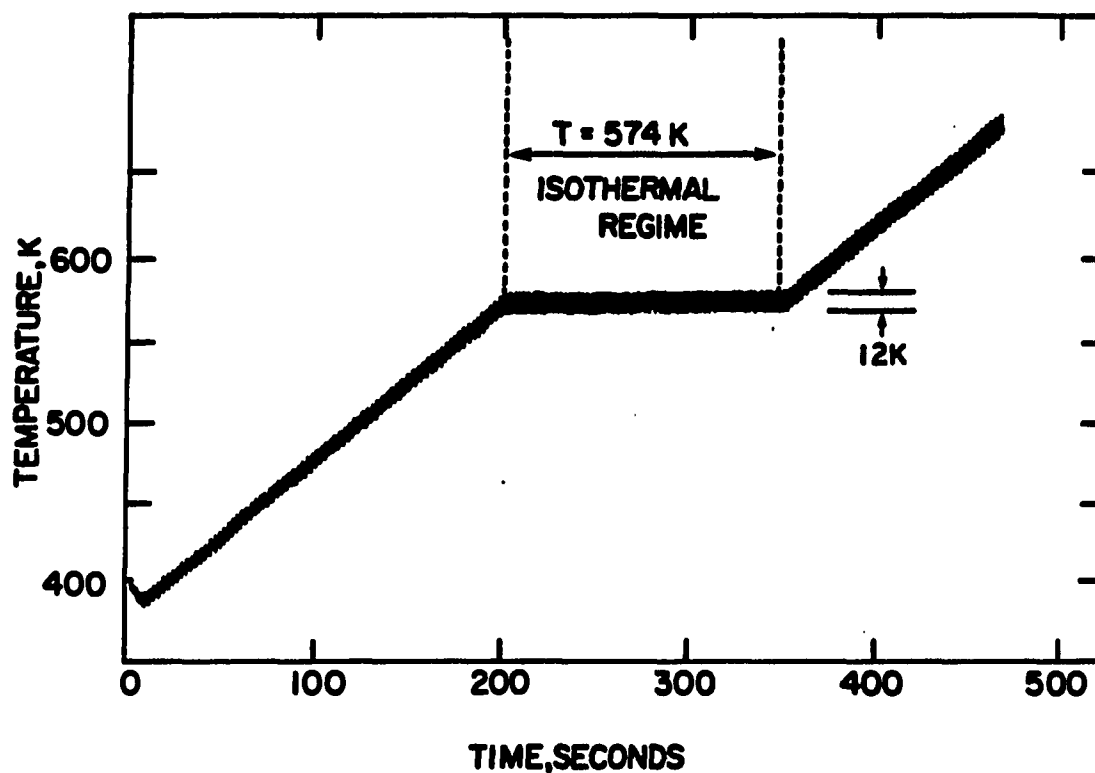


Figure 1. Time-dependent variation in temperature during a typical "isothermal" experiment. Note that temperature increases linearly with time, both before and after the true isothermal period, where $T = 574$ K. The rapid oscillations of ± 6 K about the average temperature are only present during LEED measurements, and are due to alternation of heating periods with cooling-measurement periods.

We find that the shapes of the thermal desorption spectra, particularly the relative intensity and sharpness of the γ state for a given exposure, are extremely sensitive to sample cleanliness (i.e., traces of residual oxide) and to gas purity. In order to obtain reproducible data, it is necessary to examine the Pd surface with AES regularly, and also to change the oxygen in the gas handling manifold often. Coverages given in this paper are based upon a calibration described elsewhere (16). We estimate an accuracy of ± 0.05 monolayers, although this uncertainty is larger if the amount of bulk dissolution is grossly dependent upon initial coverage (16).

Other details relevant to these experiments are described fully elsewhere (16).

III. EXPERIMENTAL RESULTS

In Figure 2, we show typical thermal desorption spectra at constant initial coverage and at four different heating rates. It is immediately obvious that the leading edges of the γ state overlap very well at all heating rates. We find this to be true at all coverages between 0.51 monolayers (just past the coverage where the γ state first appears) and 0.57 monolayers. Since the leading edges of a zero-order desorption feature must be identical at all heating rates, this is an initial indication that the desorption kinetics of the γ state may be zero-order in coverage, or nearly so. Further, the leading edges of the γ state overlap very well when the initial coverage is varied at constant heating rate (16). This is another classic characteristic of zero-order kinetics. The variation of $\ln P_{O_2}$ with T^{-1} also satisfies the requirement for zero-order desorption, exhibiting a reasonably good linear dependence throughout the leading edge of the γ state. This is shown by Fig. 3, where eight different experimental results are represented. The average slope of the straight lines corresponds to an activation barrier of 208 ± 16 kJ/mol.

Note that the shapes of the desorption spectra shown in Fig. 2 are insensitive to variations in heating rate between 0.9 and 8.4 K/s, indicating that nonequilibrium surface effects do not have a significant effect on the desorption kinetics, within this range of heating rate (20).

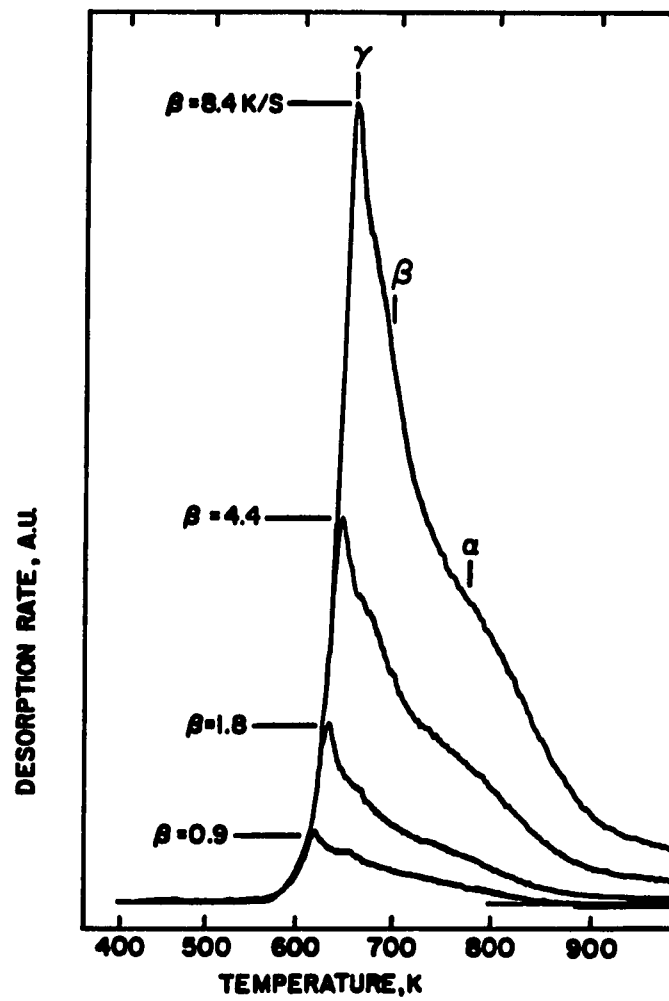


Figure 2. Thermal desorption spectra at constant initial coverage (0.57 monolayers) and at a variety of heating rates (β) as indicated.

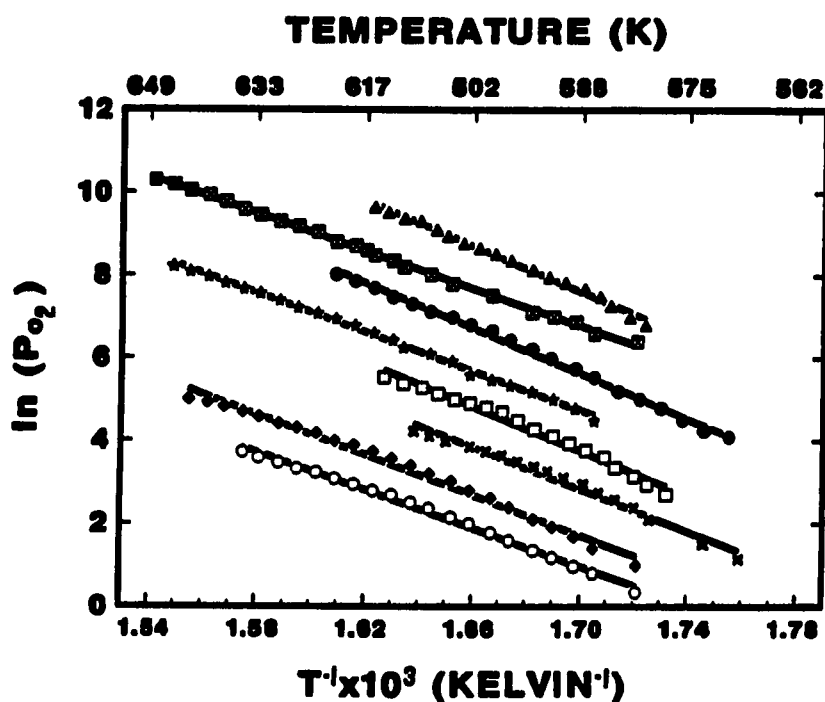


Figure 3. Variation of $\ln P_{O_2}$ with T^{-1} in the leading edge of the γ desorption state. Different symbols show results from different experiments. The average slope corresponds to an activation barrier of 208 ± 16 kJ/mol. (16 kJ/mol = 1 standard deviation.) From bottom to top, the curves represent initial coverages of 0.51, 0.53, 0.53, 0.55, 0.57, 0.59, 0.60, and 0.60 monolayers, respectively. The curves are displaced vertically by arbitrary amounts for clarity.

Measurements of the oxygen desorption rate under isothermal conditions are shown in Fig. 4. These data are representative of coverages between 0.53 and 0.60 monolayers. In spectra (a) through (d), heating programs similar to Fig. 1 are applied; the constant-temperature regimes fall between each left-hand label and the arrow at 430 s. Spectrum (e) shows the result when there is no isothermal regime, i.e., the linear heating rate of 0.9 K/s is uninterrupted. Note that for desorption kinetics which are zero-order in coverage, the desorption rate must be constant throughout the isothermal regime. Three conclusions can then be drawn from the data of Fig. 4. First, in spectra (a) through (d), desorption rate is not constant throughout the isothermal regime; clearly, desorption rate is a function of coverage within the γ state. However, the spectra seem to approach "zero-order" behavior in the limit of short times and low temperatures. For example, spectrum (a) is more nearly horizontal in the isothermal regime than is spectrum (b); furthermore, spectrum (a) is more horizontal at the beginning of the isothermal regime than at the end.

Second, there are often two clearly discernible stages of desorption in the isothermal regime; this is shown particularly well by spectrum (b) of Fig. 4. There, the desorption rate decreases linearly with time between 210 and 270 seconds, then begins to decline more abruptly at 270 s. Third, subsequent desorption is influenced by the conditions during the isothermal regime. In spectrum (a), for instance, the amount of oxygen desorbing in the β state (centered at 500-510 s in Fig. 4) is larger than in spectrum (d). In other words, isothermal

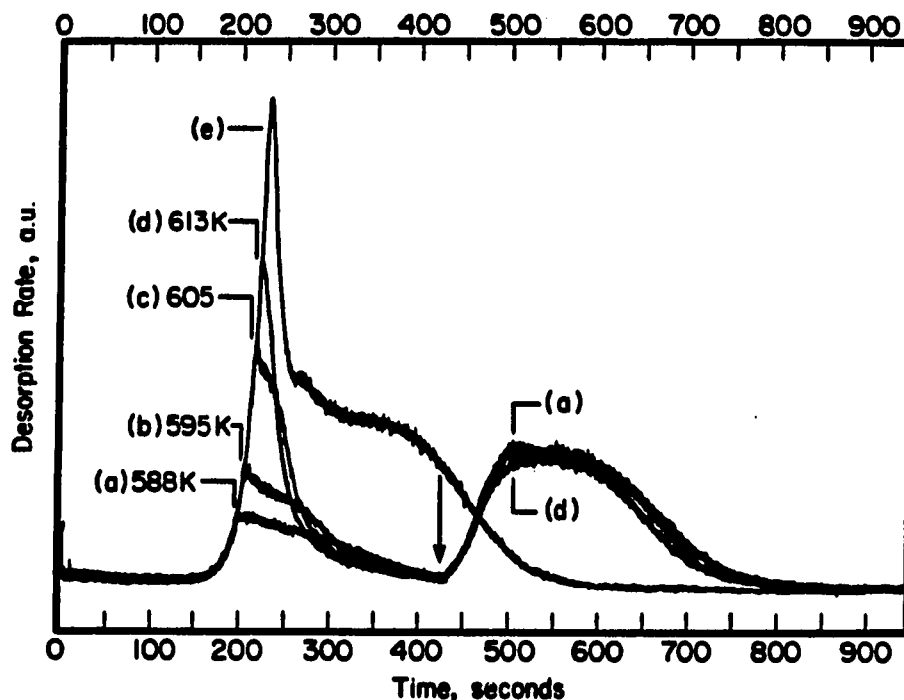


Figure 4. Thermal desorption spectra, at constant initial coverage (0.55 monolayers) and constant heating rate (0.9 K/s). In experiments (a) through (d), heating programs similar to Fig. 1 are used. Each isothermal regime begins at the vertical bar of the left-hand label, and remains at the temperature indicated until the arrow (430 seconds after the start of the experiment). Spectrum (e) shows the result when there is no isothermal regime, i.e., the linear heating rate is uninterrupted.

desorption at higher temperatures leads to significant depopulation of the β state. Because we have previously identified the β state with oxygen in the $c(2 \times 2)$ structure, this indicates that the $c(2 \times 2)$ structure is depleted during isothermal desorption at high temperatures, on these time scales.

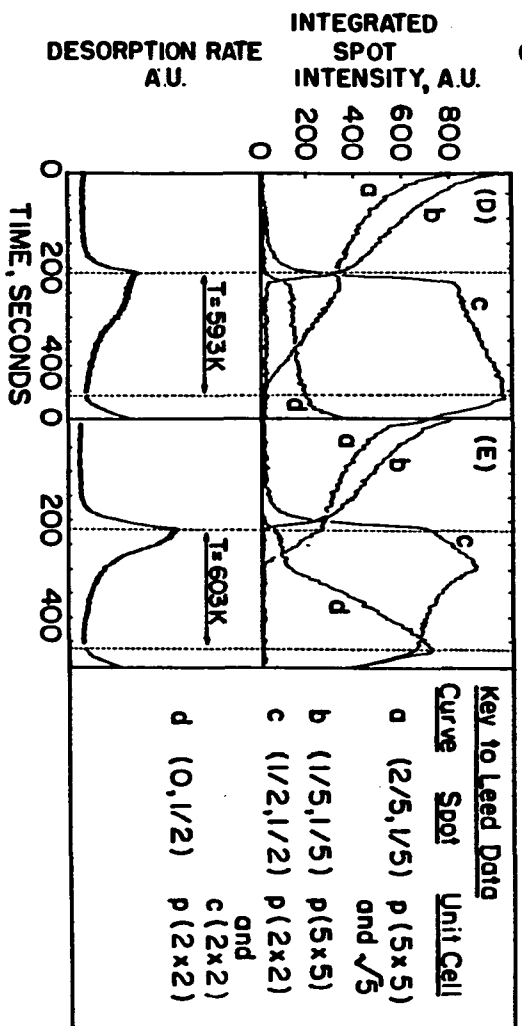
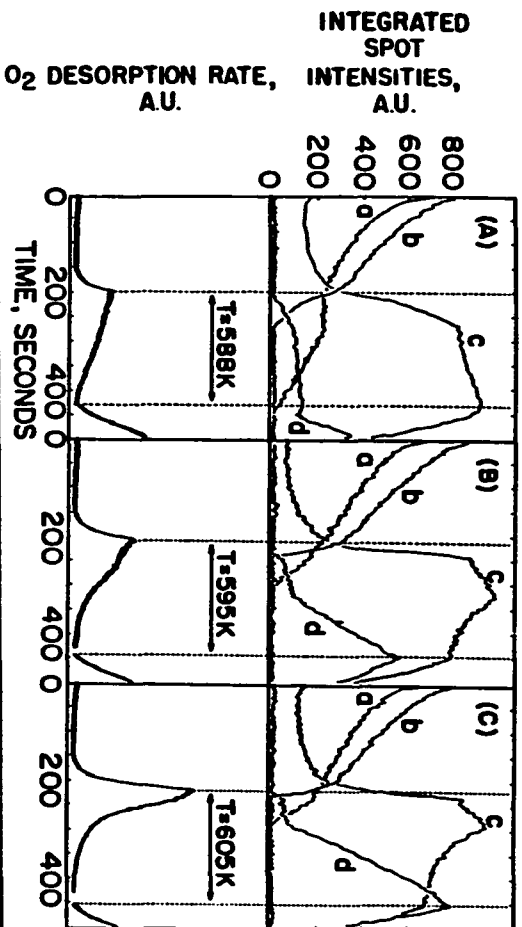
Figures 5A-C show LEED data which are taken under conditions identical, or nearly so, to three of the measurements of Fig. 4. The initial coverage is 0.55 monolayers. Figures 5D-E show the same types of measurements at a higher initial coverage, 0.60 monolayers. LEED data are shown in the top panels, and desorption rate measurements are reproduced in the bottom panels for comparison. The LEED data consistently exhibit four stages of change, before and during isothermal desorption:

(i) Intensities of all LEED spots decrease in parallel as the sample is heated, presumably due to Debye-Waller attenuation.

Desorption does not take place.

(ii) Desorption begins at an appreciable rate. The $(1/5, 2/5)$ spot intensity (curve a) remains constant or decreases slightly; the $(1/5, 1/5)$ spot intensity (curve b) decreases precipitously; the $(1/2, 1/2)$ spot intensity (curve c) increases strongly; and the $(0, 1/2)$ spot intensity (curve d) weakly mimics the $(1/2, 1/2)$ spot. The relative intensities of the latter two features is such that they must represent mainly $c(2 \times 2)$, with only a small amount of the $p(2 \times 2)$ structure (16). In this stage, the data can only mean that the $p(5 \times 5)$ disappears, while the $\sqrt{5}$, $c(2 \times 2)$, and $p(2 \times 2)$ structures simultaneously grow. Desorption

Figure 5. Isothermal LEED and TDS experiments. The initial coverage is 0.55 monolayers in A-C, and 0.60 monolayers in D-E. In each experiment, a heating program similar to Fig. 1 is used, with $\beta = 0.9$ K/s. The top panel of each experiment illustrates the variation in the following integrated LEED spot intensities: a = (2/5, 1/5); b = (1/5, 1/5); c = (1/2, 1/2); and d = (0, 1/2). Each lower panel shows the desorption rate as a function of time under conditions identical, or nearly so, to those in the top panel.



in the γ state begins as the $p(5 \times 5)$ structure disappears.

(iii) The complete disappearance of the $p(5 \times 5)$ marks an abrupt change in the rates of growth or disappearance of the other three structures, and the second stage of desorption begins. During this stage, the $(2/5, 1/5)$ spot (curve a) decreases to zero intensity, while the remaining two features,--the $(1/2, 1/2)$ spot (curve c) and the $(0, 1/2)$ spot (curve d)--both increase more slowly, while maintaining a constant ratio of intensities. These data show that the $\sqrt{5}$ structure begins to disappear just when the $p(5 \times 5)$ structure vanishes completely; as the $\sqrt{5}$ disappears, the $c(2 \times 2)$ and $p(2 \times 2)$ structures continue to grow, albeit more slowly than in stage (ii). Desorption in the γ state continues throughout. Interestingly, we sometimes observe visually that one domain of the $\sqrt{5}$ structure disappears before the other at the end of stage (iii). Perhaps this occurs because crystal misorientation ($\pm 0.5^\circ$) acts to stabilize one domain slightly relative to the other.

(iv) The disappearance of the $\sqrt{5}$ marks another abrupt change in the rate of growth of the remaining two structures. The $(1/2, 1/2)$ spot intensity (curve c) now decreases, and the $(0, 1/2)$ spot intensity (curve d) increases. This can only mean that the $c(2 \times 2)$ diminishes while the $p(2 \times 2)$ grows during this last stage of isothermal desorption. Data presented elsewhere (16) show that the beginning of this stage coincides with the maximum of the γ -state when the heating rate is held constant.

Note that stage (iv), where the $c(2 \times 2)$ intensity decreases, is only observed (on our time scales) during isothermal desorption at high

temperatures, such as 605 K in Fig. 5; stage (iv) does not occur at the lower temperature of 588 K. This is consistent with the data of Fig. 4, which also indicate that the $c(2 \times 2)$ can be depleted by isothermal desorption at high temperatures, on these time scales. We believe that the reason stage (iv) is not reached at low temperatures is simply because we do not allow enough time for the reconstructions to be entirely depleted at these temperatures.

The LEED observations are summarized in Table 1.

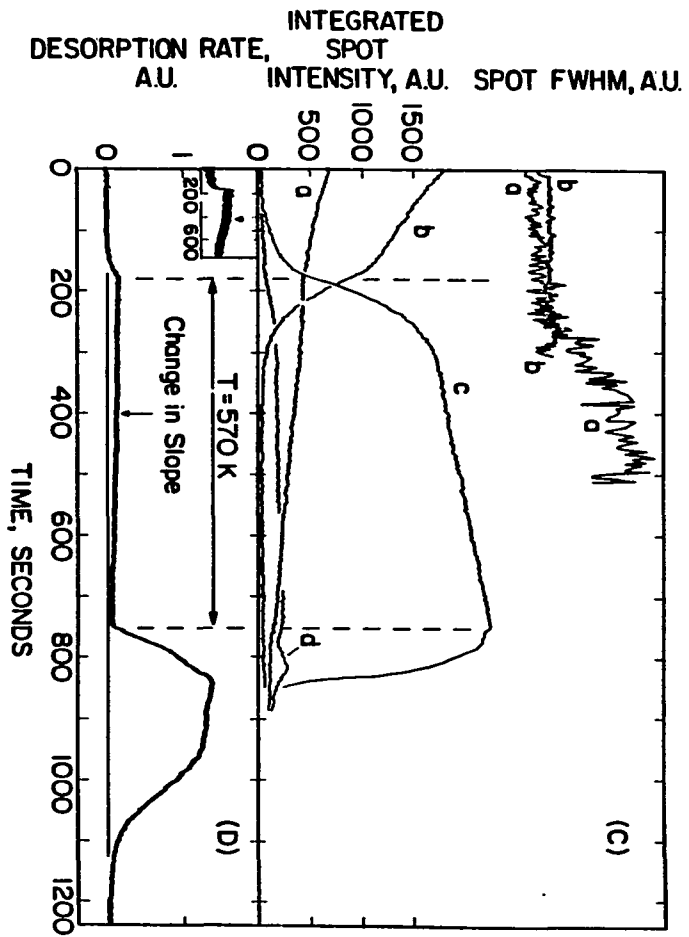
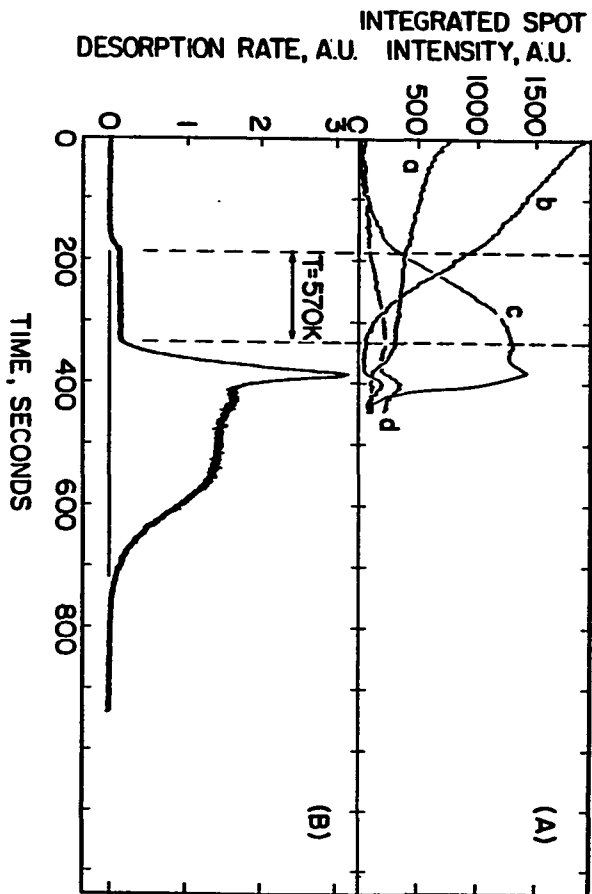
Perhaps most enlightening, however, are the experiments of Fig. 6. This figure shows isothermal measurements of LEED spot intensities (panels A and C) and desorption rates (panels B and D) at a relatively low temperature, 570 K, for two different lengths of time. The low temperature allows the experiments to proceed very slowly, so that the separate regimes can clearly be separated. Note that the absolute intensities shown by curves (a) and (b) in the LEED data are not directly comparable to Fig. 5, because different (although equivalent) beams are chosen for intensity measurements, and the sample appears to be turned 2° or 3° away from normal incidence. This only affects the absolute values and not the general trends in the data, however.

Panels (A) and (B) show the results when temperature is maintained constant only through stage (ii), i.e., only up to the point where the $p(5 \times 5)$ disappears completely. This occurs at 330 seconds. Two things should be noted from these data. First, at this very low temperature, the desorption rate appears to be genuinely zero-order throughout the isothermal regime of Fig. 6, panel (B). In other words, at low

Table 1. Description of the four stages of desorption observed in LEED and desorption rate measurements.

Stage	LEED observations	Isothermal desorption rate as a function of time	Region of θ -T diagram (see Fig. 9)
i	Intensities of p(5x5) and c(2x2) (if present) decrease gradually due to Debye-Waller effects	No desorption	p(5x5) alone or p(5x5) + (2x2) coexistence
ii	p(5x5) is disappearing $\sqrt{5}$ grows c(2x2) and p(2x2) grow rapidly and in parallel	Constant, or slightly decreasing	p(5x5) conversion to $\sqrt{5}$ and (2x2) is kinetically limited (non-equilibrium region). All three structures are present.
iii	$\sqrt{5}$ is disappearing c(2x2) and p(2x2) grow slowly and in parallel	Decreasing more rapidly	$\sqrt{5}$ and (2x2) coexistence
iv	c(2x2) diminishes p(2x2) grows	Decreasing still more rapidly; desorption occurs from β state.	(2x2) only

Figure 6. Isothermal desorption experiments at $T = 570$ K. In panels (A) and (B), the isothermal period lasts 150 seconds. In panels (C) and (D), it lasts 420 seconds. Panels (A) and (C) show the LEED data, curves labelled as in Fig. 5, whereas panels (B) and (D) show the corresponding desorption rates. The inset to panel (D) shows the desorption rate magnified by a factor of two over a compressed time-scale. In each case, the heating program is similar to Fig. 1, with $\beta = 0.9$ K/s, and the initial coverage is 0.55 monolayers.



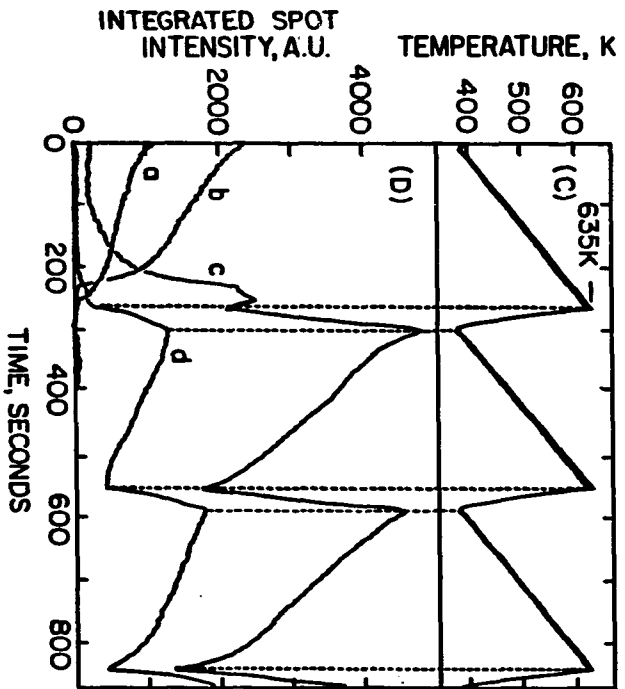
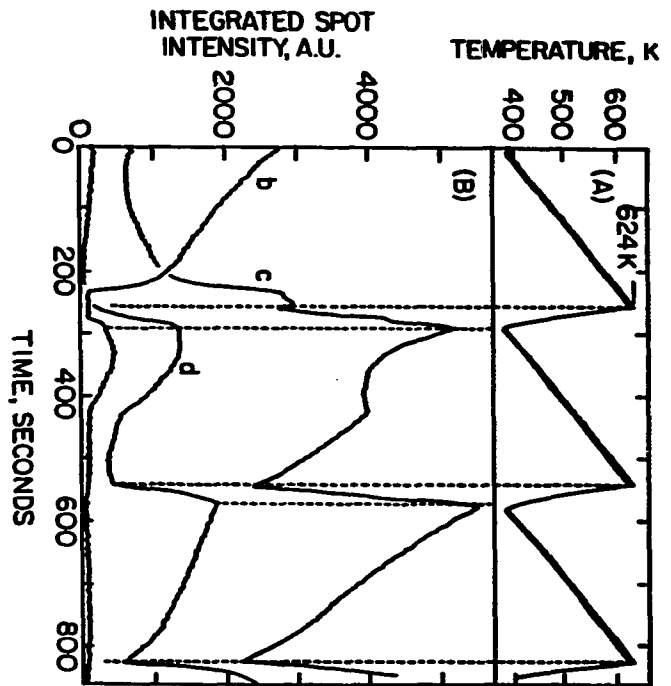
temperature, decomposition of the $p(5 \times 5)$ reconstruction is accompanied by zero-order, or very nearly zero-order, desorption kinetics. Second, when the temperature ramp is started again at the end of the isothermal period, the first desorption feature looks very similar to the original γ state. This shows that the γ state is still substantially populated at the end of stage (ii).

Panels (C) and (D) of Fig. 6 show the results when temperature is maintained constant throughout stages (ii) and (iii). Thus, the isothermal regime extends to the point where the $\sqrt{5}$ structure (almost) vanishes, i.e., to 750 seconds. When the temperature ramp is resumed after 750 seconds, the data show that the γ state has been mostly removed. (A small vestige remains visible on the leading edge, between 750 and 800 s, presumably because the $\sqrt{5}$ structure is not quite removed in the isothermal period.) In other words, the γ state is depopulated by desorption during stages (ii) and (iii). In panel (D), and particularly in the inset, the desorption rate shows a very slight change in slope, at constant temperature, at about 400 seconds. A much more pronounced change in slope is observed in those experiments where the reconstructions are entirely depleted during the isothermal regime, as in Fig. 5B, C, D, or E.

Panel (C) of Fig. 6 also shows data regarding the LEED spot widths of the reconstructed phases, taken from line profiles. The results shown are quite similar to those for all other isothermal experiments. The $(1/5, 1/5)$ spot is constantly sharp until its disappearance, at 300 s in Fig. 6C. These data indicate that the regions of $p(5 \times 5)$ structure are large, probably larger than the instrumental response, whenever this structure is present during isothermal desorption. In contrast, the $(2/5, 1/5)$ spot broadens slightly as the $(1/5, 1/5)$ spot disappears at the end of stage (ii), and it continues to broaden as it fades during stage (iii). Thus the $\sqrt{5}$ islands are smaller than the parent $p(5 \times 5)$ regions, and continuously decrease in size as they disappear during stage (iii).

Finally, we note that when desorption is stopped in stage (iii), or even early in stage (iv), and the sample is re-cooled, the $p(5 \times 5)$ pattern reappears. Although this statement must rest partly on our simple visual observations, part of its justification is shown in Fig. 7. This figure shows results from experiments in which the sample is repeatedly cycled into and out of the desorption regime. When the maximum temperature is 624 K, as shown in panels (A) and (B), desorption of the γ state stops in stage (iv), and the $p(5 \times 5)$ pattern reappears upon cooling. This is shown by the behavior of curve b in panel (B),

Figure 7. Repetitive heating-cooling cycles, following adsorption of 0.55 monolayers oxygen at 400 K. Panels (B) and (D) show the LEED spot intensities vs. time, and panels (A) and (C) show the corresponding temperature programs. In each case, the sample is heated from 400 K to some temperature above the point where desorption becomes measurably fast (ca. 570 K), then cooled back to 400 K; this cycle is repeated three times. In panels (A) and (B), the sample is heated to 624 K in each cycle. In (C) and (D), the sample is heated to 635 K in each cycle.



between 280 and 400s. When the maximum temperature is higher, 634 K, the sample is heated past the γ state, and panels (C) and (D) show that neither the $p(5 \times 5)$ nor $\sqrt{5}$ structures reappear upon cooling. Coverage falls throughout each heating cycle, and details of the intensity changes observed during each successive cycle are entirely consistent with coverage- and temperature-dependent data discussed elsewhere (16). The main point here, however, is that the $p(5 \times 5)$ to $\sqrt{5}$ transformation is reversible in temperature, so long as coverage does not fall too low as a result of desorption. In other words, the change between the $p(5 \times 5)$ and $\sqrt{5}$ structures is a true thermodynamic phase transition, occurring at ca. 570 K.

IV. INTERPRETATION OF EXPERIMENTAL RESULTS: ADLAYER STRUCTURE DURING DESORPTION

The most striking aspect of our data is the fact that all structural changes which occur during γ -state desorption are strongly and clearly linked. This is shown by the isothermal-LEED data of Figs. 5 and 6. This suggests that equilibrium is established between the various surface structures during γ -state desorption. We propose that Fig. 8 represents a portion of the θ -T diagram through which the system passes in the γ -state, based upon data presented in this paper and elsewhere (16,21). The interpretation of the larger θ -T diagram is the subject of another paper (21), but a few details are germane to the present discussion. First, the structures which we observe in LEED include the c(2x2) and p(2x2), but it is not clear whether these are separate thermodynamic phases, or a single phase of continuously variable density (16). We include both structures in the designation "(2x2)", used in Fig. 8 and the following section. In this terminology, (2x2) can be regarded as having continuously variable density, up to the maximum of 0.5 which is set by the c(2x2) structure. Second, in this paper we have shown that the transition between the p(5x5) and $\sqrt{5}$ reconstructions, in the presence of c(2x2), is reversible. Therefore, the (2x2) + $\sqrt{5}$ coexistence region shown in Fig. 8 must constitute a valid portion of the true thermodynamic phase diagram, with a lower bound at ca. 570 K. Finally, other data show that the vertical boundary between the coexistence region containing p(5x5) and (2x2) structures,

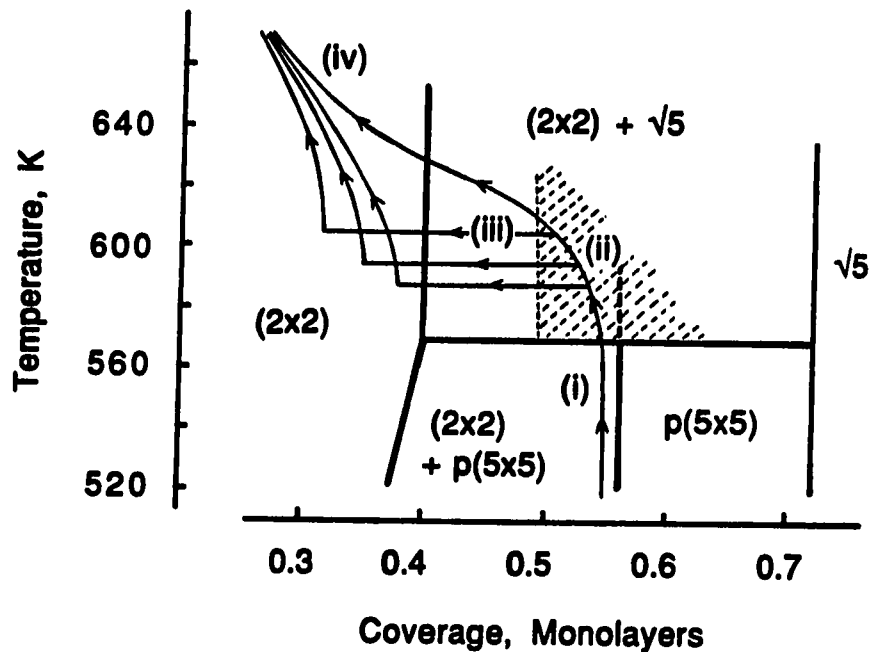


Figure 8. A portion of the θ - T diagram for the O/Pd(100) system. The lines with arrowheads represent desorption trajectories. Trajectories shown for constant heating rate (top curve) and for various isothermal programs (lower curves) are calculated from the direct desorption model described in the text. The regions through which the trajectories pass are labelled (i) - (iv), to correspond to the four experimental stages described in Table 1. The shaded region (ii) represents a portion of the trajectory where the system is not in equilibrium due to the presence of p(5x5).

and the $p(5 \times 5)$ region, occurs about 0.08 monolayers below the ideal coverage in the $p(5 \times 5)$ (16). For consistency--and in the absence of experimental evidence--we place the vertical border between $p(5 \times 5)$ and $\sqrt{5}$ regions also 0.08 monolayers below the ideal coverage of the $\sqrt{5}$, although this is (at best) an educated guess.

The solid lines with arrowheads in Fig. 8 represent desorption trajectories. The regions through which the trajectories pass are labelled (i)-(iv), corresponding to the four experimental stages described in Table 1. In stage (i), the (2×2) and reconstructed $p(5 \times 5)$ phases coexist, or the $p(5 \times 5)$ alone is present. No desorption occurs, and therefore this part of the trajectory is vertical.

In stage (ii), T increases above 570 K, the system crosses into the $\sqrt{5} + (2 \times 2)$ coexistence region of the θ - T diagram, and desorption begins. It is clear from the LEED data that the system is far from equilibrium in this stage, however. The $(1/5, 1/5)$ spot intensity is non-zero, demonstrating unambiguously that $p(5 \times 5)$ reconstruction is still present. This behavior is easily understood: conversion of $p(5 \times 5)$ to $\sqrt{5}$ and (2×2) cannot occur quickly enough to keep up with the increase of temperature above 570 K. In effect, the system is "upquenched." As the process evolves from the beginning to the end of stage (ii), i.e., from $p(5 \times 5) + (2 \times 2)$, to $\sqrt{5} + (2 \times 2)$ equilibrium, clearly the $p(5 \times 5)$ is replaced by $\sqrt{5}$. However, a significant amount of (2×2) phase is also necessarily created, because the system ends up much further from the right-hand side of the appropriate coexistence region. This behavior is evidenced by the rapid and substantial increase of the $(1/2, 1/2)$ spot

intensity which accompanies disappearance of the $(1/5, 1/5)$ spot, e.g., between 200 and 250 s in all of the data of Fig. 5. We envision that a certain fraction of $p(5 \times 5)$ regions are compressed into $\sqrt{5}$ regions with some extra (2×2) formed at the perimeter, as illustrated in Fig. 9. Correspondingly, the experimental data show that the $(2/5, 1/5)$ spot profile broadens during this process (Fig. 6C).

As coverage continues to fall, the system enters stage (iii). Here, no $p(5 \times 5)$ remains; only $\sqrt{5}$ and (2×2) coexist. We assume that the adlayer is equilibrated in this stage. Thus, as coverage falls, the system moves farther to the left of the coexistence region, and the amount of (2×2) increases as the amount of $\sqrt{5}$ falls. This is reflected in the increasing intensity of the $(1/2, 1/2)$ spot, and decreasing intensity of the $(2/5, 1/5)$ spot during stage (iii), for instance between 300 and 750 s in Fig. 6C.

Note that there is weak $p(2 \times 2)$ intensity in stages (ii) and (iii), in addition to the bright $c(2 \times 2)$, and that the $p(2 \times 2)$ intensity exactly tracks the $c(2 \times 2)$ intensity. This shows that the (2×2) phase maintains constant density during isothermal desorption, consistent with the idea that the system passes through a coexistence regime in stages (ii) and (iii). This density must be quite high (probably ~ 0.40 to 0.45), since the $p(2 \times 2)$ pattern is so weak.

Finally, the system crosses from stage (iii) into stage (iv). The $\sqrt{5}$ reconstruction disappears, and the system enters a (2×2) region of the phase diagram. The increasing intensity of the $p(2 \times 2)$ pattern, and

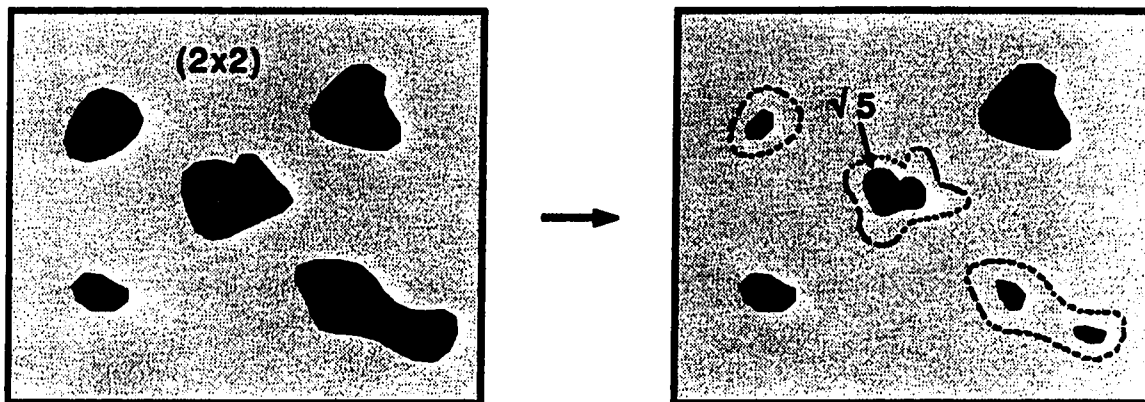


Figure 9. Schematic depiction of the process by which small regions of $p(5 \times 5)$ (labelled "5") within a sea of (2×2) may convert to $\sqrt{5}$ and additional (2×2) , as the system passes through region (ii) of Fig. 8 and Table 1.

decreasing intensity of $c(2 \times 2)$ in this stage show that the density of the (2×2) phase decreases throughout. See, for instance, the period between 290 and 450 s in Fig. 5C. Desorption in this stage corresponds to depopulation of the β desorption state, as shown by Figs. 4 and 5. As we have discussed elsewhere (16), the presence of the β desorption state reflects the influence of the next-nearest-neighbor (NNN) repulsions which also influence the $c(2 \times 2)$ ordering; thus, the behavior of the two is linked. The α and β desorption states both can be reasonably well fit by choosing a low coverage desorption barrier of $E_0 = 205$ kJ/mol, next-nearest-neighbor (NNN) repulsion of 5 kJ/mol, and a pseudo-second-order pre-exponential rate factor, ν_2 , of $2.31 \times 10^{-12} \text{ s}^{-1}$. (The ν_2 quantity is defined in Section V.) Note that these parameters are different than previously reported (16), but they fit the data better, and this E_0 agrees well with a value determined by Milun et al. (22). At high $\theta \sim 0.4$ monolayer, the effective desorption barrier decreases to ~ 170 kJ/mol. Recalling from Fig. 3 that the desorption barrier in the γ state is ~ 208 kJ/mol, this shows that oxygen in a high-density (2×2) structure is less strongly bound than in the γ state.

We believe that there is continuous desorption from the (2×2) structure from stage (ii) through (iv), i.e., throughout the γ state. The data of Fig. 4 and 5 show clearly that depletion of oxygen from the high-density (2×2) structure (β desorption state) takes place in stage (iv), at the end of the isothermal period. If desorption from the

high-density (2x2) structure takes place in the absence of reconstructions. It must also take place in the presence of them. In spite of this constant desorption from (2x2), Figs. 5 and 6 show that the intensity of the c(2x2) pattern always increases in stages (ii) and (iii), and only begins to decrease (abruptly) when stage (iv) starts. Clearly, the presence of the reconstructions in stages (ii) and (iii) serves to constantly replenish the (2x2), whereas in stage (iv), where the reconstructions have disappeared, the (2x2) becomes permanently depleted. This last stage of desorption is signalled by growth of p(2x2) intensity, and simultaneous decrease in c(2x2) intensity.

The data also show that desorption from the (2x2) alone is not sufficient to explain the quasi-zero order γ state; there must also be some desorption process associated with the reconstructions. If desorption in the γ state were to occur predominantly from the (2x2) phase, then, as the system passed through regions (ii) and (iii), the isothermal desorption rate would increase in proportion to the amount of (2x2) phase. This expectation is not fulfilled. See, for instance, the periods between 180 and 300 s in Fig. 6A-D, or the periods between \sim 200 and 250 s in the data of Fig. 5A-E. In all cases, the (1/2, 1/2) spot intensity roughly triples at constant temperature, yet the desorption rate remains constant or even decreases slightly. Thus, part of the γ state must also originate from one or both of the reconstructions.

There must be some contribution to desorption from the $\sqrt{5}$ structure, based on data for stage (iii), such as that for the period

between 400 and 750 s in Fig. 6C-D. In this stage, the fractional area covered by (2x2) rises slowly but the desorption rate drops. The net drop in desorption rate must be due to the fact that the contribution to γ -state desorption from the $\sqrt{5}$ structure, whose area is decreasing, slightly outweighs the contribution from the (2x2) in this stage. There must also be significant contribution to desorption from the p(5x5) structure in stage (ii). Otherwise, the desorption rate would grow in proportion to the areas of the (2x2) and $\sqrt{5}$ structures which both increase rapidly in this stage. In fact, the desorption rate remains constant or decrease slightly, based on data such as that for the period between 180 and 350 s in Fig. 6A-D. The net constancy or decrease in desorption rate must again be due to a close balance between increasing desorption from the (2x2) and $\sqrt{5}$ structures, and decreasing desorption from the vanishing p(5x5) structure. In short, there are contributions to γ -state desorption from the $\sqrt{5}$ and p(5x5) reconstructions, as well as from (2x2). The net desorption rate in stages (ii) and (iii) represents a delicate balance between these three contributions.

It is intriguing to note that there is severe overlap of the β and γ peaks in the thermal desorption spectrum (cf. Fig. 4). This alone suggests that the rates of desorption (per unit area) in the two states are comparable. Upon inspection of thermal desorption data for other systems, we find that overlap between a quasi-zero-order state and more "normal" desorption states is quite common (2-12). This implies that simultaneous desorption from reconstructed and unreconstructed phases is important in the quasi-zero-order states of other systems as well.

To summarize this section, the data indicate that desorption originates from the high-density (2x2) and from both reconstructions, in the γ desorption state of O/Pd(100). Furthermore, even though desorption occurs from the (2x2), the latter is constantly replenished so long as reconstructed phases are present. Also, changes in the (2x2) pattern intensity are linked to concurrent changes in intensity of the reconstructions. The last two observations support the hypothesis that the (2x2) is in equilibrium with each reconstruction in two separate coexistence regimes [stages (i) and (iii)]. During passage between these two regimes, the system briefly spends time in stage (ii), where it is out of equilibrium and (2x2) coexists with both reconstructions.

V. MODELS FOR QUASI-ZERO-ORDER DESORPTION

Various models have been proposed to explain quasi-zero-order isothermal desorption kinetics. We briefly review these models here. Our goal is to identify viable models for the γ state of O/Pd(100), in light of the experimental data from previous sections. A detailed microscopic model, and an associated expression for the desorption rate, $R = -d\theta/dt$, is desired.

Horlacher Smith et al. (7) describe the sharp β_1 state of H/W(100) using an expression for the desorption rate,

$$R = \nu(\theta) \theta^2 \exp[-E_d(\theta)/kT]. \quad (1)$$

[Note that R here is in units of monolayers s^{-1} , and this defines the units of ν .] These authors find a dramatic coverage-dependence in the desorption energy, E_d , and in the prefactor, ν , from an isosteric analysis of experimental data. Jones and Perry (23,24) point out an alternative approach, in which attractive interactions can explain quasi-zero-order states. In this spirit, Barteau et al. (12) model the sharp state (named β_1) of O/Pt(100) by decomposing R into a part which describes desorption within the β_1 state, and a separate expression for desorption of the remaining species. The desorption energy, E_d ,

decreases linearly with decreasing coverage in the sharp state, presumably due to decreasing attractive interactions, and this reproduces the explosive isothermal desorption kinetics observed in experiment. Opila and Gomer (25) describe various desorption models where the adlayer consists of a "dense" island phase and (in some cases) one or more "dilute" phases. In these models, adlayer equilibrium is often not maintained. Opila and Gomer discuss models where desorption occurs predominantly from island edges, from the dilute phase, or from more than one phase competitively. A variant of the latter model has been developed by Bienfait and Venables (26), Asada (27), and Nagai et al. (28). They assume that the contribution to desorption from the "dense" phase does not involve direct desorption from islands, but rather from a dilute phase on-top of these islands. Their model has been invoked by Norton and Bindner (3) to describe the sharp α desorption state of H/Ni(100). Finally Sobyenin and Zhdanov (29) describe adsorbate-induced surface reconstructions in terms of first-order phase transitions, and apply mean-field kinetics to model thermal desorption spectra for H₂/Pt(100).

The discussion of experimental data for the O/Pd(100) system in Section IV guides us to consider two microscopic desorption models which are similar to models described in Refs. 25-28. These models necessarily involve competitive desorption from different, equilibrated

phases. The models also incorporate the non-equilibrium effects suggested by the data. The first model adapts ideas from Refs. 27-28, assuming that a dilute "on-top phase" exists above dense adlayer islands which, in our case, are islands of reconstruction. Desorption from the (2x2) and on-top phases occurs competitively, but there is no direct desorption from the reconstructed islands. The second model assumes that direct desorption from reconstructed islands competes with desorption from the (2x2) phase.

In both models, A_2 , A_5 and $A_{\sqrt{5}}$ denote fractional areas of the (2x2), p(5x5) and $\sqrt{5}$ phases, respectively, so these always sum to unity. During the equilibrated stages, (i) and (iii), these areas are calculated via tie-line constructions within the region of the phase diagram shown in Fig. 8. In the non-equilibrium stage (ii), a simple form for the A_i is adopted, based upon observed LEED behavior. Desorption from the (2x2) phase, of density ρ_2 , is assumed to occur via recombination of atoms of NNN sites. Its contribution to R has the form $k_2(\rho_2, T) P_2(\rho_2, T) A_2$. Here $k_2 = \nu_2 \exp(-E_2(\rho_2, T)/kT)$ is a microscopic desorption rate, where E_2 is the effective desorption energy, and P_2 is the probability of finding a NNN pair of filled sites, normalized to unity at $\rho_2 = 1/2$. The forms of P_2 and E_2 reflect oxygen-oxygen interactions. In the absence of reconstructed phases, clearly $A_2 = 1$ and $\rho_2 = 0$.

In the on-top phase model, let k_5^i ($k_{\sqrt{5}}^i$) denote the microscopic desorption rate, and P_5^i ($P_{\sqrt{5}}^i$) the probability of finding an "adjacent" pair of adatoms, which can recombinationally desorb, for the

phase on-top of $p(5 \times 5)$ ($\sqrt{5}$) regions. These quantities depend on the on-top phase density ρ_5' ($\rho_{\sqrt{5}}'$), and temperature, T . The total desorption rate is chosen as

$$R = k_2 P_2 A_2 + k_5' P_5' A_5 + k_{\sqrt{5}}' P_{\sqrt{5}}' A_{\sqrt{5}}, \quad (2)$$

which reduces to $k_2(\theta) P_2(\theta)$ in the absence of reconstructions. To reduce the variables to a manageable number, we mimic the treatment of Nagai et al. (28) in assuming that $k_5' P_5' = (1 + \delta_5) k_2 P_2$ and $k_{\sqrt{5}}' P_{\sqrt{5}}' = (1 + \delta_{\sqrt{5}}) k_2 P_2$, where δ_5 and $\delta_{\sqrt{5}}$ are constants. Thus R becomes

$$R = k_2 P_2 (1 + \delta_5 A_5 + \delta_{\sqrt{5}} A_{\sqrt{5}}). \quad (3)$$

Positive, zero, or negative values of δ correspond to decreasing, constant, or increasing R , respectively, for isothermal desorption in the coexistence region. From eq. (3), the γ -state desorption energy derived from Fig. 3, E_γ , is given by

$$E_\gamma = \frac{-d \ln R}{d(kT)^{-1}} = E_2(\rho_2) - \frac{\partial \ln P_2}{\partial \rho_2} \cdot \frac{\partial \rho_2}{\partial (kT)^{-1}} + \dots \approx 208 \text{ kJ/mol}. \quad (4)$$

The data show that E_γ is larger than the high-density (2×2) energy, $E_2(\rho_2) \approx 170 \text{ kJ/mol}$, and $\partial \ln P_2 / \partial \rho_2$ is obviously positive. Therefore, from eq. (4), ρ_2 must increase with T , i.e., the $(2 \times 2) / (2 \times 2) + \sqrt{5}$ phase

boundary must have finite positive slope, even though it is drawn with infinite slope in Fig. 8 and we assume that it has infinite slope in our tie-line constructions.

Just as in the calculations of Nagai et al. (28), the sharpness of the γ state in this model is enhanced by the non-decreasing (2x2) phase density, ρ_2 , in the coexistence region. The peak corresponds to crossing the phase boundary out of the coexistence region, after which the rapid drop in P_2 [or in θ for Nagai et al. (28)] results in a corresponding drop in R .

In the direct desorption model, the total desorption rate is chosen as

$$R = k_2 P_2 A_2 + k_5 A_5 + k_{\sqrt{5}} A_{\sqrt{5}}, \quad (5)$$

which reduces to $k_2(\theta) P_2(\theta)$ in the absence of reconstructions. The temperature dependence of P_i and k_i is implicit. Rates for direct desorption from the $p(5 \times 5)$ and $\sqrt{5}$ phases are chosen as $k_5 = \nu_5 e^{-E_Y/kT}$ and $k_{\sqrt{5}} = \nu_{\sqrt{5}} e^{-E_Y/kT}$, respectively, where $E_Y = 208$ kJ/mole (using results from Fig. 3). This model can also generate a sharp γ state, for essentially the same reasons as in the on-top phase model. For the parameters which best match the O/Pd(100) data, the peak occurs at the coexistence region phase boundary, where only (2x2) phase is present (as above); however, for other parameter choices it can occur slightly earlier.

Theoretical desorption spectra are shown in Fig. 10 for the direct desorption model and in Fig. 11 for the on-top phase model, with two choices of location of the coexistence region phase boundary. These model curves should be compared with the experimental curves of Fig. 4. The choice of model parameters, summarized in Table 2, is made by attempting to match the following aspects of the experimental desorption rate and LEED intensity data shown in Figs. 4-6: (a) the height, shape, and position of the sharp γ -state peak, particularly the onset of desorption at ca. 570 K; (b) the rough correspondence between the maximum of the γ -state and the transition from stage (iii) to (iv); (c) the relative magnitudes of the desorption rates in the fairly flat isothermal desorption stretches; (d) the time spent in the $\sqrt{5} + (2 \times 2)$ coexistence region [and specifically in stage (iii)]; and (e) the slight change in the slope, dR/dt , observed in the isothermal regime upon crossing from stage (ii) and (iii). Agreement between theory and experiment, for both models, is quite good. The five matching conditions (a) through (e) listed above place fairly severe constraints on fitting the experimental data, and so each set of values listed in Table 2 represents a uniquely good fit, given the model type and phase boundary location.

We treat the location of the $(2 \times 2)/(2 \times 2) + \sqrt{5}$ phase boundary as an adjustable variable, because of uncertainty in the experimentally-determined coverages. The best fit is provided by a phase boundary at $\theta = 0.40$, as shown by Figs. 10-11, and this is the location shown in Fig. 8. This is outside the range of the experimental

Figure 10. Desorption spectra for the direct desorption model, using two choices of $(2 \times 2)/(2 \times 2) \pm \sqrt{5}$ phase boundary: (A) $\theta = 0.40$ and (B) $\theta = 0.44$. Other parameters are given in Table 2. The initial coverage is $\theta = 0.55$ and the heating rate is 0.9 K/s, to match the experimental conditions of Fig. 4. The desorption rates for constant heating rate (solid curve), and for isothermal temperature programs at 613, 605, 595, and 588 K (dashed curves) are shown. In the constant-temperature regions, the changes in slope correspond to the points where the system crosses the $(2 \times 2)/(2 \times 2) + \sqrt{5}$ phase boundary.

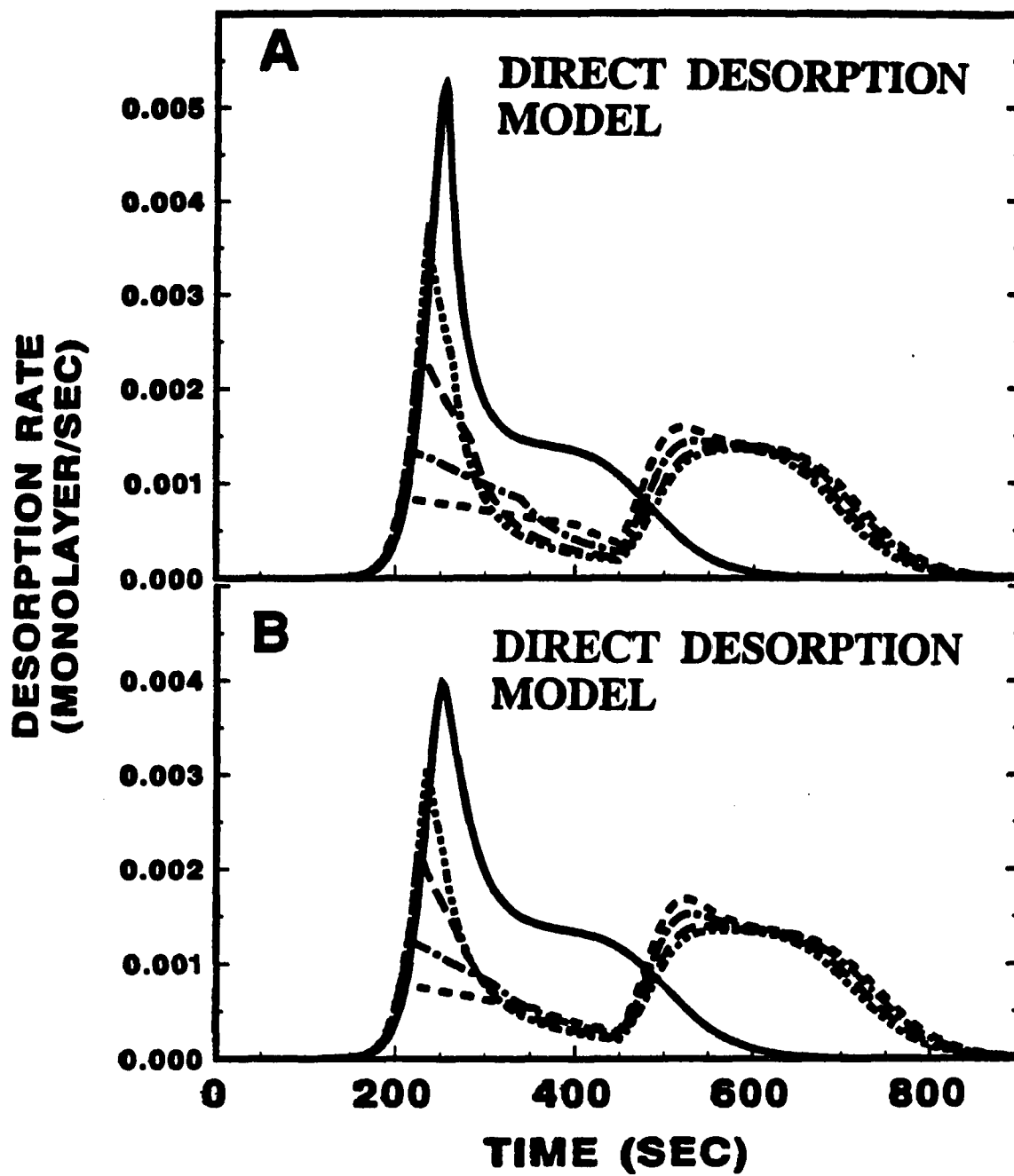


Figure 11. Desorption spectra for the on-top phase model, with two choices of $(2 \times 2)/(2 \times 2) + \sqrt{5}$ phase boundary: (A) $\theta = 0.40$, and (B) $\theta = 0.44$. Other parameters are given in Table 2. The initial coverage is $\theta = 0.55$ and the heating rate is 0.9 K/s, to match the experimental conditions of Fig. 4. The solid curve shows the desorption rate for constant heating rate, and the dashed curves show the desorption rates for isothermal temperature programs at 613, 605, 595, and 588 K. In the constant-temperature regions, the changes in slope correspond to the points where the system crosses the $(2 \times 2)/(2 \times 2) + \sqrt{5}$ phase boundary.

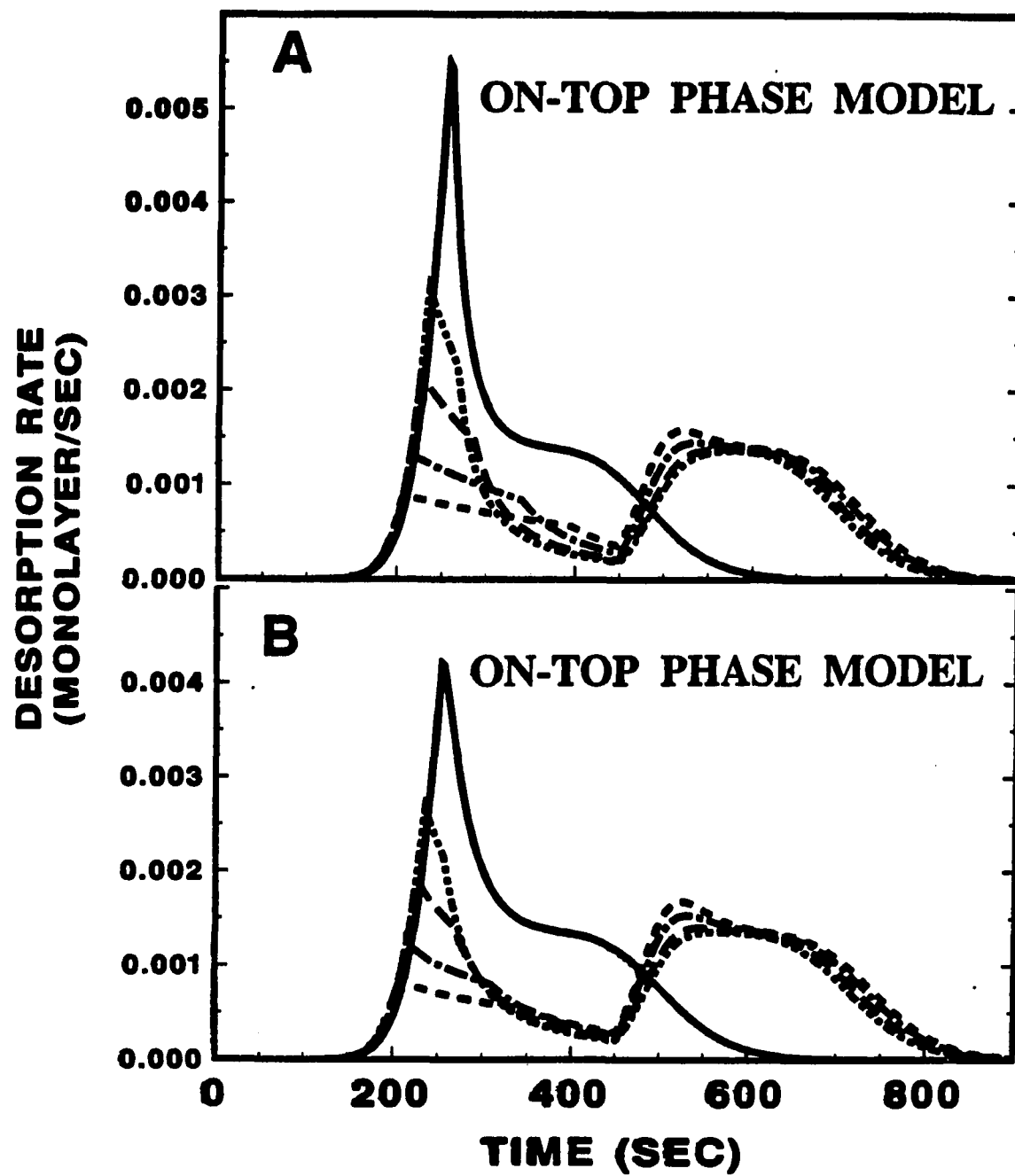


Table 2. Desorption parameters used to generate spectra of Fig. 10 and 11.

	Common Parameters			Direct Desorption Model Parameters			On-Top Phase Model Parameters	
	ν_2	E_0	ϵ	ν_5	$\nu_{\sqrt{5}}$	E_γ	δ_5	$\delta_{\sqrt{5}}$
(2x2)/(2x2)+ $\sqrt{5}$ phase boundary location in monolayers	s^{-1}	kJ/mol	kJ/mol	s^{-1}	s^{-1}	kJ/mol		
0.40	1.32×10^{12}	204.8	4.8	2.64×10^{15}	3.96×10^{15}	208	0.7	1.4
0.44	6.6×10^{11}	204.8	4.8	2.51×10^{15}	4.09×10^{15}	208	0.7	1.4

value, 0.50 ± 0.05 monolayers (16). At present we do not know how to reconcile this difference except to say that perhaps our experimental uncertainty is larger than ± 0.05 monolayers, presumably due to variations in the extent of bulk dissolution with initial coverage. Under no circumstances are we able to obtain a reasonable fit to the γ state when the phase boundary is placed at $\theta = 0.50$. Also, the appearance of the $p(2 \times 2)$ in stage (iii) of the reconstruction is compatible with a phase boundary at $\theta < 0.50$.

As an aside, we note that it is certainly possible to choose model parameters which produce a roughly linear increase in the isothermal desorption rate in the coexistence region, e.g., choose $\delta_5, \delta_{\sqrt{5}} < 0$ in the on-top phase model. However, to mimic explosive growth, such as that observed in the isothermal desorption rate for O/Pt(100) (12), requires a more fundamental change. For example, one could introduce desorption energies for the reconstructed phases which decrease with a decrease in the corresponding areas (cf. Ref. 12).

VI. DISCUSSION

The two models presented in Section V bear fundamental similarities. The direct desorption and on-top phase models both assume that a "dilute" surface phase is in equilibrium with a denser reservoir. [We ignore the brief nonequilibrium regime (ii), in this discussion.] In other words, a key element of both models is phase coexistence. In our system, the two observable phases which coexist are the (2x2) and $\sqrt{5}$. Similar coexistence regimes are probably quite common in phase diagrams of systems involving adsorbate-induced reconstructions. In particular, we expect that phase coexistence between an adsorbate on a reconstructed substrate and on an unreconstructed substrate may prove common. Such coexistence may easily go undetected where hydrogen is the adsorbate, since hydrogen on an unreconstructed substrate often produces only a (1x1) LEED pattern, i.e., it is usually impossible to distinguish the chemisorbed (1x1) phase from the clean surface, or from the reconstruction. Perhaps for this reason, coexistence regions have not generally been identified in phase diagrams of systems such as H/W(100) (7). However, coexistence implies a first-order transition between the two phases, and the nucleation-and-growth mechanism often associated with first-order transitions has been identified for several adsorbate-induced reconstructions, e.g., CO/Pt(100) (30), O/Ni(110) (31), and H/Ni(110) (4,32). This suggests that coexistence regimes may be fairly general in systems with adsorbate-induced reconstructions.

The importance of the coexistence region lies in the fact that the chemical potentials above two phases in equilibrium are identical (26-28). If the sticking coefficients into the two phases are equal or similar (25), the desorption rates per unit area will also be equal or similar (25-28). [Thus far, the argument is very similar to that given by Estrup, Cardillo, and coworkers (7,33,34) to explain compensating changes in desorption rate parameters as a system crosses a phase boundary.] Therefore, the system exhibits desorption characteristics which are close to zero-order. This can be understood simply: so long as the combined area covered by the two desorption sources remains constant (as it does throughout a coexistence regime), the total rate of desorption must also remain constant, even though coverage is changing and the microscopic desorption process is not zero-order.

The difference between the two models is in the nature of the equilibrated desorption sources. In the on-top phase model, a dense phase (such as a reconstruction) supplies adsorbate to two more dilute phases, one atop the substrate and one atop the dense phase. The dilute phases are the desorption sources, and in our system they would necessarily be the (2x2) chemisorbed phase and some sort of oxygen atop the reconstructed areas. As shown in Section V, parameters can be chosen such that this model fits all aspects of our data well. Quasi-zero order desorption results because the desorption rate per unit area from the (2x2) and the on-top phase happens to be of comparable magnitude. For instance, using the parameters of Table 2 for a phase

boundary at $\theta = 0.40$, the desorption rates (in monolayers s^{-1} per unit fractional area) from (2x2), p(5x5), and $\sqrt{5}$ at 600 K are 0.79×10^{-3} , 1.34×10^{-3} , and 1.89×10^{-3} , respectively.

However, it is difficult to rationalize the on-top phase, where stable oxygen must exist on top of the reconstruction, because oxygen density is already very high in the reconstruction. Furthermore, in chemisorption systems where quasi-zero-order kinetics have been related to surface reconstructions, no such on-top phase has been identified spectroscopically under any conditions, even though such a phase should be as stable as the normal chemisorbed phase (unlike a mobile precursor).

The direct desorption model is simpler, and assumes that the two desorbing phases (in our system) are one of the reconstructions and the (2x2). Note that these are both very dense phases, i.e., it is not appropriate to think of one phase as "dense" and the other as "dilute" (25). It is reasonable, therefore, that adsorption probabilities into the high-density (2x2) and the reconstructed phases might be comparable, leading to comparable desorption rates per unit area. Using the parameters of Table 2 for a phase boundary at $\theta = 0.40$, the desorption rates (in monolayers s^{-1} per unit fractional area) from the (2x2), p(5x5), and $\sqrt{5}$ at $T = 600$ K are indeed comparable: 0.79×10^{-3} , 2.06×10^{-3} , and 3.08×10^{-3} , respectively.

The differences between these two models may, ultimately, be more semantic than real. The dilute on-top phase is not a true independent thermodynamic phase; rather, its area is fixed by the area of the

underlying reconstruction, and its density does not vary. Thus, it is more appropriate to think of the on-top phase as a kind of virtual state, an intermediate between the reconstruction and the gas phase. In this sense, the physical distinction between the "on-top model" and the "direct desorption model" ultimately breaks down.

VII. ACKNOWLEDGMENTS

We thank Wen-Di Wang for helping with the experiments, and we thank Lyle Roelofs for insightful discussions. This work is supported by the Director for Energy Research, Office of Basic Energy Sciences. Ames Laboratory is operated for the U.S. Department of Energy by Iowa State University under Contract No. W-7405-ENG-82.

VIII. REFERENCES

1. P. J. Estrup, "Reconstruction of Metal Surfaces," Ch. 9 in Chemistry and Physics of Solid Surfaces V, R. Vanselow and R. Howe, Ed., Springer-Verlag, Berlin (1984) pp. 205-230.
2. K. Christmann, V. Penka, R. J. Behm, F. Chehab and G. Ertl, *Solid State Commun.* 51 (1984) 487; also K. Christmann, F. Chehab, V. Penka and G. Ertl, *Surface Sci.* 152/153 (1985) 356.
3. P. R. Norton and P. E. Bindner, *Surface Sci.* 169 (1986) L259.
4. T. E. Jackman, K. Griffiths, W. N. Unertl, J. A. Davies, K. H. Gurtler, D. A. Harrington and P. R. Norton, *Surface Sci.* 179 (1987) 297.
5. R. J. Behm, V. Penka, M.-G. Cattania, K. Christmann and G. Ertl, *J. Chem. Phys.* 78 (1983) 7486.
6. K. H. Rieder, M. Baumberger and W. Stocker, *Phys. Rev. Letters* 51 (1983) 1799.
7. A. Horlacher Smith, R. A. Barker and P. J. Estrup, *Surface Sci.* 136 (1984) 327.
8. P. J. Estrup, Dept. of Phys., Brown Univ., private communication.
9. P. R. Norton, K. Griffiths and P. E. Bindner, *Surface Sci.* 138 (1984) 125.
10. K. Griffiths, T. E. Jackman, J. A. Davies and P. R. Norton, *Surface Sci.* 138 (1984) 113.

11. G. N. Derry and P. N. Ross, *Surface Sci.* 140 (1984) 165.
12. M. A. Barteau, E. I. Ko and R. J. Madix, *Surface Sci.* 102 (1981) 99.
13. G. Ertl and J. Koch, *Z. Phys. Chem.* 69 (1970) 323.
14. T. W. Orent and S. D. Bader, *Surface Sci.* 115 (1982) 323.
15. E. M. Stuve, R. J. Madix and C. R. Brundle, *Surface Sci.* 46 (1984) 155.
16. S.-L. Chang and P. A. Thiel, *J. Chem. Phys.* 88 (1988) 2071.
17. J. W. Anderegg and P. A. Thiel, *J. Vac. Sci. Technol.* A4 (1986) 1367.
18. P. A. Thiel and J. W. Anderegg, *Rev. Sci. Instrum.* 55 (1984) 1669.
19. H. Herz, H. Conrad and J. Küppers, *J. Phys. E* 12 (1979) 369.
20. J. A. Polta, P. J. Schmitz and P. A. Thiel, *Langmuir* 3 (1987) 1178.
21. S.-L. Chang and P. A. Thiel, Chem. Dept., Iowa State Univ., in preparation.
22. M. Milun, P. Pervan and K. Wandelt, *Surface Sci.* 189/190 (1988) 466.
23. R. G. Jones and D. L. Perry, *Surface Sci.* 71 (1978) 59.
24. R. G. Jones and D. L. Perry, *Surface Sci.* 82 (1979) 540.
25. R. Opila and R. Gomer, *Surface Sci.* 112 (1981) 1.
26. J. A. Venables and M. Bienfait, *Surface Sci.* 61 (1976) 667.
27. H. Asada, *J. Res. Inst. Catalysis* 30 (1982) 55.
28. K. Nagai, T. Shibanuma and M. Hashimoto, *Surface Sci.* 145 (1984) L459.

29. V. A. Sobyenin and V. P. Zhdanov, *Surface Sci. Lett.* 181, L163 (1987); also V. P. Zhdanov, *Surface Sci. Lett.* 164, L807 (1985).
30. R. J. Behm, P. A. Thiel, P. R. Norton and G. Ertl, *J. Chem. Phys.* 78 (1983) 7437.
31. R. J. Behm, G. Ertl and J. Winterlin, *Ber. Bunsenges. Phys. Chem.* 90 (1986) 294.
32. R. J. Behm, K. Christmann, G. Ertl, V. Penka, and R. Schwankner, in The Structure of Surfaces edited by M. A. Van Hove and S. Y. Tong, Springer-Verlag, Berlin (1985) p. 257.
33. P. J. Estrup, E. F. Greene, M. J. Cardillo and J. C. Tully, *J. Phys. Chem.* 90 (1986) 4099.
34. M. J. Cardillo and J. C. Tully, in Dynamics on Surfaces, Ed. by B. Pullman, D. Reidel Publishing Co., Holland (1984) 169.

PAPER V:

PHASE DIAGRAM OF O/Pd(100)

PHASE DIAGRAM OF O/Pd(100)

S.-L. Chang and P. A. Thiel

Department of Chemistry and Ames Laboratory-USDOE
Iowa State University
Ames, Iowa 50011 USA

ABSTRACT

A complete phase diagram of oxygen on the Pd(100) surface is constructed based on results obtained from LEED experiments. Two reconstructed phases and the bulk oxide, in addition to the two chemisorbed phases, complicate the phase diagram. We perform two kinds of experiments, i.e., isothermal adsorption and isosteric heating-cooling cycles, to demonstrate that this θ -T diagram is truly representative of a thermodynamically-allowed phase diagram.

I. INTRODUCTION

Two-dimensional order-disorder, and order-order, phase transformations have been subjects of interest for many years (1,2). Due to the lateral interactions between adsorbed particles, and the site-dependent interactions between a particle and the substrate, ordered structures can be observed on single crystal surfaces after adsorption. By examining phase transition phenomena on such a well defined lattice, problems related to adatom-adatom and adatom-substrate interactions can be understood. A great number of studies based on experimental results or theoretical models have been performed. Low-energy electron diffraction is one of the most widely-used experimental probes in studying this subject. The diffraction pattern, containing detailed information about the long- and short-range order of the adlayers, can be investigated at various coverages and temperatures. This information can be extended to construct a phase diagram for a particular system. Experimentally, it is common to change the sample temperature at a fixed coverage (isosteric heating/cooling) to obtain the transition temperatures or to change the coverage at a fixed sample temperature (isothermal adsorption/desorption) to map out the coverage-dependent phase changes. Phase diagrams based on these methods have been established for many systems, for example, O/Ni(111) (3), H/Ni(111) (4), H/Pd(111) (5), H/Pd(100) (6), O/W(110) (7) and H/W(001) (8). In this paper we report the phase diagram of the system O/Pd(100) at temperatures above 400 K. The importance of this study is that the

reconstructions induced by oxygen introduce a great deal of complexity to the phase diagram.

II. EXPERIMENTAL PROCEDURES

The experiments are carried out in an ion pumped stainless steel ultra-high vacuum chamber equipped with AES, LEED, QMS and inert gas ion sputter gun. The typical base pressure is 8×10^{-11} Torr after bake out and 2×10^{-10} Torr between oxygen gas doses. The procedures for sample preparation (9), and the experimental set up for the video-LEED are described elsewhere (10).

The same parameters described previously (9,10) are used in this work to acquire LEED data. These parameters give a heating rate which is equal to 1.0 ± 0.2 K/s and a temperature fluctuation which is about ± 6 K from the average value.

III. EXPERIMENTAL RESULTS

We report two experimental results based on isothermal adsorption experiments and repeated heating-cooling experiments. In both kinds of experiments, changes in LEED spot intensities and profiles are monitored as a function of oxygen exposure or sample temperature. The isothermal adsorption experiments are performed by introducing oxygen gas into the chamber with the sample temperature fixed. The heating and cooling experiments are done by varying the temperature of an oxygen covered sample.

The purpose of this paper is to construct a thermodynamically-allowed phase diagram of the system O/Pd(100) by using, partly, previous data (9) and the present results. The final result is illustrated in Fig. 1. The horizontal arrows in Fig. 1 correspond to the isothermal adsorption experiments which move transverse through the phase diagram. The two-way vertical arrows indicate the areas in which the heating and cooling experiments are carried out to test the reversibility of phase transformations.

A. Isothermal Adsorption

The ordered superlattice structures are formed upon adsorption of oxygen at sample temperatures between 300 K and 400 K. We measure both integrated spot intensities and one-pixel cut spot profiles of diffraction patterns as a function of oxygen exposure. In this paper we use the same set of spots to gain information about the different LEED

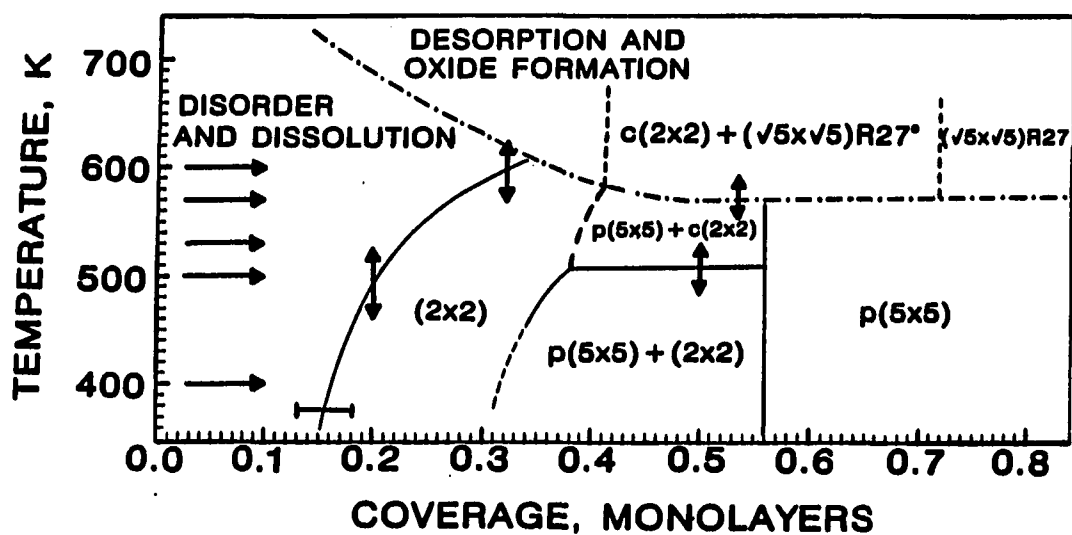


Figure 1. Phase diagram of the system O/Pd(100). The solid boundaries are based on the experimental results. The dashed lines are proposed boundaries. The dot-dashed line represents the onset of desorption. The arrows on the left-hand side represent the temperatures where isothermal adsorption experiments are performed. The vertical two-way arrows indicate the coverages where the reversibility of ordered phases at different temperatures are tested.

patterns as used previously (9). We briefly summarize it here. The $(1/2, 1/2)$ and $(0, 1/2)$ spots both appear in the $p(2 \times 2)$ pattern but only the $(1/2, 1/2)$ spot is seen in the $c(2 \times 2)$ structure. Two fifth-order spots representing the reconstructions are $(1/5, 1/5)$ and $(1/5, 2/5)$. Both of them appear in the $p(5 \times 5)$ structure but only the $(1/5, 2/5)$ spot can be observed in the $(\sqrt{5} \times \sqrt{5})R27^\circ$.

Figure 2 shows LEED spot intensities versus exposure (in units of Langmuirs, $1 \text{ L} \equiv 10^{-6} \text{ Torr} \times \text{sec}$) plotted at various adsorption temperatures. The corresponding changes in the FWHM of spot profiles are shown in Fig. 3. Due to the onset of desorption and bulk dissolution at higher temperatures (above 400 K), it is not possible for us to put down meaningful coverage values in the temperature regime above 400 K, especially at high exposures. Therefore, we choose to use exposure instead of coverage as an index of the relative amount of oxygen to which the sample is exposed. Nevertheless, we are still able to obtain the coverage value from our TPD results for the experiments performed at 400 K and below (9).

1. Adsorption at 300 K

There are two structures, $p(2 \times 2)$ and $c(2 \times 2)$, observed up to 50 L ($\theta = 0.45$) of exposure at this temperature as shown in Fig. 2a. These structures have been studied previously by the following two groups: Orent and Bader (11) and Ertl and Koch (12). When Ertl and Koch first studied this system, they did not succeed in forming the $c(2 \times 2)$ structure. Later, Orent and Bader showed a drastic drop in the oxygen

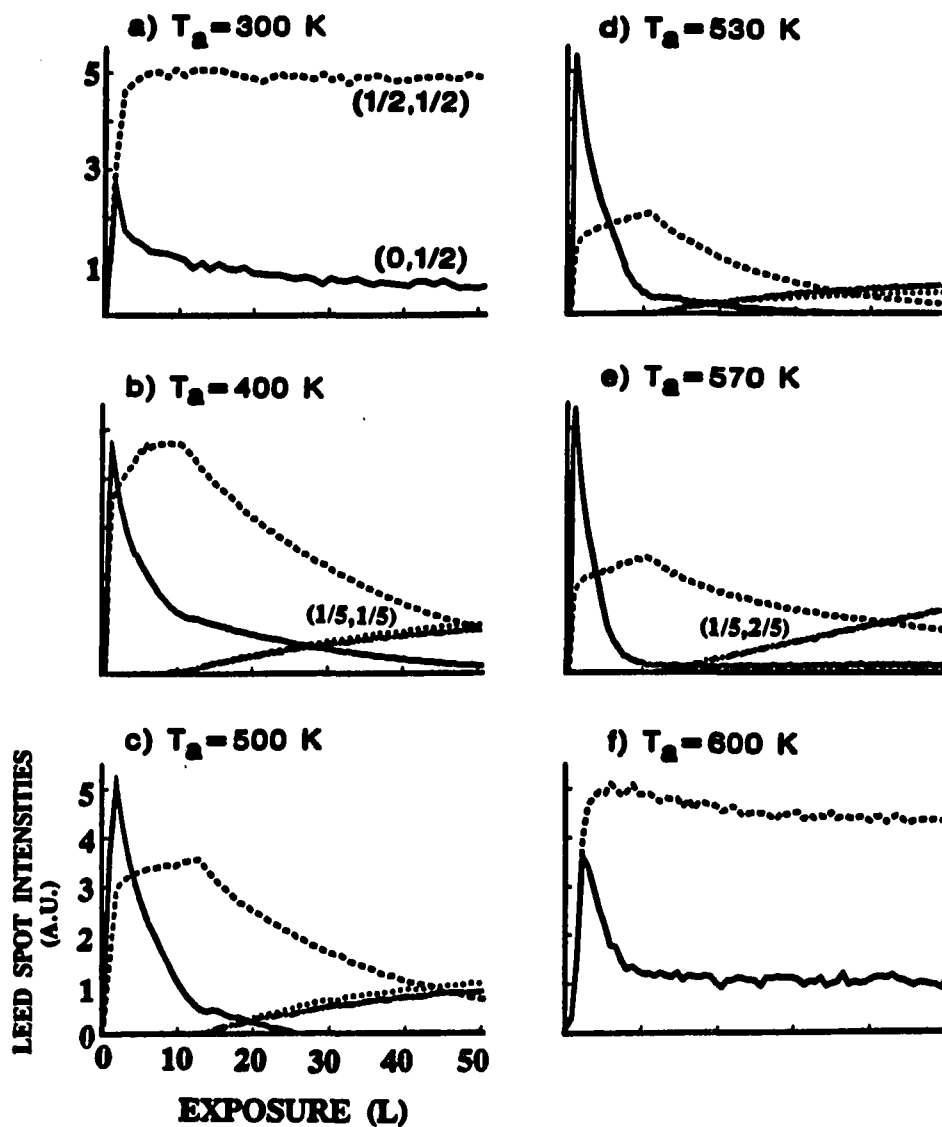


Figure 2. Adsorption isotherms at various adsorption temperature:
 a) $T_a = 300$ K, b) $T_a = 400$ K, c) $T_a = 500$ K, d) $T_a = 530$ K, e) $T_a = 570$ K, f) $T_a = 600$ K. The LEED spot intensities vs. exposure are plotted. Solid line represents (0, 1/2) spot, dashed line (1/2, 1/2) spot, dotted line (1/5, 1/5) spot, dot-dashed line (1/5, 2/5) spot. LEED beam energy is fixed at 64 eV. $P_{O_2} = (3 \sim 6) \times 10^{-8}$ Torr

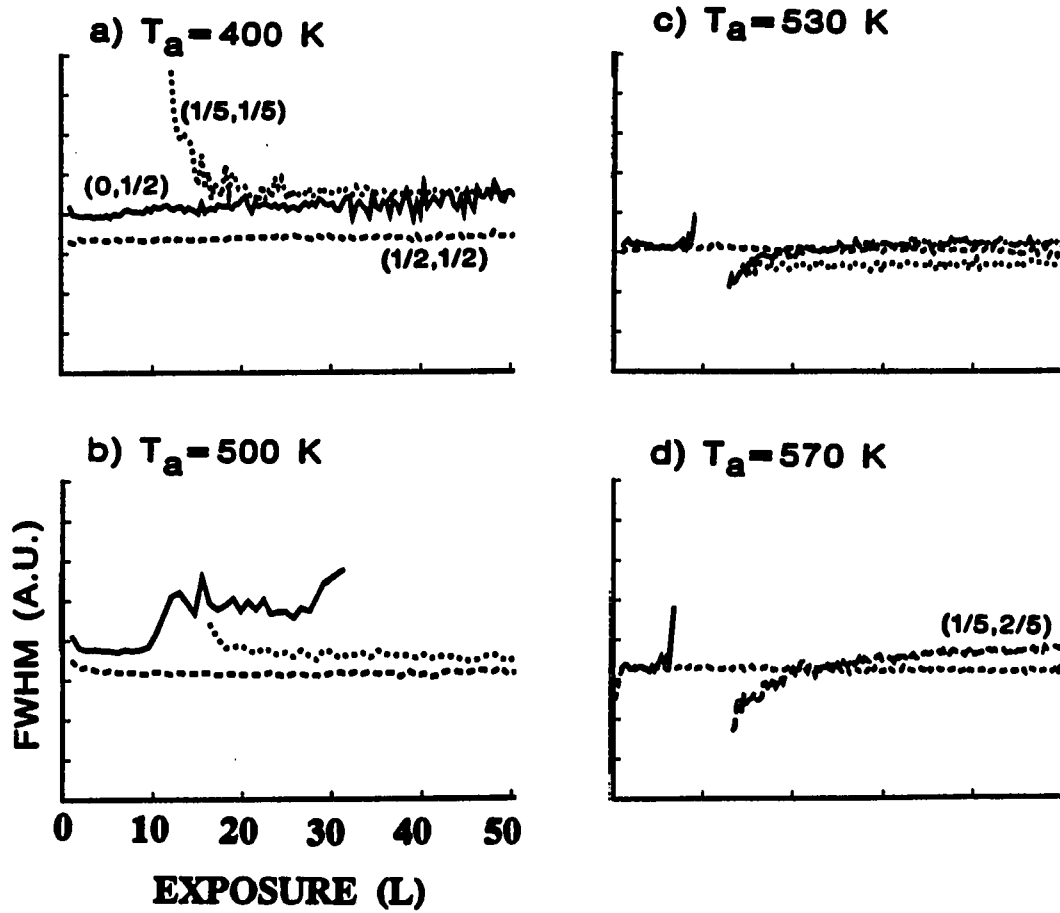


Figure 3. FWHM of spot profiles corresponding to Fig. 1:

a) $T_a = 400$ K, b) $T_a = 500$ K, c) $T_a = 530$ K, d) $T_a = 570$ K.

The same symbols used to represent different spots in Fig. 2 are used here again.

sticking coefficient on this surface after the $p(2 \times 2)$ structure is formed, which was confirmed by Stuve et al. (13). Our LEED and AES results are very consistent with the results obtained by Orent and Bader. The $p(2 \times 2)$ structure, ideal coverage 0.25 monolayers, forms immediately after adsorption starts and reaches perfection at 1 L ($\theta = 0.25$). Following the formation of this pattern, the sticking coefficient drops rapidly. This is probably due to the fact that formation of the $p(2 \times 2)$ structure destroys the eight-site ensemble required (14,15) for further adsorption.

2. Adsorption at 400 K

Figure 2b shows the results when adsorption takes place at 400 K. Below 10 L ($\theta = 0.38$), two ordered structures similar to those at 300 K are observed. However, several interesting changes occur simultaneously associated with a drastic increase in oxygen uptake beyond 10 L.

First, we notice that a new pattern emerges with fifth-order spot characteristics. This pattern has been previously assigned as a $p(5 \times 5)$ reconstruction, based on the fact that its unit cell dimensions are very similar to the unit cell of the (110) plane of bulk PdO (11). Note that this structural assignment is completely based on the periodicity of the observed LEED pattern, however. More sophisticated methods are needed to confirm that the arrangement of oxygen and Pd atoms within the $p(5 \times 5)$ unit cell is indeed similar to that of PdO(110). The ideal coverage for this proposed structure is 0.64 monolayers. Because this $p(5 \times 5)$ structure is observed after the $c(2 \times 2)$ structure, it is reasonable to

assume that its coverage is higher than the ideal coverage of the $c(2 \times 2)$, 0.50 monolayers. This assumption is confirmed by our previous TPD results (9) which show an increase in the integrated peak areas when the $p(5 \times 5)$ appears. The second noteworthy change is the intensities of half-order spots. The $(1/2, 1/2)$ spot, which represents both the $c(2 \times 2)$ pattern and the $p(2 \times 2)$ structure, shows a sudden break in its intensity. In other words, the intensity changes from a slow increase to a rapid decrease. On the other hand, the intensity of $(0, 1/2)$ spot changes from a rapid decrease to a slow decrease. The large difference between their intensities indicates that the surface is covered primarily by the $c(2 \times 2)$ structure at the coverage where these breaks occur. The rapid decline in the intensity of the $(1/2, 1/2)$ spot associated with the appearance of the fifth-order spots implies that the formation of the $p(5 \times 5)$ is mainly due to replacement of the $c(2 \times 2)$ structure.

This observation is enforced by examining the changes of FWHM of spot profiles shown in Fig. 3a. The reciprocal FWHM of a spot profile is proportional to the correlation length which can be associated with the average domain size. The $(1/2, 1/2)$ spot has a very small and coverage-independent FWHM, indicative of large domains of $c(2 \times 2)$. The $p(5 \times 5)$ domains grow by showing a continuous decrease in the FWHM of the $(1/5, 1/5)$ spot from exposures 10 L to 20 L. After 20 L of exposure, the FWHM stops decreasing and reaches a minimum value. Note that the $(1/5, 1/5)$ spot intensity keeps on increasing in this region (cf. Fig. 1b). We do not consider that the behavior of the $(1/5, 1/5)$ spot profile after 20 L of exposure is due to the limited resolution of our

instrument because we can still observe spots with smaller FWHM. Instead, we propose the following explanation: During the initial stage of growth, the $p(5 \times 5)$ reconstruction follows the nucleation and growth mechanism which sharpens the fifth order spots. As the coverage increases, the $p(5 \times 5)$ domains reach their maximum size (see below) and stop growing. However, small domains of $p(5 \times 5)$ which probably have only little effect on the correlation length of the fifth-order spot can still be formed to further intensify the spot. The saturation of the $(1/5, 1/5)$ spot FWHM after 20 L is probably because the disrupted areas which circumscribe these $p(5 \times 5)$ domains act as boundaries to prevent the large $p(5 \times 5)$ domains from coalescing. This postulation is shown schematically in Fig. 4.

According to the phase diagram shown in Fig. 1, the coverage on the surface after 20 L of exposure at this temperature is about 0.5 monolayers. By using the tie-line configuration in phase rule, we can obtain an estimate which shows that there is only 20% of the total area left unreconstructed for oxygen adsorption. The small open area remaining on the surface may be an explanation for the rapid saturation of the $p(5 \times 5)$ domains and the slow development of the spot intensity after 20 L of exposure.

The invariant FWHM of the $(1/2, 1/2)$ spot in Fig. 3a is probably due to the instrument limitation. However, it is also possible that the correlation length for the $c(2 \times 2)$ domains is so large that the appearance of the $p(5 \times 5)$ reconstruction cannot change it. Note that if this is the case, then the growth of the $p(5 \times 5)$ structure at the expense

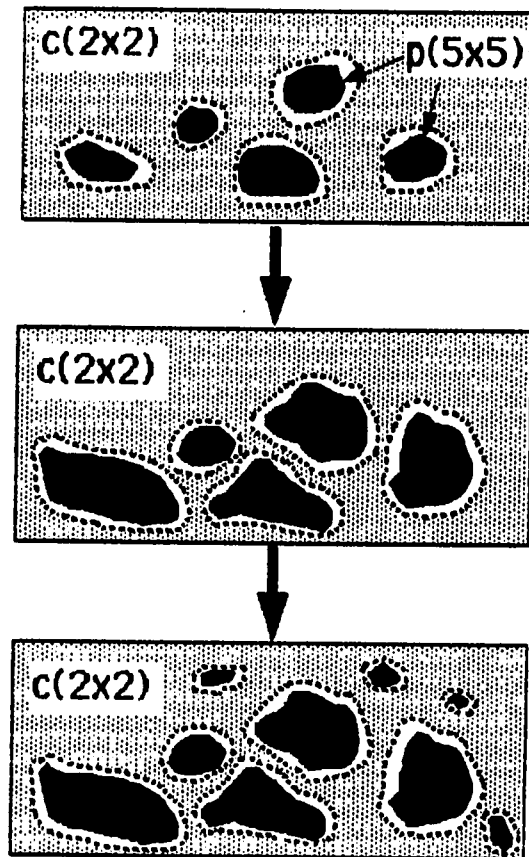


Figure 4. Proposed mechanisms for the $p(5 \times 5)$ domain growth.

- a) $p(5 \times 5)$ domains surrounded by disrupted areas reconstruct in the $c(2 \times 2)$ matrix.
- b) The reconstructed $p(5 \times 5)$ areas grow as coverage increases, but the disrupted areas make domains coalescence impossible.
- c) Small $p(5 \times 5)$ structures grow, but they are too small to affect the FWHM of the $(1/5, 1/5)$ spot.

of the $c(2 \times 2)$ structure must have a different effect on the correlation length of the $c(2 \times 2)$ as compared to the development of defect or empty holes in the $c(2 \times 2)$ structure. The latter usually decrease the correlation length thus broadening the spot profile.

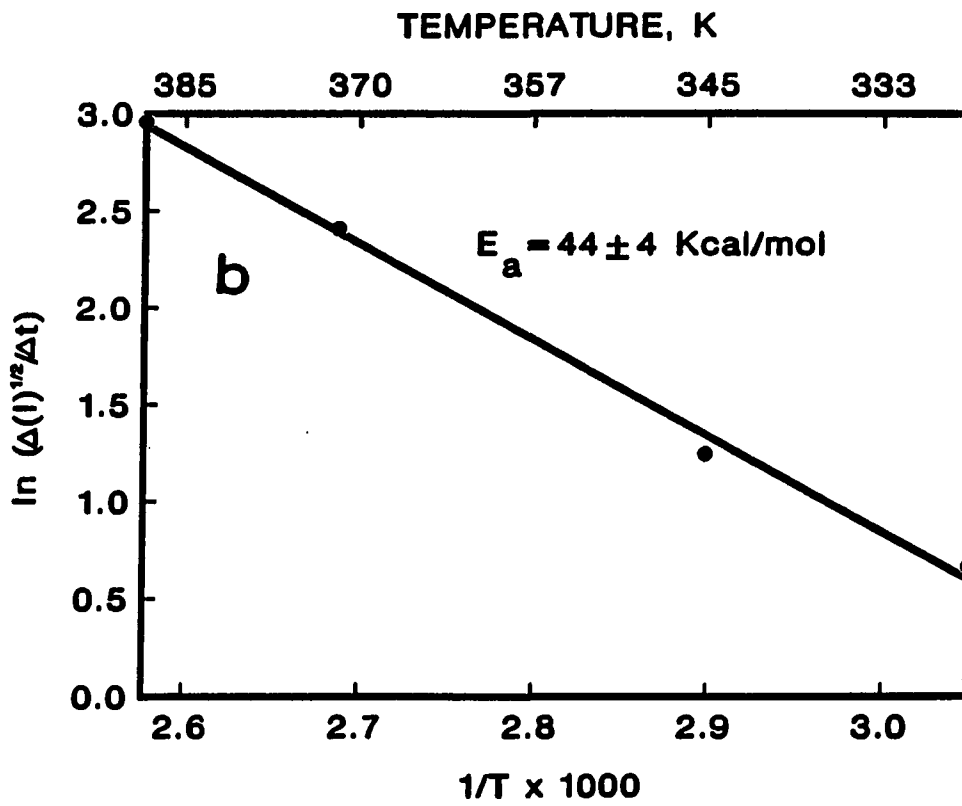
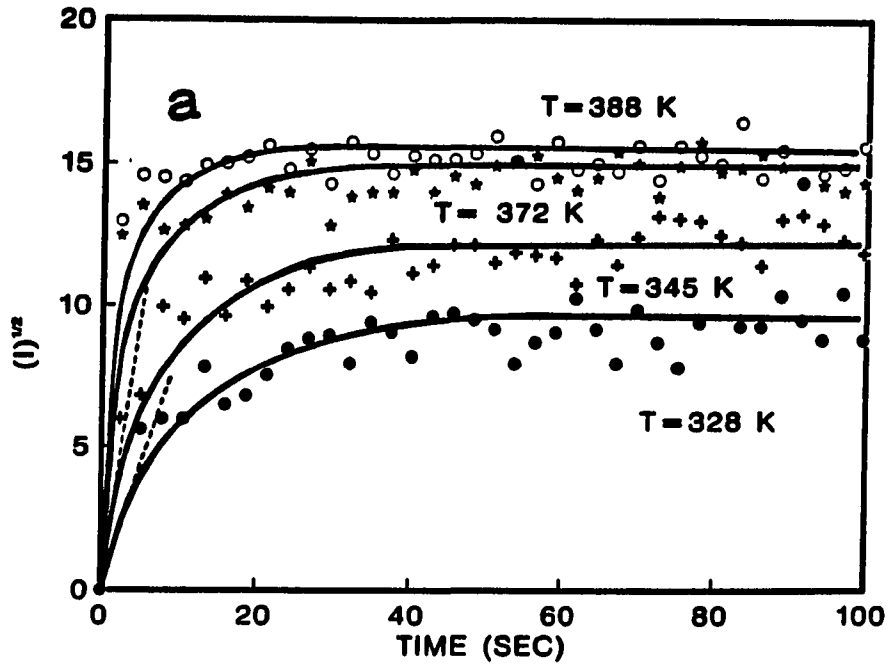
By comparing the results shown in Figs. 2a and 2b, it seems that the $p(5 \times 5)$ is formed only at elevated temperatures. This observation implies that there exists an activation barrier between the unreconstructed structure and the reconstructed structure which needs to be overcome in order to form the $p(5 \times 5)$ structure. However, an alternate explanation must be considered. It is commonly observed in group VIIIB elements that a clean-off reaction by background H_2 and CO can take place at room temperature to prevent the oxygen coverage on the surface from building up (16). The effects of the clean-off reaction can be minimized by maintaining the substrate at higher temperatures where the adsorption probabilities of H_2 and CO decrease but the adsorbed oxygen is still stable on the surface. This could be an alternate explanation for why the high-coverage $p(5 \times 5)$ oxygen structure only develops at high temperatures. In order to test whether the clean-off reaction is important in our system, we perform experiments by cooling an existing $p(5 \times 5)$ structure back to room temperature. The result shows that the formation of the $p(5 \times 5)$ is an irreversible process, i.e., the $p(5 \times 5)$, once formed, is stable even at room temperature, where clean-off would be fast. Therefore, we conclude that there must be an activation barrier separating the unreconstructed surface from the reconstructed surface.

The activation barrier of this phase transformation can be obtained by monitoring the intensity changes of the fifth-order spot as a function of time in an "up-quench" experiment. This is done by adsorbing 60 L of oxygen at 300 K which gives a coverage about 0.49 monolayers. This coverage guarantees that the surface is covered mostly by the $c(2 \times 2)$ structure. After oxygen is evacuated, the sample is heated rapidly (heating rate ≈ 30 K/s) to a temperature around 400 K to form the $p(5 \times 5)$ structure. The square root of the intensity of the fifth order spot is plotted as a function of time. The result is shown in Fig. 5a. The heating is applied between $t = -1$ and -3 seconds to the final temperature indicated on the right of Fig. 5a. From $t = 0$, where the intensity of the $(1/5, 1/5)$ spot is zero, the data are recorded until the intensity reaches an asymptote. The square root of the intensity is used because the intensity value is proportional to the square of the average domain size (17,18).

Several experimentalists have employed this up-quench method to study the dynamics of two-dimensional phase ordering. The diffusion barriers of oxygen on $W(112)$ (19) and $Rh(111)$ (20) surfaces have been obtained by such a technique. In our experiment, the initial slope changes of the square root of the $(1/5, 1/5)$ spot intensity as a function of time are plotted against $1/T$ where T is the final annealing temperature. The result is shown in Fig. 5b. The activation energy of the $p(5 \times 5)$ reconstruction is calculated from the slope of this Arrhenius plot. The value we obtain is 44 ± 4 kJ/mol. It is of interest to compare our result with the results of other adsorbate-induced

Figure 5a. Square root of the (1/5, 1/5) spot intensity plotted against time in the up-quench experiment. When $t = 0$ there is no (1/5, 1/5) spot, after 100 seconds, the intensity of the (1/5, 1/5) spot reaches a plateau. The final temperatures are shown on the right. The dashed lines indicate the initial intensity changes as a function of time.

Figure 5b. The Arrhenius plot of the initial slopes obtained from dashed lines in (a) vs $1/T$. The slope of this curve gives the activation energy.



reconstruction systems, for example, H/Ni(110) (21) and O/Ni(110) (22). The reconstruction of the Ni(110) surface induced by hydrogen is a nonactivated process occurring at $T < 180$ K, while the system O/Ni(110) has an activation energy 25 kJ/mol and occurs at $T > 250$ K. The activation energy required for oxygen to reconstruct the Pd(100) surface is about 20 kJ/mol higher than that required for oxygen to reconstruct the Ni(110) surface. This is why we can only observe the $p(5 \times 5)$ structure at 400 K or above. We think that the relative ease of reconstruction of these two metal surfaces might be related to the ease with which the bulk metals oxidize. It is known that Ni oxidizes more easily than Pd, therefore, surface atoms in Ni are probably more readily reconstructed than those in Pd. The fact that the Ni(110) face is more open than the Pd(100) face might also contribute to the lower energy barrier for Ni(110) reconstruction.

3. Adsorption at 500 K

The three patterns observed at 400 K reappear at this temperature, as shown in Fig. 2c. However, a higher dosage (~ 14 Langmuirs) is required to form the reconstruction. This is presumably due to the inverse relation between the sticking probability and temperature, although the possibility of bulk dissolution can not be ruled out as well. The other difference we note at this temperature is that the intensity of the $(0, 1/2)$ spot at its maximum is about 1.5 times that of the $(1/2, 1/2)$ spot. This situation contrasts adsorption at temperatures below 300 K where we observe a monotonic lowering of the

maximum intensity of the $(0, 1/2)$ spot as we decrease the adsorption temperature (15). We rationalize the phenomenon at $T > 300$ K by postulating that larger arrays of $p(2 \times 2)$ domains with fewer domain boundaries can form due to the higher mobility of oxygen atoms at higher temperatures. However, we do not have other experimental data to support this assumption. The other possible explanation is that the Debye-Waller factors are different for different beams, in which case there is more effect on the $(1/2, 1/2)$ spot than on the $(0, 1/2)$ spot at higher temperatures.

Comparing with the results obtained at 400 K, it is clear that at this adsorption temperature (500 K) the energy barrier to reconstruct the surface has been overcome; however, the signal of reconstruction, shown by the appearance of the $p(5 \times 5)$ structure, does not show up immediately when adsorption is turned on. This implies that a minimum nucleus size to start the reconstruction is required to activate the process. Once the surface is reconstructed, the $p(5 \times 5)$ structure develops gradually by replacing the $c(2 \times 2)$ structure. In other words, the reconstruction does not cover the entire surface all at once. This is seen from the slow variations in the intensities of the $(1/2, 1/2)$ and $(1/5, 1/5)$ spots in Fig. 2c. All these observations imply that the reconstruction of the Pd(100) surface induced by oxygen follows the nucleation and growth mechanism.

The FWHM of the $(1/5, 1/5)$ spot shown in Fig. 3b indicates that the average domain size of the $p(5 \times 5)$ structure at saturation is somewhat larger (about 30% larger) than that at 400 K at saturation. The fact

that larger $p(5 \times 5)$ domains can be observed at higher temperatures is probably because there are fewer domain boundaries. In other words, the $p(5 \times 5)$ domains have a better chance to coalesce at higher temperatures. Such a high temperature annealing effect will be observed in the following experiments, too.

4. Adsorption at 530 K

At this adsorption temperature, the $p(5 \times 5)$ reconstruction is first seen at 13 L. Figure 2d shows this result. The two fifth-order spots, $(1/5, 1/5)$ and $(1/5, 2/5)$, develop in a slightly different manner than they do at 500 K and 400 K as coverage increases. First, the intensity is slightly higher for the $(1/5, 2/5)$ spot than for the $(1/5, 1/5)$ spot. Second, as the coverage increases, the $(1/5, 2/5)$ spot develops more, while the $(1/5, 1/5)$ spot weakens slightly yet still exists up to 50 L.

The unusual behavior of the intensities of the two fifth-order spots can be interpreted as follows: Perhaps there is a phase transformation taking place, which influences the fifth-order spot intensities. As pointed out previously the $(1/5, 2/5)$ spot stands for the $(\sqrt{5} \times \sqrt{5})R27^\circ$ reconstruction. It may be that a prolonged exposure of oxygen will eventually convert the $p(5 \times 5)$ covered surface to the $(\sqrt{5} \times \sqrt{5})R27^\circ$ structure at 530 K. It is also possible that the $(\sqrt{5} \times \sqrt{5})R27^\circ$ structure is accessible only after another energy barrier is overcome or that this phase is stabilized at elevated temperatures. We will provide evidence later showing that it is not the coverage nor the activation barrier which determines the transformation from $p(5 \times 5)$

to $(\sqrt{5} \times \sqrt{5})R27^\circ$ structure, rather, it is the temperature-dependent free energy which stabilizes the formation of the $(\sqrt{5} \times \sqrt{5})R27^\circ$ reconstruction.

The FWHM of these spots are shown in Fig. 3c. The initial p(5x5) domains are already appreciably large when they start to be observed at this temperature. They are bigger than those at 400 K and 500 K. This can be understood if we follow the adsorption process isothermally along 530 K (cf. Fig. 1). Just before we pass the (2x2) region and meet the p(5x5) and c(2x2) mixture, the local density of the (2x2) structure is very high which means that the surface is mostly covered by c(2x2) domains; consequently, the p(5x5) reconstruction can be easily created. To further confirm this argument, a knowledge of the precise coverage information is needed. However, as mentioned earlier, due to bulk dissolution, it is not possible to obtain very accurate coverage values at this temperature.

The average p(5x5) domain size shown in Fig. 3c at saturation (20 L) is bigger than that at 400 K and 500 K at saturation. From a thermodynamical point of view, high temperatures favor the reconstruction to occur. At 530 K, which is 130 K above 400 K, once the requirement of the minimum nucleus size is met, the p(5x5) structure will rapidly grow to some maximum size. Again, we think that this is due to the "high temperature effect" which removes domain boundaries between the p(5x5).

5. Adsorption at 570 K

Figure 2e shows adsorption at this temperature where a completely new scheme develops as exposure reaches 13 L. First, we note that the intensity of the $(0, 1/2)$ spot drops to almost zero at about 7 L of exposure. Second, the $p(5 \times 5)$ pattern has a very short lifetime as is seen by the rapid vanishing of the $(1/5, 1/5)$ spot. Third, the other fifth-order spot, $(1/5, 2/5)$, grows uniquely despite the dramatic changes of others. This $(1/5, 2/5)$ spot represents a new structure which has been identified as $(\sqrt{5} \times \sqrt{5})R27^\circ$ (11). Its structure is probably very similar to the (001) plane of bulk PdO. Again, this is only a tentative assignment which is based on the unit cell of the observed LEED pattern. The ideal coverage for this structure is 0.8 monolayers, if indeed it is similar to the (001) plane of bulk PdO.

Figure 2e also indicates that the $(1/5, 2/5)$ spot intensity increases as coverage goes up, whereas the corresponding domain size, reflected in the spot profile FWHM of Fig. 3d, does not change very much. This is perhaps because the onset of desorption and bulk dissolution limits the growth of large size $(\sqrt{5} \times \sqrt{5})R27^\circ$ domains.

6. Adsorption at 600 K

Adsorption of oxygen at this temperature forms only the (2×2) structure on the surface. This is shown in Fig. 2f. No signs of the $p(5 \times 5)$ or $(\sqrt{5} \times \sqrt{5})R27^\circ$ reconstructions can be observed in the LEED pattern. The half-order spots look very much like those at 300 K. The thermal desorption spectra following various exposures at this

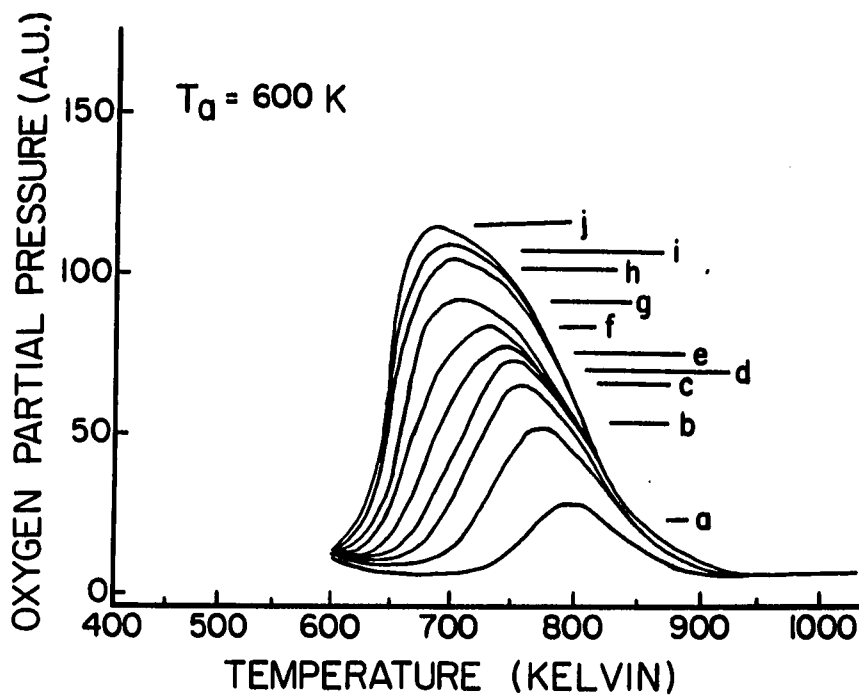


Figure 6. Thermal desorption spectra of oxygen on Pd(100) following oxygen adsorption at 600 K. The heating rate is 1 K/s. The exposure for each curve is (a) 0.5 L (b) 0.6 L (c) 0.8 L (d) 1.0 L (e) 2.0 L (f) 4.0 L (g) 8.0 L (h) 15 L (i) 30 L (j) 60 L.

temperature are shown in Fig. 6. After 100 L of exposure, we pump out the oxygen gas, desorb the chemisorbed oxygen in a typical thermal desorption experiment, and examine the surface by AES and LEED. The surface is visually shiny and LEED reveals a (1x1) Pd(100) substrate pattern with a high background intensity at room temperature. AES shows a shift in oxygen signal from 511 eV, the chemisorbed oxygen on the Pd(100) surface, to 505 eV. The shape and energy shift of the oxygen 511 eV KVV Auger transition have been used by other authors to identify the chemical properties of adsorbed oxygen on metal surfaces (23). The 6 eV energy shift observed in our AES result indicates that the surface is covered by oxygen which has different chemical properties than chemisorbed oxygen. When the sample is cooled to LN₂ temperature a c(2x2) LEED pattern with high background intensity appears. This c(2x2) structure is very inert toward reaction with CO and it can not be destroyed by annealing the sample at high temperatures (above 1200 K). Since this c(2x2) is formed after the sample is treated by oxygen at high temperatures we will name it the high temperature c(2x2) in order to distinguish it from the chemisorbed c(2x2). As we increase the sample temperature from LN₂ to room temperature, this high temperature c(2x2) structure disappears, but the AES 505 eV transition remains intact. In Fig. 7 we show the (1/2, 1/2) spot intensity of this high temperature c(2x2) structure as a function of temperature. It is clearly seen that the high temperature c(2x2) disappears at T ~ 300 K and reappears at low temperatures. This transition is completely reversible between 80 K and 300 K. We also perform experiments that

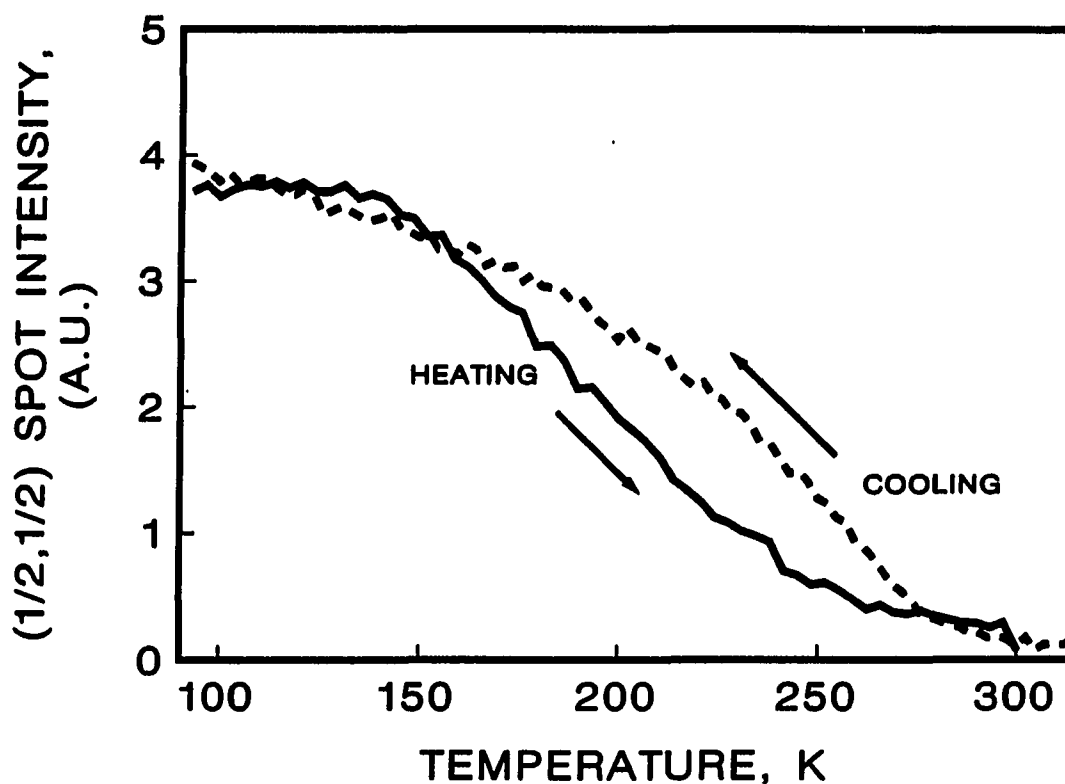


Figure 7. The intensity changes of the (1/2, 1/2) spot formed after high temperature treatments by oxygen as a function of temperature. The heating rate used is 1.2 K/sec and the cooling rate is 0.9 K/s. The small hysteresis which appears is probably due to the difference in heating and cooling rates. The beam energy is 64 eV.

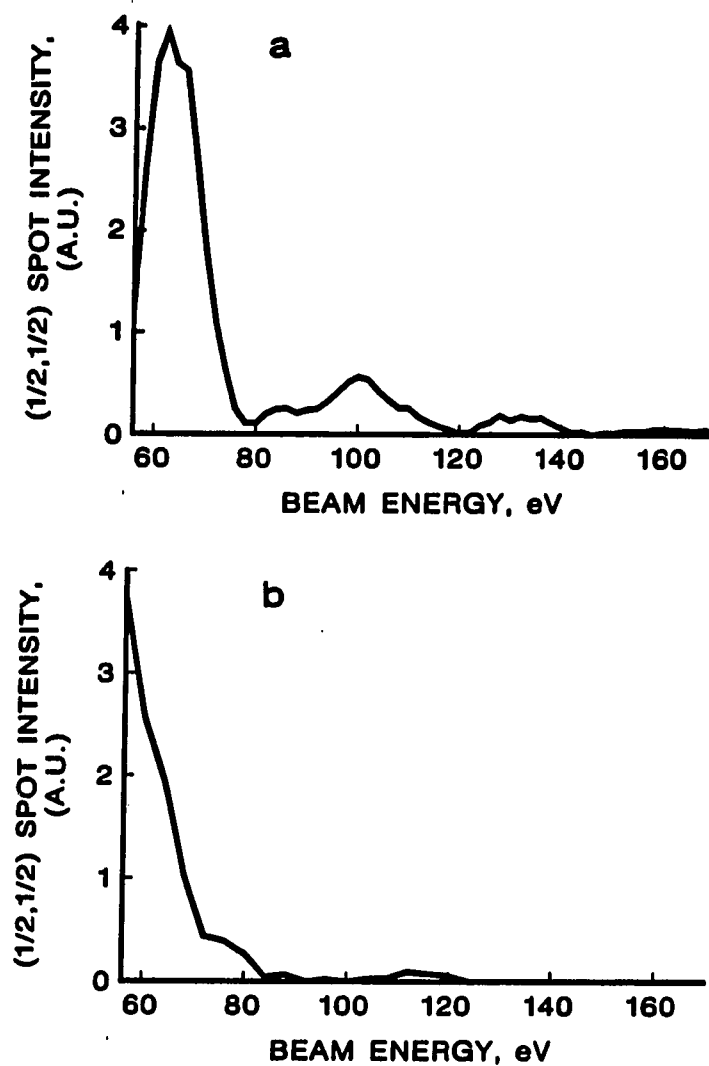


Figure 8. (1/2, 1/2) spot intensity vs. beam energy plot. Spectra are taken at LN_2 temperature.

- a) $c(2 \times 2)$ pattern formed after 50 Langmuirs of exposure to oxygen at room temperature.
- b) $c(2 \times 2)$ formed after high temperature treatments by oxygen.

monitor the changes in intensity of the $(1/2, 1/2)$ spot of the high temperature $c(2 \times 2)$ as a function of beam energy. This result is shown in Fig. 8b. In Fig. 8a, we show the changes of the $(1/2, 1/2)$ spot of a chemisorbed $c(2 \times 2)$ structure for comparison. According to Fig. 8b, this high temperature $c(2 \times 2)$ can only be observed between beam energies of 22 eV and 80 eV, and it vanishes completely as the beam energy passes beyond 80 eV.

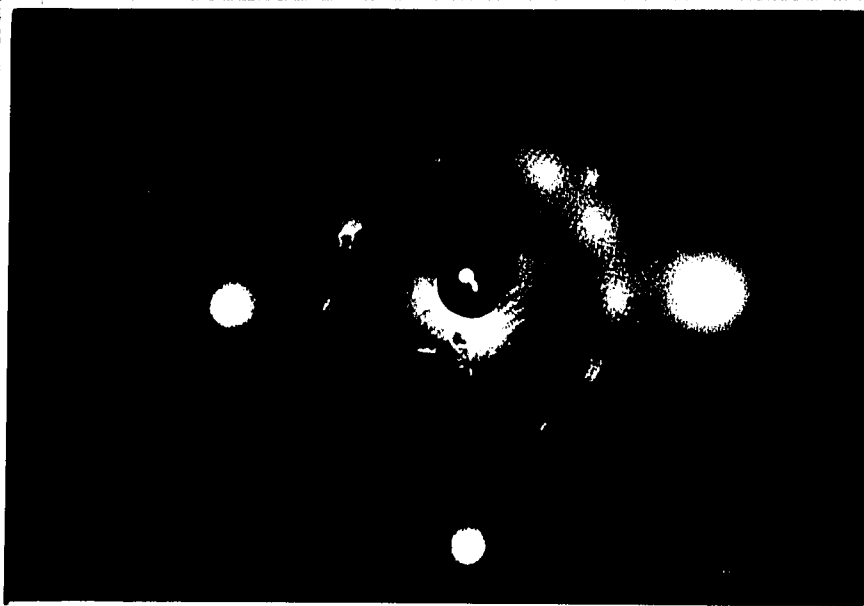
During the process of varying the beam energy, we observe another interesting structure which shows a ring-like LEED pattern. This pattern can only be seen at certain beam energies and does not disappear at high temperatures. Since the high temperature $c(2 \times 2)$ vanishes at high temperatures, it is reasonable to relate the AES 505 eV transition to this ring-like structure rather than to the high temperature $c(2 \times 2)$ structure. In Figs. 9a-c, we show the ring-like LEED pattern at three different beam energies, 55 eV, 105 eV and 135 eV, respectively. Figure 9a clearly shows that this ring-like pattern actually consists of two hexagonal domains superimposed on the high temperature $c(2 \times 2)$ structure. As the beam energy increases from 55 eV, the ring-like pattern disappears and then reappears only at 105 eV and 135 eV. At 105 eV, the high temperature $c(2 \times 2)$ disappears and streaks between the ring-like pattern are seen. At 135 eV, the streaks and the hexagonal patterns are very intense.

The high temperature $c(2 \times 2)$ and the ring-like structure have a very different properties than the ordered adlayers formed at temperatures below 600 K. It is informative to compare our results with others. A

Figure 9. The ring-like oxide pattern at various beam energies

- a) At 55 eV. The c(2x2) and dual-hexagonal structure are clearly resolved.
- b) At 105 eV. Two rings can be observed. The c(2x2) pattern can hardly be seen at this energy. The larger ring passes through the outer circumference of the first order integral spot indicating that the lattice constant of this structure is smaller than 5.5 Å but larger than 2.75 Å.
- c) At 135 eV. The inner ring becomes too weak to be seen. The outer ring gets too bright to distinguish the hexagonal pattern.

a



b

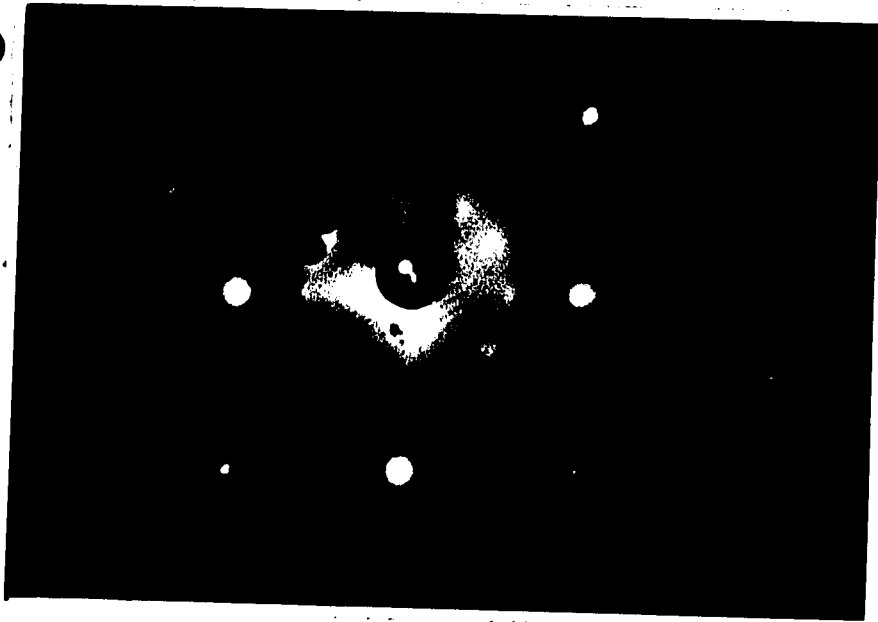




Figure 9 continues.

c(2x2) pattern is observed following adsorption at high temperature in other systems as well. Ducros and Merrill (24) treat a Pt(110) surface with oxygen ($P_{O_2} = (2 \sim 5) \times 10^{-8}$ Torr) at 800°C and see a c(2x2) pattern which transforms to a more complex structure, (3 x 12), as oxygen coverage increases. Conrad et al. (25) observe a sharp (2x2) structure on a Pd(111) surface after a similar high temperature adsorption of oxygen (900 K, $P_{O_2} = 5 \times 10^{-6}$ Torr). Both groups postulate that this c(2x2) is a transition state which exists between the chemisorbed layer and an epitaxial three-dimensional surface oxide. It is interesting to note that the bulk oxide structures for both Pt and Pd metals are identical (26). This tetrahedral oxide structure shown in Fig. 10 has the following dimensions: 5.34 x 3.05 x 3.05 Å (27). The distance between two adjacent atoms in Pd and Pt metals is 2.75 Å and 2.77 Å, respectively. These values are about one half the length of the long axis (5.34 Å) in the oxide. According to Fig. 10, the dimension of the (100) plane of bulk oxide is 5.34 x 3.05 Å. Therefore, Conrad et al. propose that the (100) plane of the bulk oxide forms on the Pd(111) surface to give the (2x2) LEED pattern (25).

The ring-like LEED pattern is observed on the Pd(111) surface by Conrad et al. (25) as well. They claim that it is caused by the growth of an epitaxial PdO layer on the Pd(111) surface. They propose a real space structure based on the PdO(100) plane superimposed on the Pd(111) surface. Ducros and Merrill [24] use the same (100) plane in PtO to construct a structure to elucidate their oxide which has a (3 x 12) LEED pattern on the Pt(110) surface. Based on Fig. 9, we can express our

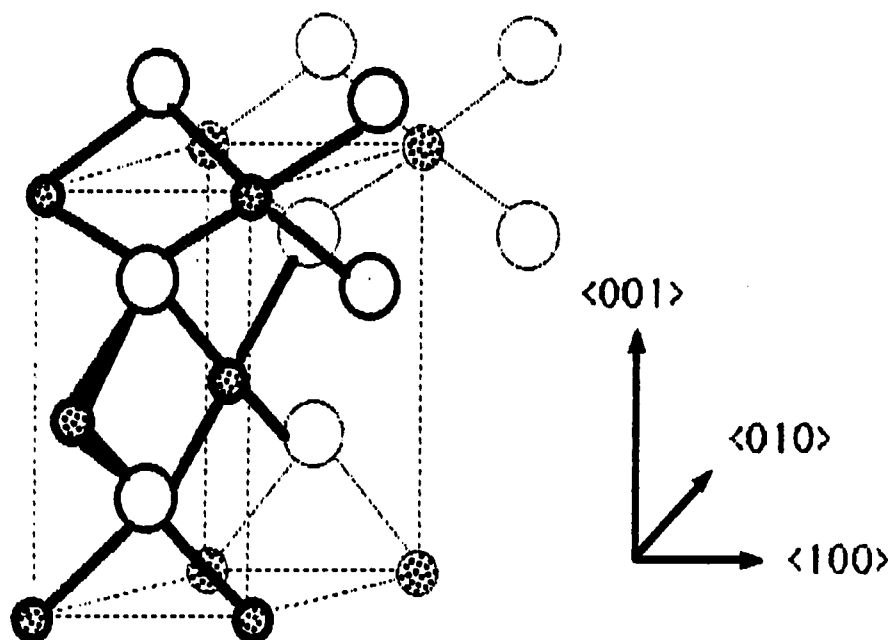


Figure 10. Oxide structure of both Pd and Pt metals (26). The small, shaded balls represent metal atoms. The big, hollow balls represent oxygen. The long axis has a dimension of 5.34 Å and the dimension for the short axis is 3.05 Å.

ring-like adlayer unit cell as $\begin{pmatrix} 3/2 & \sqrt{3}/2 \\ 3/2 & -\sqrt{3}/2 \end{pmatrix}$ in matrix notation. This non-orthogonal matrix implies that the angle between the adlayer lattice vectors is not identical to the angle between the substrate lattice vectors. If this is the case, then there is no simple low-index plane in bulk PdO which can be used to fit the observed ring structure in our experiment.

If this ring-like LEED pattern is related to the bulk oxides then it is puzzling that such surface oxides are stable at high temperatures without decomposition in vacuo. According to thermodynamic data (28,29), the equilibrium oxygen pressure for the reaction $2\text{PdO}_{(s)} \rightleftharpoons 2\text{Pd}_{(s)} + \text{O}_{2(g)}$ at 1000 K is about 250 Torr (28). As a result, the dissociation oxygen pressure of the oxide is large enough to drive the reaction to remove the oxide phase at high temperatures. The unusual stability of surface oxides has been a subject of controversy (30-33). In order to properly explain what is observed in experiments, several models have been proposed. Campbell et al. (30) think a nonstoichiometric solid solution of oxygen exists in the Pd subsurface region. Peuckert (31) concludes from his XPS studies that some small clusters of Pd metal are imbedded in the oxide matrix. Bader et al. (32) reach a result which points toward the formation of an extrinsic Si-stabilized oxide species which gives a ring-like LEED pattern from the surface, based on their AES and XPS experiments.

Our results show that the high temperature c(2x2) and the ring-like hexagonal pattern might be somewhat related to bulk PdO. According to the LEED pattern shown in Fig. 9, we calculate the lattice constant for

the ring-like pattern and obtain a value which is $4.51 \pm 0.07 \text{ \AA}$. This value is close to the value $4.6 \pm 0.1 \text{ \AA}$, reported by Bader et al. (32). However, we do not observe an enhancement of the AES transition at energy 78 eV as is pointed out by these authors (32,33). The 78 eV enhancement signals the formation of SiO_2 , which stabilizes the oxygen in this metal.

The fact that streaks appear in the ring-like LEED pattern is probably due to the formation of polycrystalline PdO facets on the surface. This polycrystalline PdO might be a azimuthally random, yet preferentially expose a low index plane of bulk PdO at the surface, and it could be microscopically rough. After high temperature treatment of the sample with oxygen, the $c(2 \times 2)$ pattern is still seen and superimposed on the ring-like pattern at 300 K and below as shown in Fig. 9a. This is probably because there is only a thin layer of the polycrystalline PdO on the surface. From Fig. 9a we can also tell that this high temperature $c(2 \times 2)$ structure does not show any streaks, which implies that the $c(2 \times 2)$ forms on top of the Pd(100) metal not on top of the PdO. Based on the LEED observations we propose a model to illustrate the relationship between the high temperature $c(2 \times 2)$ and the ring-like structure in Fig. 11. After the sample is treated by oxygen at high temperatures, a place-exchange reaction (34) between oxygen and Pd atoms might occur (Fig. 11a) and result in the formation of a thin layer of a low index polycrystalline PdO plane which shows a ring-like LEED pattern (Fig. 11b). As the sample is cooled to LN_2 temperature, the $c(2 \times 2)$ reappears on the Pd(100) surface (Fig. 11c). According to

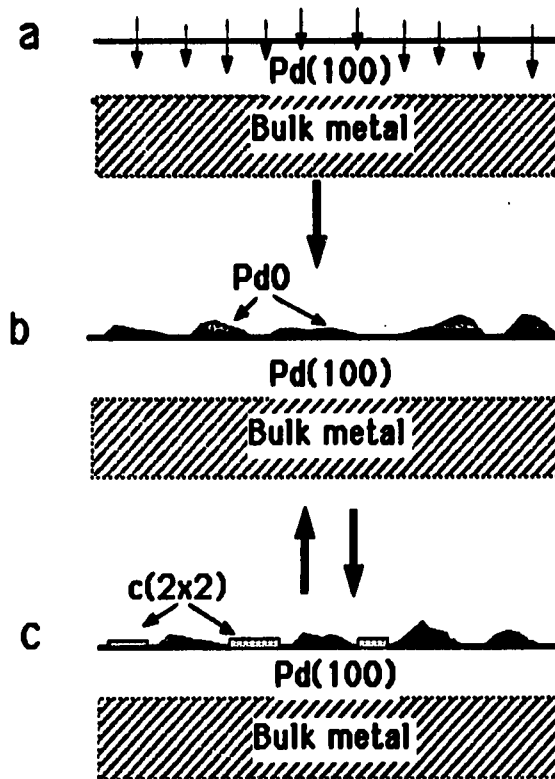


Figure 11. Proposed mechanism of forming the high temperature $c(2 \times 2)$ and the ring-like patterns.

- a) Adsorption of oxygen at high temperature makes the place-exchange reaction between oxygen and Pd atoms possible.
- b) Microcrystalline PdO covering the surface gives the ring-like LEED pattern.
- c) As temperature decreases, the $c(2 \times 2)$ structure reappears on top of the surface, thus both the ring-like pattern and $c(2 \times 2)$ pattern are observed. According to our results, (b) and (c) are reversible.

our data (cf. Fig. 7), the changes between Fig. 11b and Fig. 11c are reversible.

It is interesting to note from our result that formation of the ring-like "surface oxide" at this adsorption temperature prevents the fifth-order spots from appearing. This is probably because the formation of the polycrystalline PdO at this temperature does not allow the nuclei for the $p(5 \times 5)$ and $(\sqrt{5} \times \sqrt{5})R27^\circ$ reconstructions to form.

B. The Reversibility of Phase Transitions Between Ordered Adlayers

The phase diagram shown in Fig. 1 has many different regions separated by boundaries. In order to prove that the transitions between these phases are reversible when crossing the boundaries, we first adsorb oxygen at 300 K or 400 K to form particular phases, then the heating and cooling experiments are carried out. In each experiment, we cycle the entire process three times to remove the kinetic limitations which might occur due to insufficient mobility of oxygen atoms at low temperatures (35). Those areas that are chosen to examine the reversibility of phase transition are connected by double-headed arrows in Fig. 1. The detailed experimental results are shown in Fig. 12 in which the LEED spot intensity changes are plotted as a function of time. In Fig. 13, we plot out a typical curve for the temperature variation as a function of time. Based on this curve, we put the temperature value on the top axis of Fig. 12. The average heating rate used is 0.9 K/s and the cooling rate is 6.3 K/s.

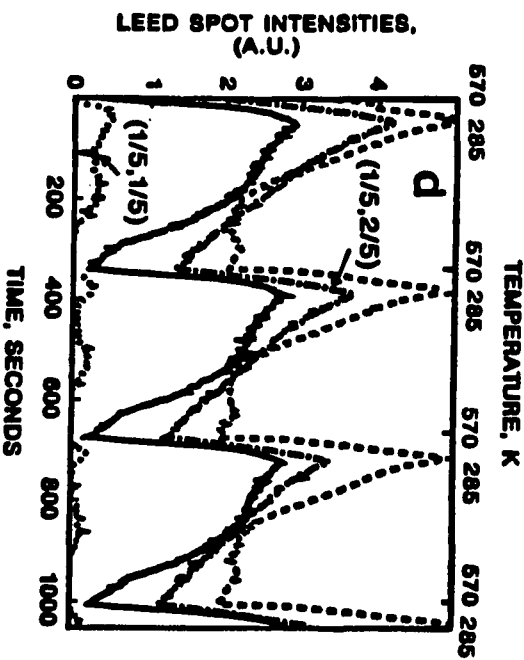
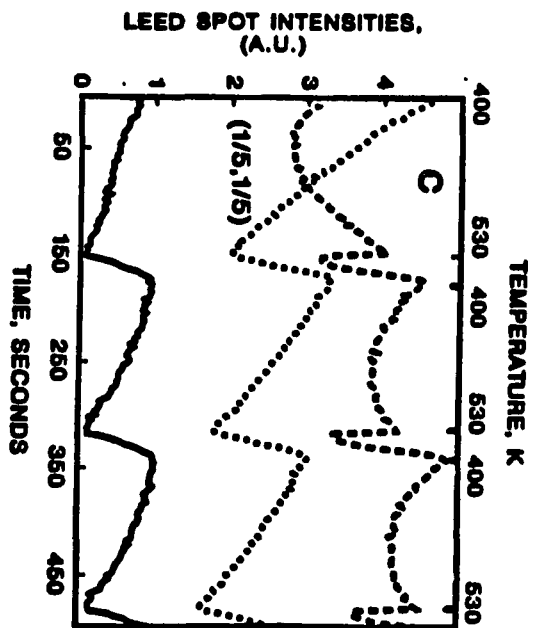
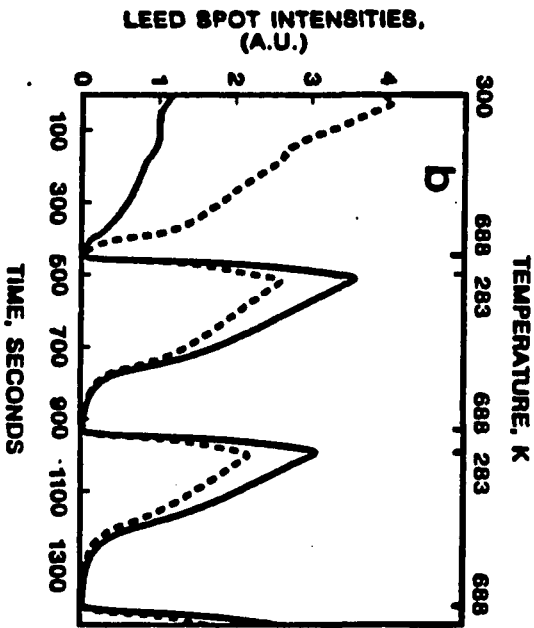
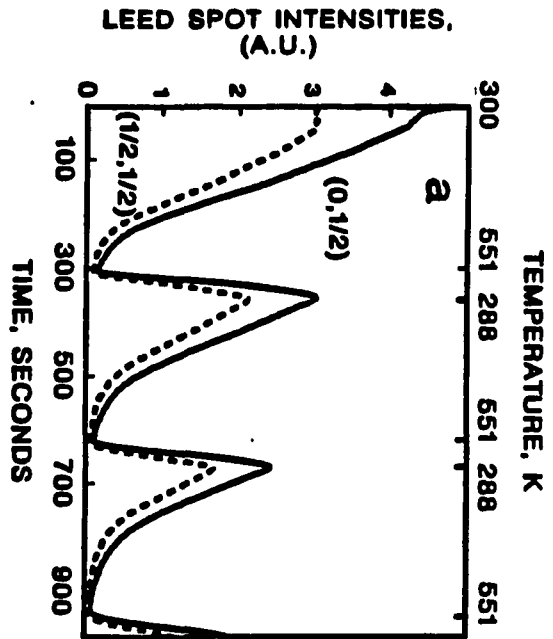
Figure 12. Reversibility of phase transitions between ordered adlayers

a) Initial coverage 0.20 monolayers

b) Initial coverage 0.32 monolayers

c) Initial coverage 0.50 monolayers

d) Initial coverage between 0.50 and 0.56 monolayers. The corresponding ordered adlayers on the surface at each coverage can be deduced from Fig. 1.



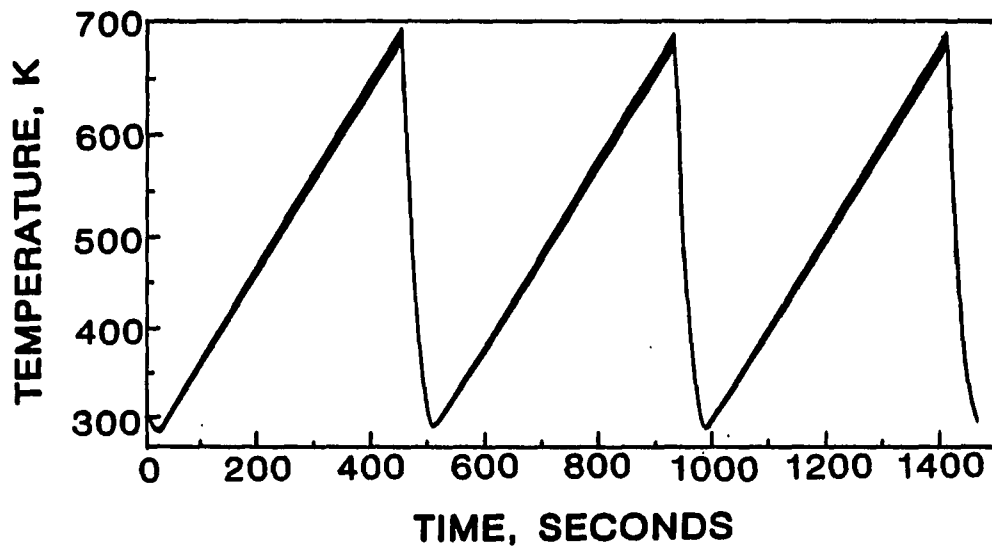


Figure 13. Temperature program used in Fig. 12. In this example the heating rate is 0.9 K/s, and the cooling rate is 6.3 K/s.

1. Initial coverage 0.20 monolayers

According to Fig. 12, the surface is covered primarily by the $p(2 \times 2)$ structure at this coverage. Both the intensities of the $(1/2, 1/2)$ and $(0, 1/2)$ spots decrease rapidly upon heating and eventually disappear at 550 K as shown in Fig. 12. Both spots can be restored when the sample is cooled; however, the maximum intensities only reach two-thirds of their original values. This could be due to the fast cooling rate that kinetically limits the domain growth on the surface. Of course, dissolution of oxygen into the bulk might also play an important role in effecting the intensities. Nevertheless, Fig. 12 shows that the ordered structures which initially exist on the surface can be obtained again after disordering. This result implies that we have an order-disorder phase transition at this coverage.

2. Initial coverage 0.32 monolayers

As coverage increases from 0.2 monolayers to 0.32 monolayers, the $c(2 \times 2)$ structure becomes more and more predominant on the surface. This is seen by the intensified $(1/2, 1/2)$ spot intensity shown in Fig. 12b. When the sample is heated to 690 K, all spots disappear. This temperature is higher than the desorption temperature; as a result, coverage falls, and when the sample is cooled again the intensity of the $(0, 1/2)$ spot becomes stronger than that of the $(1/2, 1/2)$ spot. These intensity changes reflect an increase in the amount of $p(2 \times 2)$ relative to $c(2 \times 2)$, as coverage falls. Despite the variations in intensity

(coverage), we still retrieve ordered structures, at least partially, after cycling three times.

3. Initial coverage 0.50 monolayers

There are $p(5 \times 5)$ and (2×2) structures coexisting on the surface initially. Based on Fig. 1, the phase rule indicates that there is more $p(5 \times 5)$ than (2×2) structure at this coverage. This is reflected in Fig. 12c, where the $(1/5, 1/5)$ spot intensity is higher than that of the half-order spots. When heating starts, the $p(2 \times 2)$ structure disappears at 530 K. At this temperature the surface is covered by $p(5 \times 5)$ and $c(2 \times 2)$ only. Note that during the process of heating, the $(1/2, 1/2)$ spot intensity decreases initially and then increases as temperature rises. We believe that this is due to the presence of the $p(5 \times 5)$ structure which undergoes continuous conversion to the $c(2 \times 2)$ structure. As temperature decreases during cooling, the $p(5 \times 5)$ and the (2×2) structure reappear which confirms the reversibility of the phase transition between the $(2 \times 2) + p(5 \times 5)$ and the $c(2 \times 2) + p(5 \times 5)$ regions.

4. Initial coverage between 0.50 monolayers and 0.56 monolayers

The last thing that we test is the reversibility between regions labelled $c(2 \times 2) + (\sqrt{5} + \sqrt{5})R27^\circ$ and $p(5 \times 5) + c(2 \times 2)$ shown in Fig. 1. Since the $(\sqrt{5} \times \sqrt{5})R27^\circ$ structure is formed at temperatures above the onset of desorption which is about 570 K, there is no way we know the coverage value. In addition, we want to minimize the coverage variations during the experiment; therefore, we adsorb oxygen at 570 K

first to form the $c(2 \times 2)$ and $(\sqrt{5} \times \sqrt{5}) R27^\circ$ structures and then lower the temperature to the region where $p(5 \times 5)$ and (2×2) structures appear. This result is shown in Fig. 12d. The reappearance of the $p(5 \times 5)$ is signaled by the emergence of the $(1/5, 1/5)$ spot as the sample is cooled. We still repeat the cycling three times. Each time the half-order spots are able to recover their intensities, but the intensities for the fifth-order spots decrease gradually. We believe that at this temperature the kinetic limitations have been removed; therefore, all spots should return to the original intensities as long as the phase transition is reversible and as long as coverage remains constant. The continuous decrease in the maximum values of the fifth-order spot intensities is due to the fact that the coverage decreases due to desorption and dissolution.

Based on this result, we prove that the phase transition between $p(5 \times 5)$ and $(\sqrt{5} \times \sqrt{5})R27^\circ$ structures is reversible. By closely examining the structures of $p(5 \times 5)$ and $(\sqrt{5} \times \sqrt{5})R27^\circ$ (9,11), we see that the ratio between oxygen and Pd atoms in PdO is identical for both reconstructed structures, but the superlattice unit cell is larger for the $p(5 \times 5)$ than that of the $(\sqrt{5} \times \sqrt{5})R27^\circ$ with respect to the substrate Pd(100). Note that coverage, however, is defined as the ratio of oxygen atoms to Pd atoms in a perfect Pd(100) surface, rather than to Pd atoms in the reconstruction. Therefore, the $(\sqrt{5} \times \sqrt{5})R27^\circ$ structure has a coverage which is about 25% higher than the $p(5 \times 5)$ structure, in spite of the identical ratio of oxygen to Pd atoms in the reconstructed surface. Therefore, it is possible that decreasing in the $p(5 \times 5)$ domain size

causes the local density of oxygen to increase and forms the $(\sqrt{5} \times \sqrt{5})R27^\circ$ structure. The concept of changes in coverage caused by changes in the domain size might help to understand why the phase transition between the two reconstructed structures is reversible. The observed reversibility rules out the possibility that there is a significant activation energy barrier between these two reconstructed phases.

IV. DISCUSSION AND SUMMARY

We have constructed a phase diagram based primarily on our LEED observations for the system O/Pd(100). In order to assure that Fig. 1 represents a phase diagram which is thermodynamically allowed, we experimentally walk through Fig. 1 in both horizontal and vertical directions. The results indicate that all the phases separated by boundaries are in equilibrium. Furthermore, a true phase diagram has to fulfill the Gibbs phase rule which defines the number of degrees of freedom in the system. For example, a two-component, two-phase system will have two degrees of freedom. If we apply this rule to our phase diagram then the region labelled $p(5 \times 5) + (2 \times 2)$ in Fig. 1 has two degrees of freedom since it encompasses a non-zero area of the θ -T plane, and it has two components: Pd and oxygen. Therefore, there can only be two phases. (The oxygen gas phase and Pd phase are presumed ignorable.) As a result, the (2×2) can only be a single phase, otherwise, the regions labelled by $(2 \times 2) + p(5 \times 5)$ will violate the phase rule by having too many phases.

A similar system to the present one is O/Ni(100) studied by Taylor and Park (36). They map out the temperature-coverage phase diagram in the range between 0.0 and 0.5 monolayers from 300 K to 900 K. A coexistence region with both $p(2 \times 2)$ and $c(2 \times 2)$ structures is shown in their phase diagram. In Fig. 1, we label our phase diagram where the coverage is between 0.15 and 0.30 monolayers a single (2×2) phase instead of two phases. This is saying that we cannot distinguish

whether there are two separated phases of $p(2 \times 2)$ and $c(2 \times 2)$ growing sequentially as coverage increases or if there is only one mixed, interpenetrating phase of both $p(2 \times 2)$ and $c(2 \times 2)$. We believe that a single mixed phase is more plausible based on the following reason. If there are two separated phases then as the coverage approaches $1/2$ monolayers a drastic change on average island size should be observed due to the coalescence of small domains to form large $c(2 \times 2)$ domains which implies the appearance of a distinct singularity in the spot profile vs. coverage plot. We do not observe this change in Fig. 3. We can only define this (2×2) structure, at this stage, as a single phase whose density varies continuously as coverage increases.

There is no activation energy barrier between the $p(5 \times 5)$ and $(\sqrt{5} \times \sqrt{5})R27^\circ$ reconstructions because the phase transition between them is reversible. Therefore, the total free energy (which varies with temperature) is the factor that determines which phases exist at fixed coverage, i.e., at 400 K the $p(5 \times 5)$ structure is formed, and at 570 K the $(\sqrt{5} \times \sqrt{5})R27^\circ$ structure. There is, however, an activation barrier between the ring-like structure and the two reconstructions. If this ring-like structure can be related to bulk oxide (100) plane then it is reasonable to postulate that a particular orientation of the PdO is stabilized on the Pd(100) surface at different temperatures.

In summary, we show a complete phase diagram which covers all the ordered phases formed by oxygen on the Pd(100) surface. Based on all the tests we perform in this paper we believe that Fig. 1 represents a true phase diagram of this system.

V. ACKNOWLEDGEMENTS

This work is supported by the Director for Energy Research, Office of Basic Energy Sciences. Ames Laboratory is operated for the U.S. Department of Energy by Iowa State University under contract No. W-7405-ENG-82.

VI. REFERENCES

1. D. P. Woodruff, G.-C. Wang and T.-M. Lu, "Surface Structure and Order-Disorder Phenomena," in The Chemical Physics of Solid Surface and Heterogeneous Catalysis, Vol. 2, Ed. D. A. King and D. P. Woodruff, Elsevier, Amsterdam (1983) p. 327.
2. W. H. Weinberg, *Am. Rev. Phys. Chem.* 34 (1983) 217.
3. A. R. Kortan and R. L. Park, *Phys. Rev. B*, 23 (1981) 6340.
4. R. J. Behm, K. Christmann, and G. Ertl, *Solid State Commun.* 25 (1978) 763. E. Domany and M. Schick, *Solid State Commun.* 30 (1979) 331.
5. S. M. Foiles and M. S. Daw, *J. Vacuum Sci. Technol.* A3 (1985) 1565.
6. R. J. Behm, K. Christmann and G. Ertl, *Surf. Sci.* 99 (1980) 320.
7. G.-C. Wang, T.-M. Lu and M. G. Lagally, *J. Chem. Phys.* 69 (1978) 479.
8. R. A. Barker and P. J. Estrup, *J. Chem. Phys.* 74 (1981) 1442.
9. S.-L. Chang and P. A. Thiel, *J. Chem. Phys.* 88 (1988) 2071.
10. S.-L. Chang, P. A. Thiel and J. W. Evans, *Surf. Sci.* (1988) to be submitted.
11. T. W. Orent and S. D. Bader, *Surf. Sci.* 115 (1982) 323.
12. G. Ertl and J. Koch, *Z. Phys. Chem.* 69 (1970) 323.
13. E. M. Stuve, R. J. Madix and C. R. Brundle, *Surf. Sci.* 46 (1984) 155.

14. C. R. Brundle, R. J. Behm and J. A. Barker, *J. Vacuum Sci. Technol.* A2 (1984) 1038.
15. S.-L. Chang and P. A. Thiel, *Phys. Rev. Lett.* 59 (1987) 296.
16. M. A. Barteau, E. I. Ko and R. J. Madix, *Surf. Sci.* 102 (1981) 99.
17. M. Tringides, P. K. Wu, W. Moritz and M. G. Lagally, *Ber. Bunsenges. Phys. Chem.* 90 (1986) 277.
18. V. P. Zhdanov, *Surf. Sci.* 194 (1988) L100.
19. G.-C. Wang and T.-M. Lu, *Phys. Rev. Lett.* 50 (1983) 2014.
20. P. A. Thiel, J. T. Yates, Jr. and W. H. Weinberg, *Surf. Sci.* 82 (1979) 22.
21. K. Christmann, V. Penka, R. J. Behm, F. Chehab and G. Ertl, *Solid State Commun.* 51 (1984) 487.
22. R. J. Behm, G. Ertl and J. Wintterlin, *Ber. Bunsenges. Phys. Chem.* 90 (1986) 294.
23. P. Légaré, G. Maire, B. Carrière and J. P. Deville, *Surf. Sci.* 68 (1977) 348.
24. R. Ducros and R. P. Merrill, *Surf. Sci.* 55 (1976) 227.
25. H. Conrad, G. Ertl, J. Küppers and E. E. Latta, *Surf. Sci.* 65 (1977) 245.
26. A. F. Wells, "Structural Inorganic Chemistry" 5th ed. Clarendon Press, Oxford (1984) p. 539.
27. Jürg Waser, Henri A. Levy and S. W. Peterson, *Acta Crystallogr.* 6 (1953) 661.
28. J. S. Warner, *J. Electrochem. Soc.* 114 (1967) 68.
29. W. E. Bell, R. E. Inyard and M. Tagami, *J. Phys. Chem.* 70 (1966).

30. C. T. Campbell, D. C. Foyt and J. M. White, *J. Phys. Chem.* 81 (1977) 491.
31. M. Peuckert, *J. Phys. Chem.* 89 (1985) 2481.
32. S. D. Bader, L. Richter and T. W. Orent, *Surf. Sci.* 115 (1982) 501.
33. H. Niehus and G. Comsa, *Surf. Sci.* 102 (1981) L14.
34. F. P. Fehlner and N. F. Mott, *Oxid. of Metals* 2 (1970) 59.
35. S.-L. Chang and P. A. Thiel, Chem. Dept., Iowa State Univ., in preparation.
36. D. E. Taylor and R. L. Park, *Surf. Sci.* 125 (1983) L73.

APPENDIX: THE LEED PROGRAM

All the LEED data, including one-pixel width spot profiles and integrated spot intensities, reported in this dissertation are taken by a computer-interfaced video camera coupled with Varian four-grid LEED optics. The goals of this appendix are to introduce fundamental concepts about how the computer and video camera are interfaced in this laboratory and to provide guidelines about the LEED program for new users.

I. THE COMPUTER AND THE VIDEO INTERFACE

The computer interfaced to the video camera is a MICRO PDP-11/23, a product of Digital Electronic Co. (DEC). It has a 16-bit (16 bits = 2 bytes = 1 word) central processing unit (CPU), a floating point processing unit (FPU) and a maximum 4-megabyte memory capacity (1 Kbyte = 1024 bytes). The digitized video data are stored as 2 bytes integer numbers (1 integer = 1 word), and the maximum number which can be accepted is $2^{15} = 32,768$. There are three different locations to store files or experimental data: 1) The system hard disk (logical device name SY or DU0) in which several subdirectories are created and each has a different logical device name, i.e., LD0, LD1, LD2, LD3, LD4, and LD5. 2) Two removable floppy disks (logical device name DU1 and DU2) driven by a disk driver. 3) The virtual memory (logical device name VM or VM0). Note that all these memory spaces are counted in terms of BLOCKS (1 block = 256 words). Among these memory locations, the virtual memory is very unique and deserves more attention. It uses a random-access memory (RAM) which allows data to be transferred with high speed from memory to memory whereas other types of memories use low speed disk-to-memory transportation. By using this special property, data can be stored very fast although in this area during an experiment. After each experiment, the LEED program automatically transfers all data in the virtual memory (RAM disk) to a preassigned location to have those data stored permanently. However, one should always keep in mind that

the RAM disk is always initialized when the computer is rebooted. This means that data stored in this area will be lost if a power failure occurs.

The video camera (a product of DAGE-MTI Co.) is used to acquire video signals and has an Intensified Silicon Diode (ISD) tube. This video camera is interfaced to the computer through IP-512 imaging boards (a product of Imaging Technology Inc.). There are three major elements contained in the IP-512 family; i.e., AP-512, ALU-512, and FB-512 boards. Each performs a different task in processing the video signal. The main functions of these boards are listed below:

1) AP-512 (Analog Processor)

Provides digital to analog (D/A) or analog to digital (A/D) conversion of the incoming or outgoing video signals.

2) ALU-512 (Arithmetic Logic Unit)

Provides arithmetic manipulations of the digitized video data.

3) FB-512 (Frame Buffer)

Provides 512 by 512 by 8 bits high speed RAM video frame buffers in which digitized data can be stored and accessed by AP-512, ALU-512 and the CPU of the computer.

Figure 1 shows the block diagram of the configuration of the three video boards, which are usually referred to as an Imaging Processing Cluster, together with the computer CPU and the video camera. The digitized video signal is carried and passed to the Imaging Processing Cluster by the Video-Bus. The Q-Bus is used by the computer's CPU to access the

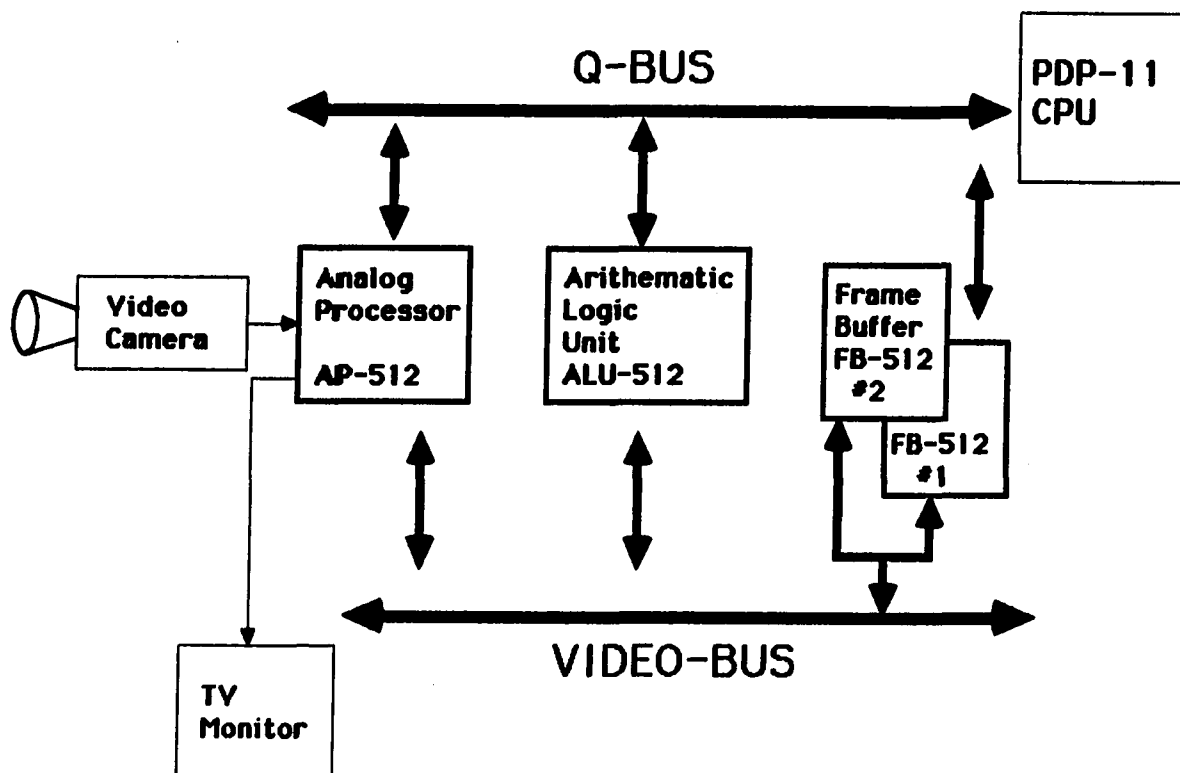


Figure 1. Block diagram of the IP-512 family, the computer CPU, and the video camera. The video signals are transferred between the IP-512 Video boards by a Video-Bus. The computer CPU accesses the video signals through a Q-Bus.

digitized video signals. The TV monitor displays the picture which is either stored in the frame buffer or is sent out directly by the video camera.

II. THE LEED PROGRAM

A. Program Highlights

The entire LEED program consists of many subroutines and files which are stored in various memory locations. All these subroutines and files are required to run the program. Figure 2 illustrates the distribution of these files. The file names are enclosed in rectangular boxes. On the top of these boxes are subdirectories in which files are stored. The arrows show the paths through which these files are directed.

All the Fortran source files and their compiled object files are stored in LDO. After all the object files are linked by issuing command LEEDLK.COM in LDO, a file named LEED.SAV is generated. This current LEED.SAV file should be copied to LD1. In VMO, a copy of the LEED.SAV file is duplicated from LD1 by executing the RLEED.COM file which is stored in LD1. The virtual memory which contains the LEED.SAV file then acts as a working disk to store and transfer data. After the LEED.SAV file is executed in VMO, it opens a new file SCTPRO.BIN with 3000 blocks of empty space to store experimental data. This SCTPRO.BIN is a scratch file meaning that old data stored in this location will be erased and written over by the newly acquired data. The program then reads parameters from the file LEEDCM.DEF or LEEDCM.DAT in DUO. Both the LEEDCM.DEF and LEEDCM.DAT files store parameters which are needed to run the LEED program. The primary difference between them is that the

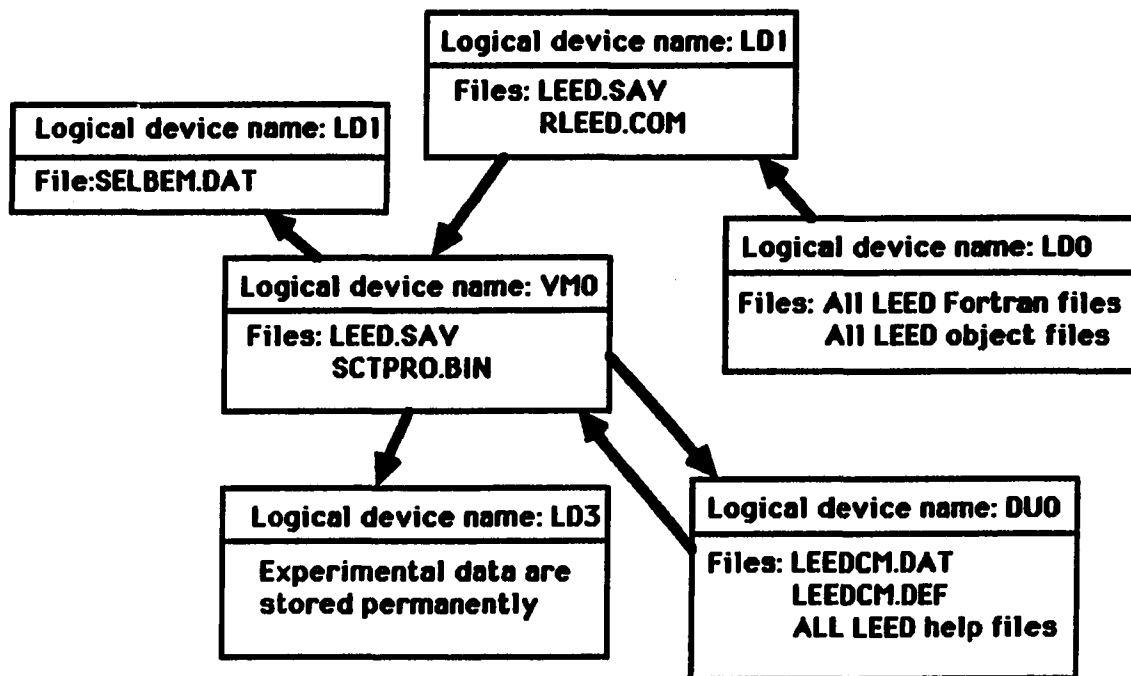


Figure 2. Allocations of all files that are associated with the LEED program. The figure shows the locations in which these files are stored. Arrows indicate the sequence in which these files are generated.

former contains default parameters and the latter contains current parameters. A detailed explanation about these files will be presented in Section IIB.

There are help files stored in DUO for the LEED program. These help files provide lists of commands used in the LEED program and their explanations. To read these help files, one needs to type "HE" after the LEED program is executed.

In LD1, there is a file named SELBEM.DAT which keeps all the current information of the selected windows. This file is created by the command "OP" in VIDCOM.FOR.

When an experiment is running, all acquired data are stored in SCTPRO.BIN at a maximum speed. After the experiment is finished, those data stored in file SCTPRO.BIN are transferred automatically to LD3 for permanent storage. Sometimes an error message shows a failure in transferring data from VMO:SCTPRO.BIN to LD3 due to insufficient disk spaces. It is important to know that this error does not destroy the current experimental data which have been stored in the file SCTPRO.BIN as long as the computer stays on. To recover the data from SCTPRO.BIN, one first needs to reset the file pointer to 1 by using command "RS" followed by using command "CO" and later choose "write" to transfer these data to another disk space. Even if the program terminates itself due to a severe error, the data in SCTPRO.BIN can still be transferred to other places. To do that, one has to reenter the LEED program by typing "RUN LEED" instead of "@RLEED" and then follow those steps described previously. The reason for using a different command is

because the "RUN LEED" command does not initialize the VMO; therefore, it preserves the contents stored in the file SCTPRO.BIN. Note that all the data taken by the LEED program are stored in binary form (i.e., they can not be displayed on the terminal) which takes less memory space and thus maximizes the storage capacity of data points. The program allows 750 data points to be taken and each data point can have 10 windows.

Although the majority of the LEED program is written in Fortran language, some of the subroutines are written in assembly language for the purpose of fast processing. These subroutines are used to drive the three IP-512 imaging boards and are incorporated in the LEED program. A detailed description of these routines are documented by Imaging Technology Inc. A copy of this document is kept in room 222 of Spedding Hall.

The Fortran coded LEED program is composed of many subroutines which are called by the root program LEEDRT through different commands. Figure 3 shows all the subroutines and how they are called by the root program. In each rectangular box, a program's name is listed on the top half followed by subroutines on the bottom. Arrows outside the boxes point to the corresponding subroutines which are called by the commands indicated. Although these arrows are drawn as one-way paths, the actual subroutine calls are two way processes. Note that there are three shaded boxes which contain three important programs: LEED, VIDCOM, and DATMNP. We briefly describe their functions as follows:

LEED: The root that establishes the entire program.

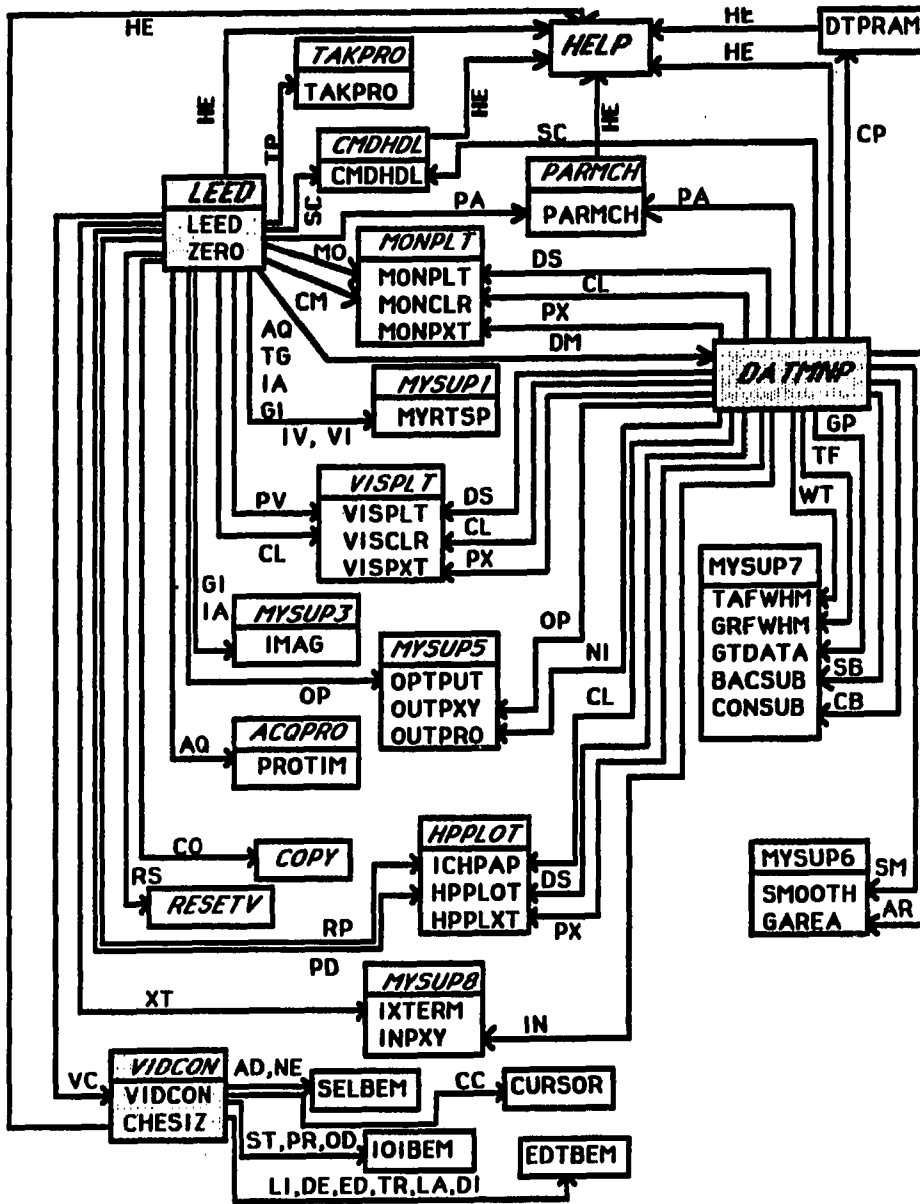


Figure 3. Subroutines and commands involved in the LEED program. The shaded areas indicate files that are of greatest importance and most frequently used.

VIDCOM: The program that allows windows of interesting spots to be selected.

DATMNP: The program that manipulates the experimental data after they are acquired.

A detailed explanation of all other subroutines can be found in the LEED documentation which is a copy of the output of the LEED program located in room 222 of Spedding Hall.

Due to the large size of the program, it is not possible to fit the entire program in the available memory space (PDP-11 allows 64K bytes in the memory to store programs); therefore, the program is linked by using "overlays". The characteristics and advantages of using the overlay can be found in the RT-11 System Utilities Manual. The overlay structure is shown in the following:

Root Program	Overlay 1	Overlay 2	Overlay 3	Overlay 4
LEEDRT	SAVCOM	PARMCH	MYSUP7	MYSUP2
MYSUP	VIDCON	DTPRAM	SELDRT	LDHELP
ITALIB	DATMNP	VISPLT	CURSOR	MYSUP6
SYSLIB	LOADAT	MONPLT	IOIBEM	MYSUP8
	TAKPRO	SELBEM	ACQPRO	COPY
		EDTBEM	CMDHDL	RESETV
		MYSUP3	HPLOT	MYSUP1
		MYSUP5		

B. Transportation of Parameters

Many parameters are passed between subroutines in this program. In order to transfer these parameters efficiently, COMMON BLOCKS are used. A common block is always stated at the beginning of a program and is defined as follows: /NAME/ parameter1, parameter2, parameter3; etc. Name is the fixed title of this common block and the parameters that follow are used to carry information. The symbols of parameters used in a common block can be different in different programs. However, the relative positions of these parameters should always be kept the same. The way that common blocks work is that the information carried by parameters in a common block is passed to the program. This information can also be carried and transported by common blocks to another program in which common blocks with identical names are defined. This way the information carried by the parameters in the common block can be used by the latter program directly without repeating the calculations.

The LEED program stores all the essential parameters in a file named LEEDCM.DEF. This file is generated by the program SAVCOM.FOR, which also loads the information in LEEDCM.DEF to the LEED program. The current experimental parameters can be stored by the SAVCOM.FOR into file LEEDCM.DAT if the LEED program is terminated normally. Upon starting, the LEED program first loads all the parameters automatically, then the common blocks pass these parameters to other subroutines. The important point to note here is that the parameter files (i.e., LEEDCM.DEF and LEEDCM.DAT) should have exactly the same format as those created by SAVCOM.FOR. All the common blocks used in this program are

listed below. Explanations for all the parameters carried by common blocks and their default values can be found in the LEED documentation.

```

COMMON/PARM/NSLE,NSLO,NSIG,NSUB,NSTOR,IBAC,IARE
COMMON/VPARM/YSTP(10),IXSTP(10),NIB,IXWID,IVNP,IVOF
COMMON/MNPLTC/IBCLOR,IZCLOR,INST,IMOF
COMMON/HPARAM/IUD,IPN,IHPS,IHPT,IFB,LIB,ICV,IHOF
COMMON/VDATA/IHP(1000),DPRAM(5)
COMMON/VTBUF/VTBF,VTPOS,VTBFF
COMMON/CRMOV/CURM,IXC,IYC
COMMON/BLK2/IOPGE,ICSRTT
COMMON/BLK3/STOPN,STOPL
COMMON/BLK1/BLABEL,IBE,IB,ISPN
COMMON/PROF/IXM,IYM,IHH,IHW,IET,IHVL(128),IVVL(128)
COMMON/PROFL/IFL,NTI,TMPROF,IPFL,IEXP,IFILE
COMMON/NAMEC/NAME,NAMTM
COMMON/SAVCM/IMXREC,IFIFL,ILIFL
COMMON/COMMAND/COMD,BEEP,VCOMD,DMPCOM,COML,COMB
COMMON/CDATMP/IDIS,IUNT,IXP,ISW1,TTLE,NAMEI,NPTS,
IBF,IFF,ILF,MM

```

The output of the file LEEDCM.DEF is shown in Fig. 4. The first three lines list all commands that are used in programs LEEDRT,VIDCON, and DATMNP. They are written by the I2, 40A2 format. The two digits at the beginning of each line indicate the maximum number of commands that can be used. Following these numbers are commands represented by two characters. The relative position of these commands is important since

```

35IUPVUIGIIAAGOPCOXTRPSATPVCLDCLHERYFDRSTGPAGOSCDUTAMOCMGFDMXVXDIEDLPMSTE
16EXHECCDSDEEDTRLADILINEADSTODPRNI
25HEATEXPXWTDSTFPAGPSMARSELMLCLSCGOOPCFRSNIINCRGSTMHF
  1  30  6  3  0  2  1
  1  90  1 10  1  0
  0  1 10  0 500 900  1 100
256 256 20 20  0  2  1.0000  1
BEAM 1
256 256 20 20  0  2  1.0000  1
BEAM 2
256 256 20 20  0  2  1.0000  1
BEAM 3
256 256 20 20  0  2  1.0000  1
BEAM 4
256 256 20 20  0  2  1.0000  1
BEAM 5
256 256 20 20  0  2  1.0000  1
BEAM 6
256 256 20 20  0  2  1.0000  1
BEAM 7
256 256 20 20  0  2  1.0000  1
BEAM 8
256 256 20 20  0  2  1.0000  1
BEAM 9
256 256 20 20  0  2  1.0000  1
BEAM 10
256 256 20 20  7
  1  1  1  1  1 750  1  1
  1 250  1 10
  2 5 1 0 1 5 100
LD3:LEEDTM,000 0
LD3:LEEDDT,000 0
4IATPPVDM
4GSPMSBDS
TEST

DATA

```

Figure 4. Output of the file LEEDCM.DEF. This file contains all the required parameters for the LEED program.

the programs read them in accordance with their relative positions. The next three lines are in the 8I5 format. They cover parameters carried by common blocks PARM, VPARAM, BLK1 and HPARAM. Following those lines are 20 lines that contain information for the ten selected windows. Then there are three 8I5 lines and one 6I2, 3I4 line. These four lines correspond to parameters in common blocks PROF, PROFL, MNPLTC and CDATMP. The next two lines with 7A2, I2 format are for storing names of the data files. The first is for the experimental data file and the second is for the file of x-y data (which will be defined in Section IIC). They are both carried by the common block NAMEC. The next two lines store the "GO" commands for LEEDRT and DATMNP. They are both I2, 20A2 formatted. The last two lines both have 130 characters space for storing the experimental title and x-y data file title.

The value of the parameters contained in this parameter file can be changed by calling subroutines DTPRAM and PARMCH through commands CP and PA (cf. Fig. 3).

C. Experimental Data Storage

The experimental data are stored in IHP and DPRAM arrays. The IHP array can hold 1000 integers which is defined as one "data point". The DPRAM array can accept 5 real numbers. The first digit records time (by default) and the rest of the digits can be defined by users. All the information for the LEED spots (y-value) is stored in the IHP array while other information like time or beam energy (x-value) is stored in the DPRAM array. The IHP and DPRAM arrays require a total of 1010

words in memory space. The LEED program opens a record size 512 which equals 1024 words in the memory space and is large enough to store one "data point". By dividing the 3000 blocks (768000 words) reserved by SCTPRO.BIN in VMO with 1024, a total number of 750 data points can be obtained. Note that this maximum number of data points cannot be increased by decreasing the total number of windows or by decreasing the size of the windows. This is because the 1024-word space is opened and used for one "data point" regardless of whether it is completely filled or not. The IHP and DPRAM arrays can be printed out by command DU in the main program. Figure 5 shows an example of such an output. The explanation of the arrangement of these two arrays is listed in Table 1.

10	1	10	14	70	146	242	338	408	482	578	674	744	51	220
220	218	221	217	223	221	218	219	222	221	223	230	232	227	229
232	237	249	255	261	278	309	348	388	399	402	400	406	432	412
356	321	305	276	252	242	244	237	236	232	228	227	225	225	225
221	219	227	222	221	1	2	375	382	71	217	216	216	214	218
216	216	215	220	220	218	221	219	223	221	218	219	222	221	223
230	232	227	229	232	237	249	255	261	278	309	348	388	399	402
400	406	432	412	356	321	305	276	252	242	244	237	236	232	228
227	225	225	225	221	219	227	222	221	218	219	219	219	218	214
216	219	217	218	216	215	1	2	377	382	91	216	213	219	215
212	216	214	214	215	213	216	214	220	213	218	219	218	219	215
220	220	218	218	221	220	217	217	221	223	223	226	225	224	225
235	235	238	239	250	257	270	287	299	333	378	386	418	448	424
404	401	384	330	308	294	266	250	245	237	232	228	222	226	223
220	218	218	217	217	214	213	214	210	212	213	210	213	216	210
208	211	209	211	211	209	210	209	209	211	211	209	1	2	538
134	91	222	225	223	223	226	222	222	224	220	222	228	223	223
228	219	223	223	224	226	224	223	230	224	224	232	231	231	227
234	228	234	235	240	242	236	242	246	259	263	262	266	274	300
317	336	366	388	389	379	369	381	371	347	305	272	266	260	259
254	245	236	234	237	229	224	225	225	221	218	222	221	220	221
216	219	219	218	218	219	220	218	215	216	219	218	216	218	216
216	218	214	1	1	374	381	65	204	205	205	205	205	205	205
206	205	206	205	206	206	207	207	206	206	208	208	207	208	208
209	210	211	212	213	214	216	217	216	216	216	216	214	213	211
210	210	210	210	210	208	208	209	209	208	208	207	208	208	209
208	208	207	209	209	208	207	208	208	208	208	208	208	51	0
176	186	69	208	209	209	209	210	210	210	211	211	212	212	212
213	214	214	215	215	216	218	219	219	220	220	223	224	225	226
228	232	234	238	241	246	252	256	260	262	261	258	252	247	241
238	235	232	230	228	226	225	224	223	222	221	220	220	219	219
219	217	217	217	218	217	216	216	216	216	215	215	55	0	537
132	91	202	202	199	200	199	203	201	200	203	200	203	201	200
203	203	203	200	201	199	205	204	203	203	202	207	203	206	204
204	206	207	204	209	207	206	212	214	209	212	223	228	232	232
237	240	236	237	237	234	227	224	223	217	209	213	211	213	211
207	208	215	213	210	206	211	212	209	207	208	209	209	209	210
209	212	208	208	210	213	211	208	211	210	212	213	209	210	210
213	214	210	1	2	175	180	91	206	204	205	203	205	208	207
205	210	204	208	205	205	202	201	205	207	203	206	207	204	207
203	208	205	207	207	211	207	208	209	211	216	214	209	215	220
219	220	222	232	238	236	251	253	245	246	243	239	232	229	224
222	217	220	219	213	214	211	210	210	206	208	210	210	207	209
206	209	209	211	207	209	214	208	210	209	210	212	206	207	208
206	206	209	209	211	215	210	212	211	1	1	176	185	65	216
217	217	216	217	217	217	217	216	216	216	217	217	218	217	216
216	217	217	217	216	216	217	217	217	217	217	217	217	217	216
216	217	218	217	217	217	217	217	217	217	217	217	217	217	217
217	216	216	217	216	217	216	217	217	218	218	218	218	218	218
218	218	218	218	51	0	291	266	91	213	214	210	212	206	209
214	210	210	209	209	210	213	208	209	210	210	211	210	211	212
213	210	211	208	210	211	212	208	215	211	210	212	210	215	212
213	211	211	214	213	212	210	214	208	213	212	213	216	213	211
213	216	211	213	208	211	215	213	212	215	217	218	212	215	215
218	215	218	217	218	213	215	219	217	214	215	219	218	219	219
216	218	219	217	220	218	216	218	219	219	1	1	366	184	
0.434		0.000		0.000		0.000		0.000		0.000				

Figure 5. An example of output of the IHP(1000) array and the DPRAM (5) array for a single "data point".

Table 1. Explanations of the IHP(1000) and DPRAM(5) arrays.

Element location in the IHP array	Explanations
1	Total number of selected windows
2	Data point
3	Number of frames used to sum the video signal in the experiment
4 to 13	Starting location of each window in this array
14	The number (IL) indicates the length of the first window
15 to 15+IL-1	Intensities of each pixel in the first window, can be either cut profile of integrated profile.
15+IL	Width of the first window
15+IL+1	Type of the first window
15+IL+2	x-coordinate of the center of the first window
15+IL+3	y-coordinate of the center of the first window
15+IL+4	The number (IL) indicates the length of the second window
...	(The rest of the data represent pattern common to all the other windows)
	The last line is the DPRAM array

Note that such an output has only one data point which covers the information of ten windows. In the example shown by Fig. 5, there are 10 windows selected. This output is the first data point. It represents a summation of 10 frames. The first window starts at the 14th location; the second window starts at the 70th location, the third window starts at the 146th location; etc. The number at the 14th location is 51 (IL) which indicates the first window has 51 pixels. From the 15th location to the 65th location ($15+51-1=65$) are the intensity numbers for these 51 pixels. Following these numbers is the character 1 which represents the width of the first window. The number 2 that follows indicates that this window is defined as a horizontal profile. The following two numbers are the x and y coordinates of the center of the first window. In this case, they are 375 and 382. The next number is 71. It is located at the 70th position. This number represents the length of the second window. The other numbers after it repeat the pattern seen in window 1. Note that this file takes only 839 locations in the IHP array.

The last line lists the number 0.434. It is saying that this data point is acquired in 0.434 seconds.

If there are 50 "data points" in one experiment then there will be 50 IHP and 50 DPRAM arrays. Each IHP array represents a different data point. The program DATMNP allows one to plot out these data points in terms of spot intensities vs. time or beam energy or FWHM vs. time or beam energy. These kinds of plots are defined as x-y data point plots.

III. HOW TO EDIT THE LEED PROGRAM

The procedures and commands used to edit the LEED program are listed below:

1. Type: ASSIGN LDO: DK: (Enter directory LDO)
2. Type: KED XXXX.FOR (XXXX.FOR represents a program written in FORTRAN code)
3. Upon finishing the editing procedure, use "PF1" key followed by "COMMAND" key and then type: EXIT
4. Type: FORT XXXX (This command generates a XXX.OBJ file)
5. Type: @ LEEDLK (This command generates a LEED.SAV file)
6. Copy this LEED.SAV to LD1:
7. Enter LD1 by typing: ASSIGN LD1: DK:
8. Execute the LEED program by typing: @RLEED.

CONCLUSIONS

In this thesis, we have investigated the interactions between oxygen and the Pd(100) surface. The main conclusions which have been drawn can be summarized as follows:

(a) A metastable $c(2 \times 2)$ structure can be formed when adsorption is carried out at low temperature and high pressure. Possible models to explain this result are discussed, including a model in which an ensemble of eight empty sites is probably required for oxygen molecules to adsorb dissociatively. The energy barrier for oxygen to diffuse on this surface is estimated to be 12 ± 1 kcal/mol.

(b) Adsorption of atomic oxygen proceeds via a temperature dependent molecular precursor state. The sticking probability is 1.0 at 180 K and 0.60 at 300 K.

(c) The metastable $c(2 \times 2)$ structure can always be trapped when adsorption temperatures are below 300 K. There are two steps involved in transforming the metastable $c(2 \times 2)$ to a $p(2 \times 2)$ structure when the sample is annealed. First, the metastable $c(2 \times 2)$ is destroyed. Second, the $p(2 \times 2)$ domains grow.

(d) Three distinct desorption states, α , β , and γ are observed in TDS spectra and are characterized. The α state shows the traits of second-order kinetics and is due to desorption of oxygen from a disordered layer. The β state appears at higher-coverages and is due to desorption of oxygen from the $c(2 \times 2)$ ordering. The energy difference barrier between the α and the β states is about 5 kcal/mol and is due to

the repulsive interactions of oxygen in the $c(2 \times 2)$. The γ state shows quasi-zero-order desorption kinetics with a desorption energy which equals 49.5 ± 3.8 kcal/mol.

(e) The $p(5 \times 5)$ reconstruction is induced by oxygen in an activated process. This occurs above 400 K with an activation energy of 44 ± 4 kcal/mole. The $p(5 \times 5)$ reconstruction forms from the $c(2 \times 2)$ regions and follows a nucleation and growth mechanism.

(f) The coexistence of two phases, one reconstructed and one unreconstructed, and the equilibrium of adsorbates between them are probably responsible for the quasi-zero-order γ state desorption.

(g) The $\sqrt{5} \times \sqrt{5}R27^\circ$ can be observed at temperature between 570 K and 600 K. There is no activation barrier between the $p(5 \times 5)$ and the $(\sqrt{5} \times \sqrt{5})R27^\circ$ reconstructions.

(h) Adsorption of oxygen at 600 K causes a ring-like LEED pattern to appear which is probably due to the oxidation of the surface.

(i) A complete probably phase diagram for this system is presented. This phase diagram is very complex because the presence of two reconstructions induced by oxygen.

REFERENCES

1. H. Conrad, G. Ertl and J. Küppers, Surf. Sci. 76 (1978) 323.
2. E. M. Stuve, R. J. Madix and C. R. Brundle, Surf. Sci., 146 (1984) 155.
3. S. Ladas, H. Poppa and M. Boudard, Surf. Sci. 102 (1981) 151.
4. C. Nyberg and C. G. Tengstäl, J. Chem. Phys. 80 (1984) 3463.
5. L.-G. Petersson, H. M. Danneberg and I. Lundström, Surf. Sci. 161 (1985) 77.
6. G. Ertl and J. Koch, Z. Phys. Chem. 69 (1970) 323.
7. C. Nyberg and C. G. Tengstäl, Surf. Sci. 126 (1983) 163.
8. K. H. Rieder and W. Stocker, Surf. Sci. Lett. 150 (1985) L66.
9. T. W. Orent and S. D. Bader, Surf. Sci. 115 (1982) 323.
10. J. E. Turner, B. C. Sales and M. B. Maple, Surf. Sci. 103 (1981) 54.
11. G. Ertl, P. R. Norton and J. Rüstig, Phys. Rev. Lett. 49 (1982) 177.
12. J. W. Anderegge and P. A. Thiel, J. Vac. Sci. Technol. A4 (1986) 1367.
13. P. Heilmann, E. Lang, K. Heinz, and K. Müller, Appl. Phys. 9 (1976) 247.
14. E. Lang, P. Heilmann, G. Hanke, K. Heinz and K. Müller, Appl. Phys. 19 (1979) 287.

ACKNOWLEDGEMENTS

I would like to express my sincere appreciation to my advisor, professor P. A. Thiel for her support and guidance throughout my graduate career. It would not have been possible for me to accomplish this project without her very fruitful advice and enormous patience. Most importantly, her inexhaustible enthusiasm for pursuing the scientific truth has always been an inspiration to me, especially when experimental results turned out unexpectedly.

I also want to thank all the people in the group who have provided the warmest friendship to me and my family during my stay at ISU and made this period the most memorable one in my life. My special thanks go to Mike Columbia who taught me very practical English vocabulary every day, and Pam Leavitt who gave me the Velcro to use in the ACS presentation.

I am also greatly indebted to Dr. James W. Evans who taught me how to use the kinematic theory to calculate the LEED spot intensity without worrying about the pressure in the UHV chamber, and Mr. James Anderegg who wrote the LEED program which makes the data acquisition possible.

I also enjoyed very much the friendship with the people from Ames Chinese Christian Fellowship: Dr. T.-C. Chang, Dr. W.-B. Tzeng, Dr. M.-S. Yeh and Dr. Peter Chen to name a few.

Finally, I want to dedicate all my accomplishments to my parents who supported me financially, encouraged me spiritually and provided help whenever I needed.

This work was performed at Ames Laboratory under contract No. 7405-eng-82 with the U.S. Department of Energy. The United States government has assigned the DOE Report number IS-T 1364 to this thesis.